

THESIS FOR THE DEGREE OF LICENTIATE OF ENGINEERING

Developing Computational Methods for Detailed Assessment of Cavitation on Marine Propellers

ABOLFAZL ASNAGHI



Department of Shipping and Marine Technology
CHALMERS UNIVERSITY OF TECHNOLOGY
Göteborg, Sweden 2015

Developing Computational Methods for Detailed Assessment of Cavitation on
Marine Propellers

ABOLFAZL ASNAGHI

© ABOLFAZL ASNAGHI, 2015

Report no 15:156
ISSN 1652-9189

Department of Shipping and Marine Technology
Chalmers University of Technology
SE-412 96 Göteborg
Sweden
Telephone + 46 (0)31-772 1000

Printed by Chalmers Reproservice
Göteborg, Sweden 2015

Developing Computational Methods for Detailed Assessment of Cavitation on Marine Propellers

ABOLFAZL ASNAGHI

Department of Shipping and Marine Technology
Chalmers University of Technology

Abstract

Cavitation often brings negative effects, such as performance degradation, noise, vibration, and material damage, to a marine propulsion systems, but for optimum performance, cavitation is almost inevitable. Therefore, it is necessary to improve the understanding of cavitation in order to maximize the performance without encountering severe problems. Experimental tests can only provide limited information about this complex phenomenon. This thesis deals with improving numerical simulations methodologies that can offer a more complete picture of the cavitation process, making it possible to investigate the flow in more detail with some confidence, thus enabling an improved design.

Numerical simulations of non-cavitating and cavitating flows are conducted using OpenFOAM. The flow is modelled using Implicit Large Eddy Simulation and considering the two phases, i.e. vapour and liquid, as a homogeneous mixture through a volume fraction transport equation method along with the Schnerr-Sauer mass transfer model.

To avoid manual calibration of the mass transfer model coefficients, which may significantly affect both the accuracy and stability of the numerical predictions, an approach is suggested and tested to compute the mass transfer rate based on the flow local time scale during the solution procedure. Moreover, the saturation pressure is modified in order to take into account the shear stress effects on the liquid rupturing.

To test the proposed modifications, several test cases consisting of 2D and 3D hydrofoils and model scale propellers are simulated and the results are compared with experimental data. Integral quantities, local pressure data, and cavitation extent are studied for both the non-cavitating and the cavitating flows. Furthermore, the computational set-up is tested by varying domain size, mesh type and resolution, numerical schemes, and mass transfer model coefficients.

The overall results compare well with the available experimental data, provided the mesh resolution is sufficient. The proposed mass transfer model modifications give a considerably improved prediction of pressure distribution and cavity extent. Some results yield overpredicted cavitation, indicating discrepancies between the modelling approach and model scale experimental techniques.

Keywords: Cavitation, Hydrodynamics, Numerical simulation, LES, OpenFOAM

Acknowledgement

This work would have not been possible without the help, support and encouragement of many people along the last few years. First and foremost I would like to thank my supervisors Professor Rickard E. Bensow and Dr. Andreas Feymark for all the valuable discussions, enthusiasm and support.

I also would like to thank Professor Göran Bark and Dr. Urban Svennberg for all of the interesting discussions that we had about the physics of cavitation.

Thanks towards all of my colleagues in the Department of Shipping and Marine Technology for providing a wonderful atmosphere, especially to Dr. Arash Eslamdoost who was a perfect colleague and friend. I also would like to thank Johannes Palm for all of the interesting fruitful discussions that we had about OpenFOAM.

Rolls-Royce Marine is acknowledged for funding the project through the Rolls-Royce Technology Centre at Chalmers. The Chalmers Centre for Computational Science and Engineering (C3SE) is also acknowledged for providing computational resources through the project.

All my gratitude to my parents, all of my achievements and success is only due to their way of bringing me up.

CONTENTS

1	Introduction	1
1.1	Cavitation	1
1.1.1	Definition	1
1.1.2	Cavitation number	1
1.1.3	Different types of cavitation	2
1.1.4	Cavitation effects	4
1.2	Effective parameters	6
1.2.1	Nuclei content	6
1.2.2	Roughness	6
1.2.3	Leading edge region	7
1.2.4	Viscous effects	7
1.3	Propeller terminology	8
1.4	CFD Methods	9
1.4.1	Eulerian vs. Lagrangian methods	9
1.4.2	Interface tracking vs. interface capturing methods	10
1.5	Objectives and studies of the present research	11
1.6	Thesis outline	14
2	Governing equations	17
2.1	Mass and momentum continuity equations	17
2.2	Mass transfer modelling	18
2.3	Turbulence modelling	18
3	Numerical Methods	19
3.1	OpenFOAM Package	19
3.2	Modified interPhaseChangeFoam solver	19
3.2.1	Schnerr and Sauer cavitation model	20
3.2.2	Pressure correction equation	21

3.2.3	Solution Strategy	23
4	Sheet Cavity Inception Modelling	25
4.1	Phase change time scale	25
4.2	Viscous shear stress effects	27
5	Numerical Results - 2D and 3D hydrofoils	29
5.1	NACA0009	29
5.1.1	Experimental setup	30
5.1.2	Numerical setup	30
5.1.3	Schnerr-Sauer model parameters tuning	31
5.2	NACA66MOD	34
5.2.1	Experimental setup	34
5.2.2	Numerical setup	35
5.2.3	Cavitation simulation	36
5.3	Twisted Delft hydrofoil	39
5.3.1	Experimental setup	40
5.3.2	Geometry and mesh structure	40
5.3.3	Flow conditions	41
5.3.4	Computational mesh description	42
5.3.5	Wetted flow simulation	43
5.3.6	Evaluation of mass transfer modelling modifications	44
5.3.7	Effects of the outlet boundary distance	49
5.3.8	Spatial mesh resolution effects on cavitation simulation	51
6	Numerical Results - Cavitating propellers	61
6.1	E779A	63
6.1.1	Computational domain, grids and simulation conditions	63
6.1.2	Noncavitating flow conditions	64
6.1.3	Cavitating flow conditions	65
6.2	PPTC propeller, SMP 2015	67
6.2.1	Introduction	67
6.2.2	Computational domain and mesh specifications	69
6.2.3	Wetted flow numerical results	70
6.2.4	Cavitating flow numerical results	71
6.2.5	Case2.1	71
6.2.6	Case2.2	77
6.2.7	Case2.3	80
6.3	Rolls-Royce high skew propellers	81
6.3.1	Experimental setup	81
6.3.2	Computational domain and mesh specifications	83
6.3.3	Wetted flow numerical results	85
6.3.4	Cavitation prediction of the RR-A propeller	86
6.3.5	Cavitation prediction of the RR-B propeller	87

7 Summary and suggestions for future work	91
REFERENCES	95

LIST OF FIGURES

1.1	Water phase diagram	2
1.2	Different types of cavitation	3
1.3	Erosion caused by cavitation on an arbitrary propeller	5
1.4	Erosive mechanisms formed during bubble collapse	5
1.5	Schematic effects of nuclei content on propeller cavitation	6
1.6	Schematic effects of roughness at the propeller leading edge	7
1.7	Cavitation detachment and laminar boundary layer separation points	7
1.8	Different types of propeller cavitation	9
3.1	Cavitation Solver Algorithm	24
5.1	EPFL high speed cavitation tunnel	30
5.2	Cavitation simulation settings, NACA0009	31
5.3	Pressure distribution of NACA0009 for different number of nuclei	33
5.4	Pressure distribution of NACA0009 for different nuclei diameters	33
5.5	Pressure comparison between modified and original coefficients	34
5.6	cavitation simulation setting of NACA66MOD	35
5.7	Pressure coefficient of NACA66MOD	36
5.8	Averaged cavity distribution around NACA66MOD	37
5.9	Local mesh refinement at the cavity closure region, NACA66MOD	38
5.10	Effects of the mesh resolution at the closure region, NACA66MOD	39
5.11	Pressure probes locations and numbers on the Twist11 foil	40
5.12	Computational domain of Twist11 simulation	41
5.13	Averaged vapour iso-surfaces and pressure distribution around Twist11 with $y^+ = 1$	46
5.14	Added Pressure to the threshold pressure due to the viscous effects for cavitation around Twist11	46
5.15	Comparison between numerical and experimental data for pres- sure variations at different sections of the Twist11 foil	48

5.16	Variation of lift coefficients for model B and model C versus time	50
5.17	Cavity and pressure distribution during negative lift force	50
5.18	Pressure variations calculated at different probes location	51
5.19	Pressure distributions for different outlet boundary distances	52
5.20	Pressure coefficient distributions at the section of $y/S = 0.5$	52
5.21	Pressure coefficient over Twist11 for different mesh resolutions, wetted flow	54
5.22	Pressure coefficient over Twist11 for different mesh resolutions, cavitating flow	55
5.23	Variation of lift coefficient for various mesh resolutions, cavitating flow	56
5.24	Integrated vapour volume fraction for different mesh resolutions in one typical shedding cycle	57
5.25	Averaged vapour iso-surfaces 10% around Twist11 with $y^+ = 1$ for four different mesh resolutions.	58
5.26	Part one - Comparison between numerical results and experimental snapshots for cavitation shedding	59
5.26	Part two - Comparison between numerical results and experimental snapshots for cavitation shedding	60
6.1	E779A propeller	63
6.2	Boundaries setting for E779A propeller simulation	64
6.3	Mesh specification of E779A propeller	64
6.4	Numerical results comparison with experiment, E779A propeller	66
6.5	Comparison of different calibrated cavitation mass transfer models	67
6.6	SMP'15 propeller geometry	68
6.7	SMP'15 propeller and experimental tunnel sketch	68
6.8	The computational domain of SMP-Mesh-I and SMP-Mesh-I	70
6.9	The blade surface mesh for SMP-Mesh-III	70
6.10	Description of radius ratio over the blade surface	72
6.11	Vapor iso-surfaces for Case2.1, SMP-Mesh-I, view along x-axis	73
6.12	Comparison between numerical results and experimental sketches for cavitation in Case2.1, suction side	75
6.13	Comparison between numerical results and experimental sketches for cavitation in Case2.1, pressure side	76
6.14	Case2.1, view along x-axis, suction side, SMP-Mesh-I	77
6.15	Case2.1, view along x-axis, Suction side, vapour iso-surface 0.6	78
6.16	Vapor Iso-surfaces for Case2.2, SMP-Mesh-I, view along x-axis	79
6.17	Vapor Iso-surfaces for Case2.3, SMP-Mesh-I, view along x-axis	80
6.18	The general sketch of the RR propellers geometries	82
6.19	Experimental setting of the propeller cavitation tests	83
6.20	Inclined propeller towards the incoming flow in experiment setup	83
6.21	Isometric view of the computational domain, RR propellers	84
6.22	Surface mesh of the propeller RR-A	85

6.23	Triangular surface mesh of the propeller RR-B, Mesh-RR-B-2 . . .	85
6.24	Side view of numerical predictions vapour Iso-surfaces (50 %) and experimental snapshot, RR-A propeller	87
6.25	Front view of numerical predictions vapour Iso-surfaces (50 %) and pressure coefficients of RR-A propeller	87
6.26	Pressure coefficient distribution and vapour iso-surfaces (50 %) of cavitating flow simulations for RR-B propeller	89
6.27	Zoomed in view of vapour iso-surfaces (50 %) and pressure coefficient distribution of numerical results for RR-B propeller	89
6.28	Comparison between vapour iso-surfaces (50 %) of numerical results and experimental observations for RR-B propeller	90
6.29	Vapor iso-surfaces (10 %) of numerical results for RR-B propeller	90

LIST OF TABLES

5.1	Boundary conditions for cavitation simulation around NACA0009	31
5.2	Investigated parameters for cavitation simulation around NACA0009	31
5.3	Boundary conditions for cavitation simulation of NACA66MOD	35
5.4	Surface mesh specification for mesh independency study, $y^+ = 50$	42
5.5	Mesh specification for mesh independency study with different y^+	42
5.6	Mesh specification for cavitation simulation, $y^+ = 1$	43
5.7	Lift coefficients for various mesh resolutions, wetted flow Twist11	43
5.8	Lift Coefficient for different y^+ , wetted flow Twist11	44
5.9	Coefficients of the three different models investigated	45
5.10	Lift coefficients results of different cavitation models	49
5.11	Lift and drag coefficients for various mesh resolutions	53
5.12	Lift coefficient for various mesh resolutions in cavitating flow simulation	55
5.13	Comparison of the shedding frequency of the cavitating flows	57
6.1	Simulation conditions of E779A propeller	65
6.2	Wetted flow open water performance of E779A propeller	65
6.3	Cavitating flow open water performance of E779A propeller	66
6.4	Case2 of SMP 2015 operating conditions	69
6.5	Case2 of SMP 2015 numerical boundary conditions	69
6.6	Wetted flow open water coefficients of PPTC propeller	71
6.7	Cavitating open water coefficients of PPTC propeller	72
6.8	Boundary conditions for cavitation simulation, RR propellers	84
6.9	Wetted flow open water performance of the RR propellers	86
6.10	Cavitating open water performance of the propeller RR-A	86
6.11	Cavitating open water performance of the propeller RR-B	88

1

Introduction

1.1 Cavitation

1.1.1 Definition

Cavitation is the formation of vapour in a liquid when local static pressure of liquid falls below a critical pressure threshold. As pressure of a larger region gets below the threshold pressure, more liquid will change phase into vapour. Without considering the effects of shear forces in flowing fluids, the pressure threshold is equal to the saturation pressure. The difference between cavitation and boiling is that cavitation occurs due to pressure drop while boiling is caused by an increase in temperature, Figure 1.1.

The region or pocket of the generated vapour in the cavitating flows is called cavity. The cavity can be either steady and attached to the surface or it can be separated from the surface and transported downstream. The size of the cavity might vary from aggregation of a few bubbles to a size that covers the whole geometry (super cavity).

In order to maintain the thermodynamic balance at the interface of the two phases during cavitation formation, the liquid will experience evaporation cooling which causes the temperature to slightly drop around the liquid-vapour interface. For fluids like water where the density ratio between liquid and vapour is very high (e.g. 1000 to 0.025 kg/m^3 for water), these thermal effects are not significant and cavitation formation reasonably can be considered isothermal [1, 2].

1.1.2 Cavitation number

The cavitation number, σ , is presented in Equation 1.1 where in this equation U_∞ and p_∞ are respectively the reference velocity and pressure, ρ_l is the density of

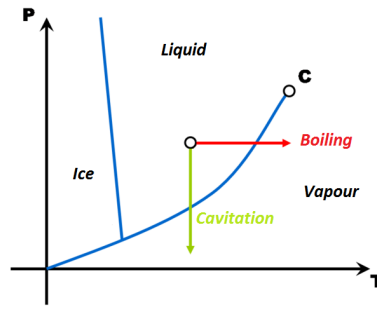


Figure 1.1: Water phase diagram

liquid, and p_{sat} is the saturation pressure.

$$\sigma = \frac{p_{\infty} - p_{\text{sat}}}{\frac{1}{2}\rho_l U_{\infty}^2} \quad (1.1)$$

It is conventional to categorize the cavitating flows based on the cavitation number. The cavitation number represents the same ratio as the Euler number where in both numbers the ratio of the free stream pressure head to the inertial forces are computed. However, in the cavitation number the pressure head is the difference between the reference pressure and the saturation pressure. Therefore, the cavitation number reflects how close the liquid pressure is to the saturation pressure. It should be noted that cavitating flows are affected by the boundary layer (e.g laminar flow or transient flow), thus the Reynolds number also becomes important,

$$Re = \frac{\rho U D}{\mu}. \quad (1.2)$$

1.1.3 Different types of cavitation

There are five main cavitation patterns observable in cavitating flows depending on the operating conditions and fluid properties. These five flow patterns are briefly discussed in the following, see also Figure 1.2.

Bubble cavitation

The main feature of this type of cavitation is the formation of separated bubbles, their transportation to the downstream, and their collapse at the higher pressure region of the downstream of the flow.

Sheet cavitation

In this type of cavitation, the cavity stays attached to the surface. The interface between liquid and vapour at this condition is sharp and easily distinguishable.

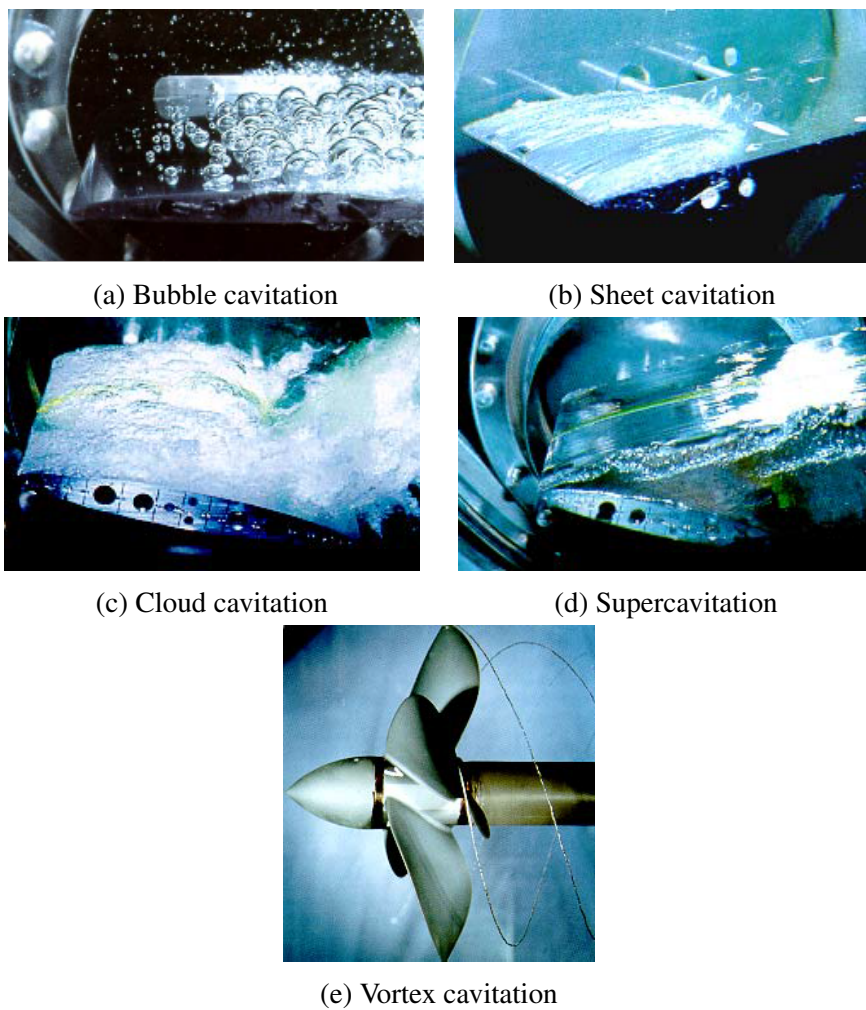


Figure 1.2: Different types of cavitation [1]

Cloud cavitation

Here, the cavitating flow consists of a large collection of small bubbles separated from the initial sheet cavity. If there is a re-entrant flow at the end of the cavity that is strong enough to separate the cavity from the surface, two phase vortex shedding occurs. This phenomenon is characterized by strong vibration, and noise. In the case that the transported cavity collapses near the surface, the risk of erosion is also considerable.

Supercavitation

This indicates as a type of cavitation where the cavity is large enough to cover either the whole object or most of it. The main application of supercavitation is to decrease the drag force. In super cavitation conditions, since most of the surfaces are covered by vapour and considering that the viscosity of vapour is much lower than the liquid, the skin friction will be smaller than the corresponding wet flow conditions.

Vortex cavitation

This type of cavitation can be defined as the formation of cavitation in the core of vortices. Due to the high velocity gradients and the flow feature of vortices, the pressure at a vortex core is lower than the surroundings. If the pressure of the core falls below the saturation pressure, cavitation will start at the core, and can travel to the downstream of the flow with the vortex. This type of the cavitation mainly occurs on the tips of rotating blades and in the separation zone of bluff bodies.

1.1.4 Cavitation effects

1.1.4.1 Erosion, noise and vibration

Cavitation can occur in a machine for several reasons [1, 3, 4]:

1. Change of streamlines curvatures (e.g. blades tip, and restricted section passage like nozzles) leads to local increase of flow velocity and reduction of pressure which in some circumstances can cause cavitation;
2. Flow instabilities can cause pressure fluctuations (e.g. in diesel injectors);
3. Solid surface imperfections (e.g. in hydraulic constructions);
4. High shear and high vortex flows (e.g. in cavitating jet, and turbine vortex rope).

For a system or machine designed to operate in liquid phase (or very limited amount of cavitation), presence of cavitation is unfavourable and may cause several negative consequences mainly on the performance and life time of the machine. For propellers, cavitation can increase the losses, and therefore decrease the efficiency or limit the blades' thrust. Another negative aspect of the cavitation is related to the collapse of the cavity.

The collapse can cause severe pressure pulses. In the case that these collapses occur near a surface, they can cause damage by removing material from the surface which is called erosion, Figure 1.3. This process is noisy, and also due to posing high pressure pulses at different time occasions to the solid surface, can lead to significant vibration on the body. This phenomenon is complex since it involves both the flow characteristics and surface material properties. Therefore, in order to control it one has to investigate hydrodynamics behaviours of the flow and also the structural responses of the solid body to these hydrodynamics behaviours at the same time.

The main reason for erosive behaviour of cavity collapse can be explained by considering the energy balance. When the cavity is formed, the energy of phase change is restored in the cavity. During the shrinkage of the cavity, the concentration of the energy will increase. When the cavity (e.g. a bubble) collapses, the

restored energy will be released. This energy concentration can result in very high stress levels which can exceed the material resistance such as yield strength or fatigue limit. Mainly the level of released energy, occasion of its occurrence, and the response of the surface material will determine the erosion level. The schematic emitted pressure wave during a bubble collapse is depicted in Figure 1.4.

Two main parameters responsible for erosive collapse are the emission of the shock waves during the collapse of the bubble which causes very high amplitude pressure pulse in very short time span, and the generation of a high-speed liquid jet directed towards the solid boundary [5].

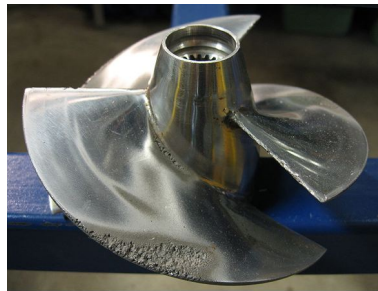


Figure 1.3: Erosion caused by cavitation on an arbitrary propeller [6]

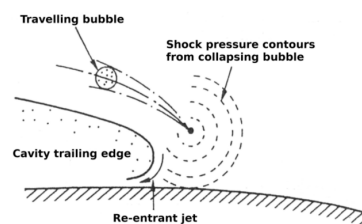


Figure 1.4: Erosive mechanisms formed during bubble collapse and pressure waves from bubble collapse, [3]

1.1.4.2 Drag reduction

Cavitation can have positive effects such as reduction of the drag force. When a body moves in water with high speed, formation of cavitation is almost inevitable. Depending on the geometry of the body (basically the head shape) and flow conditions, the cavity can cover some parts or all of the body. This type of cavitation as it is discussed previously is called supercavitation. Since the viscosity of vapour is much lower than the viscosity of liquid, the skin friction exerted on the body will be lower than the similar wet flow condition (single liquid phase condition). It is also possible to inject air inside the cavity in order to expedite or expand the cavitation formation and stabilize the cavity, known as ventilated cavity.

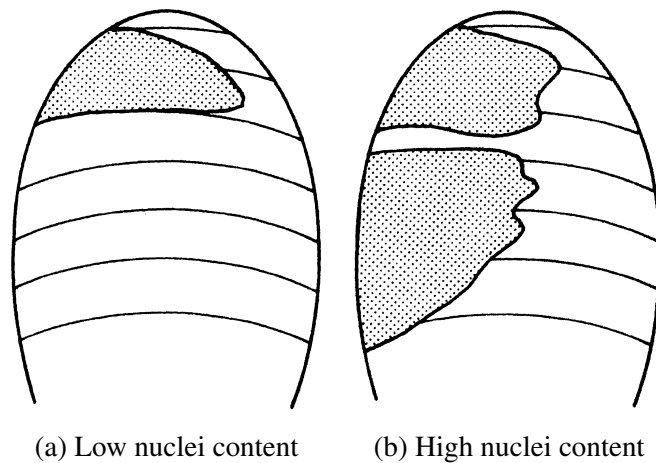


Figure 1.5: Schematic effects of nuclei content on propeller cavitation, [3]

1.2 Effective parameters

1.2.1 Nuclei content

Experimental tests have revealed that when the amount of dissolved gas bubbles inside the liquid is very low, the cohesion force between liquid molecules becomes very strong. At this condition, the liquid can withstand tension (i.e. negative pressure) without undergoing any phase change. The dissolved or non-condensable gas bubbles act as weakness points inside the liquid where the cohesion force is weaker than other parts of the liquid and therefore the liquid breaking down starts from these points. These dissolved gas bubbles are known as nuclei [1, 3].

The amount of nuclei is important because it can influence not only the extent of the cavitation but also its structure and periodic behaviour. In Figure 1.5, the effects of the nuclei content on the propeller cavitation pattern is depicted schematically.

1.2.2 Roughness

The laminar boundary layer can suppress the cavitation inception, and affects its pattern due to the change in the location of cavitation inception. While the boundary layer of full scale propellers are considered to be fully turbulent, except for a small region close to the propeller leading edge, the boundary layer on a model scale propeller can be laminar in considerable part of the blade area. Therefore, it is possible that due to the different boundary layers between model and full scales, different cavitation patterns are observed, Figure 1.6. One solution to this discrepancy is to deliberately trip the boundary layer of model scale into turbulence at the leading edge by applying roughness. In this condition, the model scale boundary layer transition will occur close to the leading edge representing the full scale flow pattern much better [1, 3].

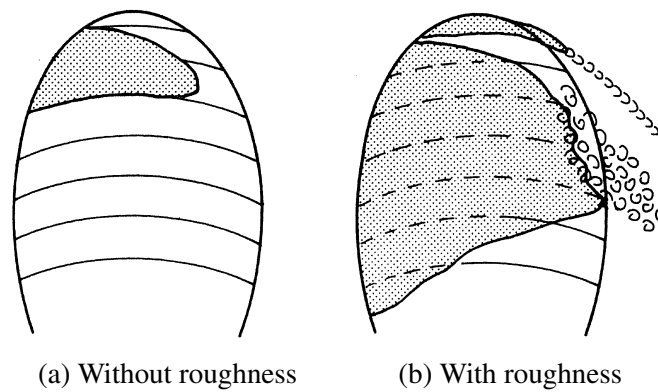


Figure 1.6: Schematic effects of roughness at the propeller leading edge on the cavitation pattern, [3]

1.2.3 Leading edge region

Studies show when there is laminar boundary layer separation on the leading edge of a hydrofoil, cavitation starts after the separation point. Inception of cavitation after the separation point which has the lowest pressure value poses a paradox known as the cavity detachment paradox. In this condition, since the pressure gradient after separation is reverse, the location of cavitation inception has higher pressure than the separation point, Figure 1.7. Therefore, the paradox suggests that liquid is in tension upstream the cavity detachment. It was shown on a polished hydrofoil that the boundary layer separation offers a shelter protecting the vapour cavity from being swept off by the incoming flow [7, 8].

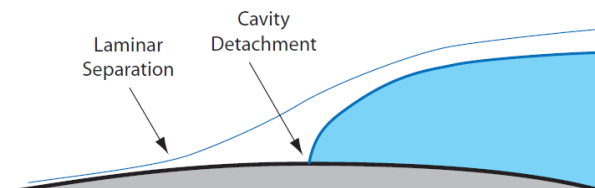


Figure 1.7: Cavitation detachment and laminar boundary layer separation points on a typical cavitating hydrofoil

1.2.4 Viscous effects

It has been observed that the viscous effects (or more accurately the laminar boundary layer effects) are predominant in the detachment region of cavitating flow near the leading edge [7, 9, 10]. It is shown that a well-developed cavity always detaches downstream of laminar separation of the boundary layer. Attached cavitating flow can form in a turbulent boundary layer. The natural transition

to turbulence on full scale ship propellers occurs near the leading edge resulting in attached leading-edge cavitation. On smooth hydrofoils, the natural transition to turbulence will occur at different locations on the hydrofoil. One approach to resemble the flow on ship propellers in the experiments of model scale cases is applying roughness at the leading edge to trip the boundary layer into transition. Thus, the leading edge roughness effectively eliminates the laminar flow and causes the cavitation inception to occur at the leading edge. As a consequence the point with minimum surface pressure and the point of cavity detachment are approximately at the same location [11]. However, for the cases that the laminar boundary layer covers some portions of the blade or hydrofoil, the cavitation behaviour will be affected and accurate modelling of the laminar to turbulent transition has direct effects on the accuracy of cavitating flow prediction. Another aspect of the viscosity is the damping of large gradients and the loss of mechanical energy during the growth and collapse process [11, 12]. The flow shear stress is also dependent on the fluid viscosity.

1.3 Propeller terminology

The hydrodynamic performance of a propeller is defined by using non-dimensional thrust and torque coefficients and also the advance ratio, Equations 1.3, 1.4, and 1.5. Respectively in these equations, D is the propeller diameter, n is the rotational speed of the propeller in rev/sec, ρ is the fluid density, T is the propeller thrust force, Q is the propeller shaft torque, and V_A is mean inflow velocity towards the propeller plane.

$$K_T = \frac{T}{\rho n^2 D^4} \quad (1.3)$$

$$K_Q = \frac{Q}{\rho n^2 D^5} \quad (1.4)$$

$$J = \frac{V_A}{nD} \quad (1.5)$$

The open water efficiency of a propeller is defined by,

$$\eta_o = \frac{TV_A}{2\pi nQ} = \frac{JK_T}{2\pi K_Q}. \quad (1.6)$$

In a real application, the ship hull will affect the flow field creating a complicated wake flow field upstream of the propeller. This complicated flow can drastically influence the propeller performance. Depending on the complexity of the flow field, and propeller characteristics, a propeller may experience different types of cavitation, Figure 1.8.

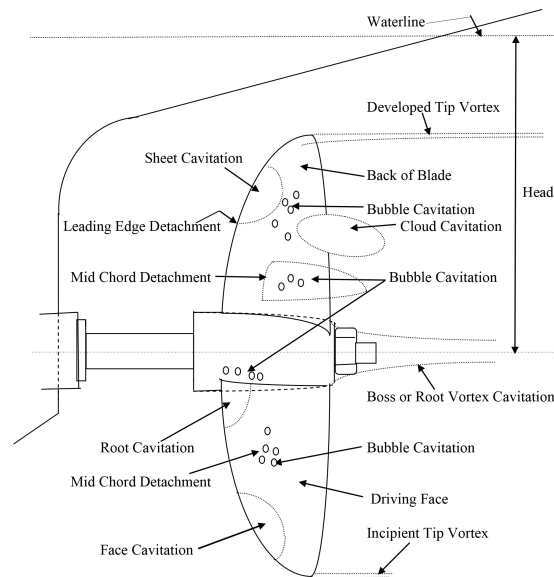


Figure 1.8: Different types of propeller cavitation, [13]

1.4 CFD Methods

In this section, different CFD methods for simulation of cavitating flows are presented and briefly discussed.

1.4.1 Eulerian vs. Lagrangian methods

In the Eulerian description of a field, the field (e.g. velocity, pressure, density, etc.) is represented as a function of position x and time t while Lagrangian specification of the field is a way of looking at fluid motion where the observer follows an individual fluid parcel as it moves through space and time. Considering two phase flow, different specifications can be used which are briefly described below [14, 15].

1. Euler-Euler approach: In this approach, the liquid and vapour phases are both described as interpenetrating fluids. For each phase, a set of mass and momentum equations is solved and coupled with other phases properties (e.g. through void fraction transport equation) to close the governing equations.
2. Euler-Lagrange approach: If there is a continuous phase and a dilute/disperse phase where the dispersed phase occupies a low volume fraction, then the fluid phase is treated as a continuum while the dispersed phase is considered as particles modelled individually. In that case, the mass and momentum equations are solved for the continuous phase while the dispersed phase

is solved by Lagrangian Particle Tracking method. It tracks the particles or bubbles through the calculated flow field. The dispersed phase exchanges momentum, mass and energy with the fluid phase. The trajectory of the particles are calculated individually at specified intervals during the fluid phase calculations [14].

1.4.2 Interface tracking vs. interface capturing methods

Based on the modelling of liquid-vapour interface and in Euler-Euler methodology, the modelling can be categorized further down in two groups, interface tracking methods and interface capturing methods [16, 17].

In the interface tracking approach the physical properties of the liquid phase are only solved. In this approach the interface between vapour and liquid is considered as a boundary condition for the liquid governing equations where the pressure at the interface (i.e. the vapour region) is considered constant and equal to the saturation pressure. The idea is to decompose the domain into two regions and then tracing or deforming the interface in an iterative way until convergence [18]. The interface can be either traced by the marker particles that define its location or by deforming the computational grid. This approach provides a sharp clear interface between phases.

The interface capturing methods, also called the continuum modelling, treat the flow as a mixture of vapour and liquid where the mixture density values varies continuously between liquid and vapour densities values. Therefore, there is no need to track the interface as it would be a part of the results when the governing equations of the mixture are solved.

1.4.2.1 Inhomogeneous vs. Homogeneous

Depending on how the interactions between phases are modelled, the cavitation interface capturing methods can be classified in two groups, the inhomogeneous (or full two-fluid) models and homogeneous (or single fluid) models.

In the inhomogeneous assumption, each of the phases is modelled separately and therefore for each phase, a different set of conservation laws are considered and solved [19, 20]. In this model, the exchange of mass, momentum and energy between phases are treated explicitly as transfer terms. Therefore, the inhomogeneous model can provide the physical details occurring at the cavitation interface such as mass/energy exchange, thermal transfer and even surface tension [16].

In the homogeneous model, it is assumed that the phases share the same properties at each point of the flow, such as pressure, velocity, and temperature. Therefore, the flow can be modelled by solving a single set of mass, momentum and energy equations. The mixture density then can be calculated by using different possible options such as state equation, barotropic equation, or transport equation model.

In the state equation approach, the thermodynamic state law is employed to provide a relation between the density, pressure and temperature [11, 21, 22, 23].

Since using an isothermal assumption in cavitation simulation is reasonable, it is

possible to use a relation between pressure and density (i.e. barotropic equation) instead of the state law equations. Because of simple implementation, this approach is attractive and has been used widely [24, 25, 26]. However, since using the barotropic equation creates a parallel prediction between pressure and density, it fails to capture some fundamental fluid physics such as the vorticity production which is an important aspect of cavitating flows, especially in the closure region [16, 27].

In the homogeneous approach, another method in modelling and calculating the mixture density is using the transport equation model (TEM). In this model the mass transfer between liquid and vapour is modelled using source terms. In most of the applications of this model, the transport of volume or mass of either liquid or vapour is modelled. Then the transport equation is considered with mass, momentum and energy equations of the mixture fluid to close the governing equations. Different models have been proposed to model the mass transfer rate in TEM. Derived from the Rayleigh-Plesset equation, Sauer and Schnerr proposed a model based on the dynamics of a single bubble [28, 29]. In order to improve the phase change modelling, some author have proposed models derived from the Rayleigh-Plesset equation which includes empirical coefficients [30, 31]. Some of the proposed models are based on the practical methodology of using effective parameters and then using empirical factors in order to adjust the mass transfer between liquid and vapour phases [32, 33]. In order to get rid of the empirical constants, a model was proposed by Senocak and Shyy to explicitly calculate the coefficients of the mass transfer model from the interfacial velocity terms [34, 35, 36].

The main advantages of TEM is the convective characteristics of the model which allows appropriate modelling of the cavity detachment and also cavity closure. In contrast to the barotropic models, in TEM approaches, the density is a function of the transport process. Consequently, gradients of density and pressure are not necessarily parallel, suggesting that the model can accommodate the vorticity production term as highlighted by recent experimental studies [27].

The main drawback of TEM comes from the source terms and phase change rate modelling. If the source term parameters (e.g. empirical coefficients, bubble density, bubble size, etc.) are not properly set, the accuracy of the numerical predictions can be significantly affected. In the next sections these conditions are investigated and the effects of the phase change rate on the final results are highlighted.

1.5 Objectives and studies of the present research

The current work focuses on the analysis and simulation of cavitation by using a multiphase LES method. The investigated mechanisms are related to cavitation formation and development which have direct effects on the flow structure and characteristics such as forces distributions, pressure pulse, noise, vibration and

erosion risk. Experimental observations can provide appropriate information regarding the occurrence of cavitation but this information is limited to the visual observations and possibly pressure pulse measurements. As a results, this information will indicate only the possible existence of a certain problem and gives limited guidance regarding how to redesign. Numerical simulation can provide further detailed view of the flow strcuture. The gained understandings and knowledge can contribute to preventing or reducing negative effects of cavitation and therefore improving performance of propulsion systems.

Previous studies on the numerical simulation of cavitating flows using LES performed by Huuva [37] and Lu [38] are encouraging and promising. In these results the global mechanisms of cavitation are well captured in the simulation. The current work, therefore, is focused on using and also developing the previous computational methodology for cavitating flows simulation. The main objectives of the current work can be listed as follows:

1. To check the capability of the methodology in predicting the cavitation pattern and the large scale two-phase mechanisms that interact with collapse, erosion risk, noise, and performance degradation of propulsor systems;
2. Mass transfer modelling improvement by considering the shear stresses in the liquid rupturing and the local flow time scale in computing the mass transfer rate;
3. Investigation of mesh resolution effects on cavitation prediction (formation, development, transfer and collapse);
4. Apply the numerical methodology in engineering configurations in order to provide further knowledge for guiding the development of design principles.

To work towards these objectives, several studies have been performed in this work:

1. NACA0009 hydrofoil
Numerical simulation of cavitation is performed on the two dimensional geometry of NACA0009 hydrofoil with the emphasis on the Schnerr-Sauer mass transfer model parameters setup. Different configurations for number of nuclei and diameter are considered, and for each setup the accuracy of the results are investigated by comparing the pressure distribution and cavity size with the available experimental data. The proposed modification for calibration of the mass transfer rate based on the local flow time scale is tested, and verified for this case.
2. NACA66MOD hydrofoil
The first study of the mesh resolution effects on the cavitation simulation

and force distribution is conducted by the simulation of two dimensional geometry of NACA66MOD hydrofoil. Three different operation conditions are simulated and for each condition the accuracy of cavity size and pressure distribution prediction are analyzed. The effects of the mesh resolution on the cavity closure region is investigated for one condition, and its effects on the pressure distribution is highlighted.

3. Twisted Delft hydrofoil

The mesh resolution study on the cavitation prediction is elaborated by numerical simulations conducted on the three dimensional geometry of Twisted Delft hydrofoil. Effects of mesh resolution in streamwise, spanwise and also normal to wall (y^+) directions on the flow predictions are investigated in both wetted and cavitating flows. Drag force, pressure distribution and cavitation pattern are studied and compared with the experimental data. For one case, effects of the outlet boundary location on the flow prediction are studied. Effects of the shear stresses on the liquid rupturing (pressure threshold modification) and also calibration of mass transfer rate are also investigated. Moreover, the importance of the spatial mesh resolution on transformation of the separated two-phase vortex and its strength preservation is highlighted. It is shown that the correct prediction of collapse (location and pressure induced pulses) of the separated cavity requires very high spatial mesh resolution.

4. E779A propeller

The computational methodology for cavitating propeller simulation is validated by a study on the E779A propeller in wetted and cavitating conditions. The selected operating conditions have undisturbed inflows. Since the propeller rotational axis is in the inflow direction, it constitutes a steady cavitating condition. Therefore, for this case it would be less demanding to test the moving mesh strategy and also mass transfer modelling accuracy. Open-water performance prediction in wetted and cavitating flows, and cavitation pattern are analyzed for this case. The results are also compared with the published numerical results, and it is highlighted that different calibrated mass transfer models lead to similar cavitation prediction in this case.

5. PPTC SMP' 15 propeller

In order to elaborate the numerical simulation of cavitating propellers to more complex flows, the PPTC SMP' 15 propeller is simulated in three different cavitation conditions. Since the propeller shaft is inclined towards the inflow direction by 12 degrees, the load on the blades varies by their angular positions which leads to unsteady cavitation pattern on the blades. Effects of the inlet distance, time scheme, and mesh resolution are studied for this propeller. For each operating condition, the wetted and cavitating flows are simulated, and open-water performance characteristics of the propeller are analyzed. The cavitation pattern on the pressure side and suction sides of

the blades are investigated and compared with the available experimental data.

6. Rolls Royce high skew propellers

Two high skew propellers operating in open water conditions on inclined shaft are simulated to investigate the effects of design differences on the flow features and cavitation pattern. Open-water performance and cavitation pattern are highlighted. For the second propeller, two different mesh topologies are tested and dependency of the cavitation pattern and cavity shape on the local mesh resolution are investigated.

1.6 Thesis outline

Following the present chapter, the thesis is structured as follows:

In Chapter 2, the governing equations of two-phase cavitating flows are described where by taking advantage of homogeneous assumption the two-phase mixture is modelled via the effective fluid. The phases are considered incompressible, isothermal and immiscible. The transport equation is used to calculate the distribution of each phase. The concept of ILES is also presented and briefly discussed. In Chapter 3, numerical methods are presented. The OpenFOAM software is introduced, and the modified interPhaseChangeFoam solver used for simulation of cavitation in this work is described. The implementation of Schnerr-Sauer mass transfer model in the solver is explained by using the same notation as OpenFOAM. The derivation of the pressure correction equation and its coupling with the mass transfer source term is explained. Finally, the solution strategy used to create coupling between different equations in the segregated approach is provided.

In Chapter 4, two proposed modifications for better prediction of cavitation are presented. In the first part of the chapter, the concept of the phase change time scale is explained, and negative effects of its miscalculation on the cavitation predictions are highlighted. It is discussed that the velocity strain time scale can be an appropriate choice to improve the prediction of the phase change rate based on the flow local properties. In the second part of the chapter, the effects of the shear stresses on the liquid rupturing previously investigated by the other researchers are discussed and extended to marine applications.

In Chapter 5, numerical simulations of NACA0009 hydrofoil, NACA66MOD hydrofoil, and Twisted Delft hydrofoil flows are presented. The hydrofoils are simulated in wetted and cavitating flows. Effects of mass transfer modelling setup, proposed modifications, computational domain size, and mesh resolution on the flow behaviour and cavitation pattern are investigated. Dependency of results to the mesh resolution at the closure region, the accuracy of transforming the separated two-phase vortex and also cavity collapse on the spatial mesh resolution are highlighted in this chapter.

In Chapter 6, numerical simulations of the propellers are presented: E779A pro-

propeller, PPTC SMP'15 propeller and the Rolls Royce high skew propellers are investigated at different operating conditions. Effects of mesh resolution, computational setup and design changes on the flow structure and cavitation pattern are analyzed in this chapter.

In Chapter 7, a summary and suggestions for future work are presented.

2

Governing equations

In the current study, the Euler-Euler approach, or linear mixture approach, along with the interface capturing method has been employed. With this assumption, the two-phase flow can be simulated by modelling the effective-fluid properties. Moreover, it is assumed that the mean fluid and each phase are incompressible and isothermal which is a common approach when simulating cavitating flows. Transport equation of volume fraction (TEM) is used to model the phases distribution, based on the VOF, Volume of Fraction, method. Therefore, the governing equations consist of continuity of mass and momentum and also TEM to predict the phases' distribution.

2.1 Mass and momentum continuity equations

The conservation equations of mass and momentum (in Cauchy description) for the mean fluid can be written as follow,

$$\frac{\partial \rho_m}{\partial t} + \frac{\partial(\rho_m u_i)}{\partial x_i} = 0, \quad (2.1)$$

$$\frac{\partial(\rho_m u_i)}{\partial t} + \frac{\partial(\rho_m u_i u_j)}{\partial x_j} = \frac{\partial \tau_{ij}}{\partial x_j} + \rho_m g_i. \quad (2.2)$$

The stress tensor of Newtonian fluids is conventionally written in the form of summation of pressure stress and shear stresses. In this presentation, it is assumed that effects of the bulk viscosity of the fluid is negligible.

$$\tau_{ij} = -p\delta_{ij} + S_{ij} - \frac{2}{3}\mu_m \frac{\partial u_k}{\partial x_k} \delta_{ij} \quad (2.3)$$

$$S_{ij} = 2\mu D_{ij} \quad (2.4)$$

Here p is the static pressure, ρ_m and μ_m are the effective (mixture) density and viscosity, S is the viscous stress tensor and $D_{ij} = \frac{1}{2}(\frac{\partial u_i}{\partial x_j} + \frac{\partial u_j}{\partial x_i})$ is the deformation rate tensor (symmetric part of the velocity gradient), respectively.

2.2 Mass transfer modelling

As described before, one approach to model the phase distribution is using a transport equation for volume or mass fraction. In this work, the transport equation of liquid volume fraction is solved along with a source term to mimic the mass transfer between liquid and vapour. Using the volume fraction function, it is possible to calculate the mixture density and mixture viscosity based on the homogenous flow assumption.

$$\rho_m = \alpha_l \rho_l + (1 - \alpha_l) \rho_v, \quad \mu_m = \alpha_l \mu_l + (1 - \alpha_l) \mu_v \quad (2.5)$$

$$\frac{\partial \alpha_l}{\partial t} + \frac{\partial(\alpha_l u_i)}{\partial x_i} = \frac{\dot{m}}{\rho} \quad (2.6)$$

$$\frac{\partial u_i}{\partial x_i} = \left(\frac{1}{\rho_l} - \frac{1}{\rho_v}\right) \dot{m} \quad (2.7)$$

In Equation 2.6, which represents the transport equation of liquid volume fraction, the source term is the rate of mass transfer between vapour and liquid phases. Since the OpenFOAM package is utilized for solving the equations, similar notation is employed here for TEM. As it can be seen from Equation 2.7, in cavitating flows, due to the phase change, the flow is not divergence free, and therefore special considerations should be taken in solving the pressure correction equations.

2.3 Turbulence modelling

For turbulence modelling, the implicit Large Eddy Simulation approach, ILES, is used. This model has been previously used successfully for simulating cavitating flows [37, 39, 40, 41, 42]. Using the low pass filtering approach, the momentum equation in LES model can be written as,

$$\frac{\partial(\rho_m \bar{u}_i)}{\partial t} + \frac{\partial(\rho_m \bar{u}_i \bar{u}_j)}{\partial x_j} = -\frac{\partial \bar{p}}{\partial x_i} + \frac{\partial}{\partial x_j} (\bar{S}_{ij} - B_{ij}) + \rho_m g_i, \quad (2.8)$$

where the over bar denotes low pass filtered quantities. In this equation, $B_{ij} = \rho(\bar{u}_i \bar{u}_j - \bar{u}_i \bar{u}_j)$ is the subgrid stress tensor. In ILES, no explicit model is applied for \mathbf{B} , instead the numerical dissipation is considered enough to mimic the action of \mathbf{B} [37, 39, 40]. Therefore, for the momentum convection term, a somewhat dissipative scheme should be used to provide appropriate numerical diffusion in the solution procedure.

3

Numerical Methods

3.1 OpenFOAM Package

OpenFOAM (Open Source Field Operation and Manipulation) is an open source code written in C++ to model and simulate fluid dynamics and continuum mechanics. It is possible to adopt the code and build new functionalities, libraries, solvers, and utilities. The software is community driven where various communities are working on different fields of applications. This has expedited the progress and development of the software. Another advantage is the ability to use the software in parallel.

In OpenFOAM, the spatial discretization is performed using a cell centered collocated finite volume (FV) method for unstructured meshes with arbitrary cell-shapes, and a multi-step scheme is used for the time derivatives. To complete the FV-discretization the face fluxes need to be reconstructed from grid variables at adjacent cells, requiring interpolation of the convective fluxes and difference approximations for the inner derivatives of the diffusive fluxes; see Weller et al. [43], Jasak [44] and Rusche [45] for more details on the discretization and the numerics used in OpenFOAM. In this work, the OpenFOAM version 2.3.x is used.

3.2 Modified interPhaseChangeFoam solver

InterPhaseChangeFoam is a solver for two incompressible, isothermal, immiscible fluids with phase-change (i.e. cavitation) which uses a VOF (Volume of Fluid) phase-fraction based interface capturing approach. The set of phase-change models provided are designed to simulate cavitation but other mechanisms of phase-change are supported within this solver framework. Turbulence modelling is generic, i.e. laminar, RAS, or LES may be selected. More details about this solver can be found in the open access literature [46].

3.2.1 Schnerr and Sauer cavitation model

There are several cavitation phase change models implemented in OpenFOAM 2.3.x package, e.g. Schnerr-Sauer [28], Kunz [32], and Merkle [33] models. Here the description of the Schnerr-Sauer model which has been used for the current research, is presented and its relation with the other parts of the code is also explained.

The Schnerr-Sauer model assumes that there are several vapour bubbles, also called nuclei, inside the liquid which act as the initial sources of the phase change, and cavitation inception occurs due to their presence. The number, size and distribution of these bubbles can be determined in water quality experiment tests. To simplify the numerical modelling, it is assumed that the initial nuclei have been distributed evenly throughout the liquid, and they have equal size which is the smallest size that vapour bubbles can have.

The volume of nuclei, its volume fraction, and the radius of bubble can be described through Equations 3.1, 3.2 and 3.3. In these equations, n_0 is the number of nuclei in one cubic meter of liquid, and d_{Nuc} is the diameter of the nuclei. The radius of the bubble, R_B , is modified based on the notation used in OpenFOAM to consider the effects of initial nuclei volume fraction, α_{Nuc} .

$$\text{Vol}_{Nuc} = \frac{\pi n_0 d_{Nuc}^3}{6} \quad (3.1)$$

$$\alpha_{Nuc} = \frac{\text{Vol}_{Nuc}}{1 + \text{Vol}_{Nuc}} = \frac{\frac{\pi n_0 d_{Nuc}^3}{6}}{1 + \frac{\pi n_0 d_{Nuc}^3}{6}} \quad (3.2)$$

$$R_B = \sqrt[3]{\frac{3}{4\pi n_0} \frac{1 + \alpha_{Nuc} - \alpha_l}{\alpha_l}} \quad (3.3)$$

Depending on the local properties of the flow, in the matrix of the discretized volume fraction transport equation, the source term can become very large compared to the diagonal part due to the very high phase change rate. This may make solving the discretized equations matrix problematic [28]. In order to improve the solution stability, the source term needs to be rewritten, Equation 3.4, so the diagonal part can take into account some parts of the source term as an implicit term.

$$\frac{\partial \alpha_l}{\partial t} + \frac{\partial(\alpha_l \bar{u}_i)}{\partial x_i} = \frac{\dot{m}}{\rho_l} = \frac{\dot{m}}{\rho_l} - \alpha_l \left(\frac{1}{\rho_l} - \frac{1}{\rho_v}\right) \dot{m} + \alpha_l \left(\frac{1}{\rho_l} - \frac{1}{\rho_v}\right) \dot{m} \quad (3.4)$$

Considering the non-conservative form of the mass continuity equation, the last

term in Equation 3.4 can be replaced with the divergence of velocity,

$$\frac{\partial \alpha_l}{\partial t} + \frac{\partial(\alpha_l \bar{u}_i)}{\partial x_i} = \left(\frac{1}{\rho_l} - \alpha_l \left(\frac{1}{\rho_l} - \frac{1}{\rho_v}\right)\right) \dot{m} + \alpha_l \frac{\partial \bar{u}_i}{\partial x_i}. \quad (3.5)$$

The phase change model can be also decomposed in two terms, one for condensation and the other for vapourization modelling.

$$\dot{m}_{\alpha c} = C_c \alpha_l \frac{3\rho_l \rho_v}{\rho_m R_B} \sqrt{\frac{2}{3\rho_l}} \sqrt{\frac{1}{|p - p_{\text{threshold}}|}} \max(p - p_{\text{threshold}}, 0) \quad (3.6)$$

$$\dot{m}_{\alpha v} = C_v (1 + \alpha_{\text{Nuc}} - \alpha_l) \frac{3\rho_l \rho_v}{\rho_m R_B} \sqrt{\frac{2}{3\rho_l}} \sqrt{\frac{1}{|p - p_{\text{threshold}}|}} \min(p - p_{\text{threshold}}, 0) \quad (3.7)$$

$$\dot{m} = \alpha_l \dot{m}_{\alpha v} + (1 - \alpha_l) \dot{m}_{\alpha c} = \alpha_l (\dot{m}_{\alpha v} - \dot{m}_{\alpha c}) + \dot{m}_{\alpha c} \quad (3.8)$$

By introducing $\dot{V} = \left(\frac{1}{\rho_l} - \alpha_l \left(\frac{1}{\rho_l} - \frac{1}{\rho_v}\right)\right) \dot{m}$ and putting Equation 3.8 inside Equation 3.5, the transport equation can be rewritten as,

$$\frac{\partial \alpha_l}{\partial t} + \frac{\partial(\alpha_l \bar{u}_i)}{\partial x_i} = \left(\frac{\partial \bar{u}_i}{\partial x_i} + \dot{V}_v - \dot{V}_c\right) \alpha_l + \dot{V}_c. \quad (3.9)$$

Accordingly, the source term is decomposed into two terms where the first one can be considered implicitly to improve the robustness of the solution.

3.2.2 Pressure correction equation

The general form of Navier-Stokes equation is presented in Equation 3.10. Here, we will continue with the finite volume discretized form of this equation, Equation 3.11. Details of the discretization of each term of this equation can be found in [44, 47].

$$\frac{\partial(\rho_m u_i)}{\partial t} + \frac{\partial(\rho_m u_i u_j)}{\partial x_j} = -\frac{\partial p}{\partial x_i} + \frac{\partial}{\partial x_j} \left(\mu \frac{\partial(u_i)}{\partial x_j}\right) + B_i \quad (3.10)$$

$$a_p U_p = \sum a_{NB} U_{NB} - \Omega \nabla p + \Omega B \quad (3.11)$$

In Equation 3.11, the pressure field is related to the previous iteration (or time step), a_p and a_{NB} are also related to the cell and its neighbouring cells, and Ω is the volume of the cell. All of the values in this equation are related to the cell centre values which have been noted by the subscript p . It should be noted that since a_p and a_{NB} convey the non-linearity of the convection term, they are dependent on the velocity field.

By diving Equation 3.11 by a_p , we get,

$$U_p = H[U]_p - D_p p, \quad (3.12)$$

where $H[U]$ and D_p are defined by

$$H[U]_p = \frac{\sum a_{NB} U_{NB} + \Omega B}{a_p}, \quad (3.13)$$

$$D_p = \frac{\Omega \nabla p}{a_p}. \quad (3.14)$$

By solving Equation 3.15, the new velocity field U^* is obtained. In order to solve this equation, $H[U]$ and D_p operators should be calculated by the available velocity fields from previous iteration or time step,

$$U_p^* = H[U^*]_p - D_p p^0 \quad (3.15)$$

The pressure equation is derived by applying the divergence operator on Equation 3.12, considering the newly obtained velocity field, U^* ,

$$\nabla \cdot (U_p^*) = \nabla \cdot (H[U^*]_p - D_p p) = \nabla \cdot H[U^*]_p + \nabla \cdot (-D_p p). \quad (3.16)$$

The divergence of the velocity in the cavitating flows is non-zero due to the phase change. Therefore, the divergence of the velocity field, $\nabla \cdot (U_p^*)$, can be replaced by the phase change term.

$$\nabla \cdot H[U^*]_p + \nabla \cdot (-D_p p) = \left(\frac{1}{\rho_l} - \frac{1}{\rho_v} \right) \dot{m} \quad (3.17)$$

In the interPhaseChangeFoam solver, the term related to the phase change, $\left(\frac{1}{\rho_l} - \frac{1}{\rho_v} \right) \dot{m}$, is decomposed in a way that some portions of this term can be handled implicitly, similarly to what was described for the vapor volume fraction equation. By defining $\dot{m}_p = \dot{m} / (p - p_{\text{threshold}})$, \dot{m}_p can be written as $\dot{m}_p = \dot{m}_{pv} - \dot{m}_{pc}$ where these two terms defined via Equations 3.18 and 3.19. In these equation, the pos function returns plus one when the input is positive and zero otherwise, and the neg function returns minus one when the input is negative and zero otherwise.

$$\dot{m}_{pc} = C_c \alpha_l (1 - \alpha_l) \frac{3\rho_l \rho_v}{\rho_m R_B} \sqrt{\frac{2}{3\rho_l}} \sqrt{\frac{1}{|p - p_{\text{threshold}}|}} \cdot \text{pos}(p - p_{\text{threshold}}) \quad (3.18)$$

$$\dot{m}_{pv} = -C_v \alpha_l (1 + \alpha_{\text{Nuc}} - \alpha_l) \frac{3\rho_l \rho_v}{\rho_m R_B} \sqrt{\frac{2}{3\rho_l}} \sqrt{\frac{1}{|p - p_{\text{threshold}}|}} \cdot \text{neg}(p - p_{\text{threshold}}) \quad (3.19)$$

Then by introducing \dot{V}_p as Equation 3.20, the pressure equation can be rewritten as Equation 3.21.

$$\dot{V}_p = \left(\frac{1}{\rho_l} - \frac{1}{\rho_v} \right) \dot{m}_p \quad (3.20)$$

$$\begin{aligned}\nabla.H[U^*]_p + \nabla.(-D_p p) &= (\dot{V}_{pv} - \dot{V}_{pc})(p - p_{threshold}) = \\ &= (\dot{V}_{pv} - \dot{V}_{pc})p - (\dot{V}_{pv} - \dot{V}_{pc})p_{threshold}\end{aligned}\quad (3.21)$$

The first term in the L.H.S. of Equation 3.21 can now be handled implicitly, while the other term needs to be computed explicitly. By solving this equation, a new pressure field can be obtained. Since this pressure field is an intermediate results, let's call it p^* . The velocity field is updated using these newly computed pressure field,

$$U_p^{**} = H[U^*]_p - D_p p^*. \quad (3.22)$$

3.2.3 Solution Strategy

The final solution algorithm thus becomes, see also Figure 3.1:

1. Initialization of velocity, pressure and volume fraction fields.
2. Calculate the viscosity and density fields based on the volume fraction field and each phase's properties.
3. Calculate the time step.
4. Compute the coefficients, a_p and a_{NB} , of the algebraic discretized momentum Equation (i.e. update the fluxes), Equation 3.11.
5. Compute the pressure gradients and body forces, Equation 3.11.
6. Solve Equation 3.15 to obtain new velocity field U^* .
7. Compute the mass transfer source term and H operator, Equation 3.17.
8. Solve the pressure Equation 3.17 to obtain new pressure field, p^* .
9. Update the velocity field using Equation 3.22.
10. Based to the number of non-orthogonality correction, go back to step 8.
11. Based to the number of solving pressure Equation (PISO loop), go back to step 7.
12. Solve equations related to the turbulence modelling and update the effective viscosity.
13. Solve the liquid volume fraction transport equation, and update the mixture density and viscosity fields, Equation 3.9.
14. Based on the number of PIMPLE iterations, go back to step 2.

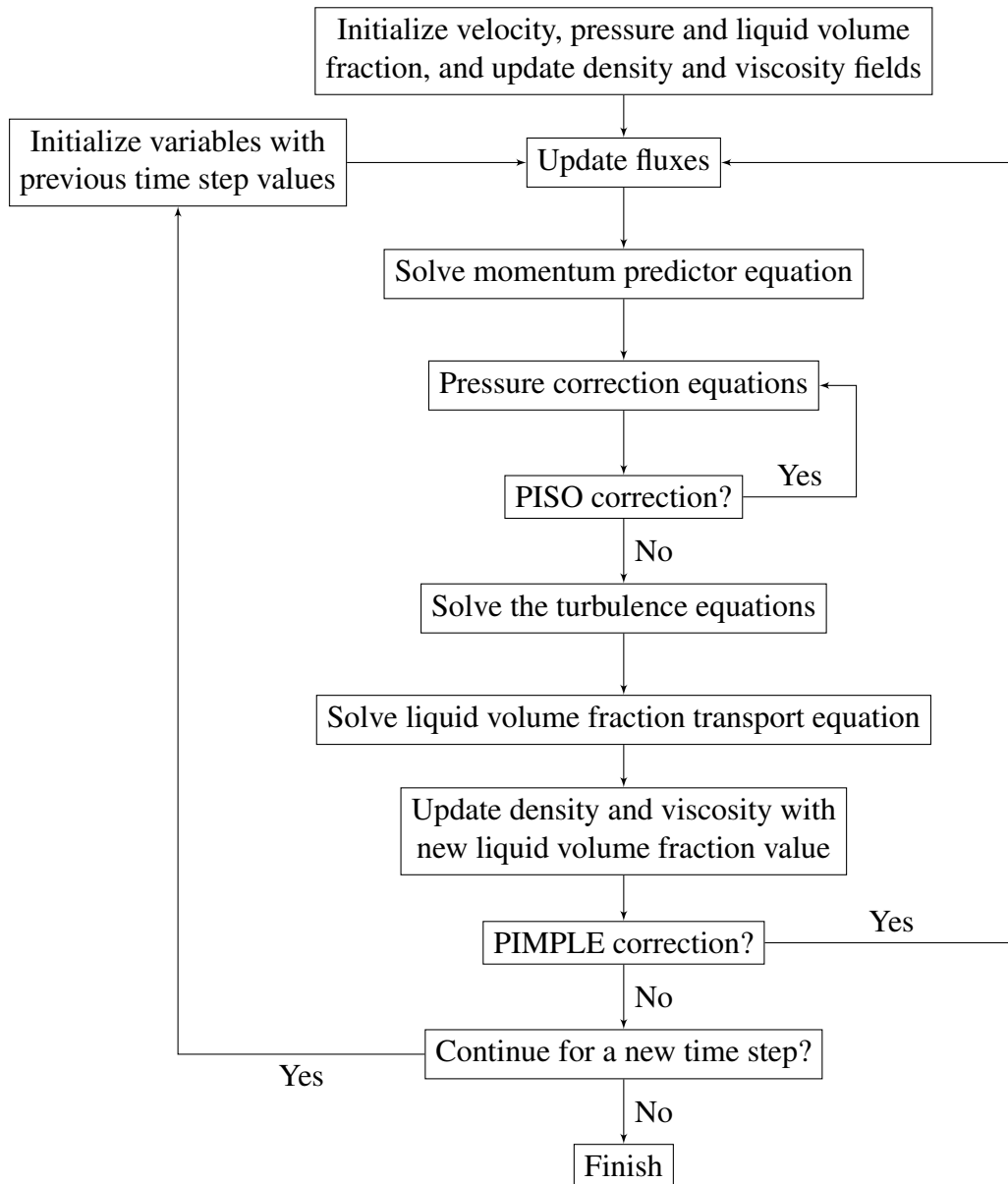


Figure 3.1: Cavitation Solver Algorithm

4

Sheet Cavity Inception Modelling

4.1 Phase change time scale

Pure liquids, e.g. water, can withstand low pressure and even negative pressure without undergoing any cavitation formation. In pure liquids, the inner molecular forces and bonding between the molecules are very strong and therefore stronger forces are required to break this bonding. In such a condition, the liquid can withstand the tension meaning that even by being exposed to negative pressure the liquid does not transfer into vapour. Presence of nuclei inside a liquid can change the strength of the inner molecular forces and bonding among them, making them weaker comparing to the pure status. As a result, the cavitation inception is strongly dependent on the presence of these weak spots, i.e. nuclei, inside the liquid. Although presence of nuclei can expedite the formation of cavitation, it is not the only effective parameter. Some studies have shown that in some circumstances where the viscous effects dominate the flow behaviour even in the presence of enough nuclei the liquid can withstand pressure lower than the saturation pressure without undergoing any phase change, [9, 48, 49]. In a flowing liquid, the viscous effects become important when either the viscosity or velocity gradients are large enough to create considerable shear stresses.

It has been observed that on smooth surfaces, for example a smooth leading edge, the cavitation interface detachment point is located downstream of the laminar boundary layer separation point. Due to the adverse pressure gradient downstream of the boundary layer separation point, the pressure at the cavity detachment point is higher than the separation point, thus means that cavitation has not started at the location with the lowest pressure, the separation point. The distance between the boundary layer separation point and cavity detachment point is reported to be related to the flow Reynolds number which represents contribution of the scale effects on the cavitation behaviour [4]. Therefore, in some experimental tests, in order to reduce the scale effects and eliminate the complexity of interaction

of laminar boundary layer and cavitation, roughness is applied right at the leading edge to prevent any development of the laminar boundary layer and force the flow transition into turbulent flow. As a result, in the tripped boundary layer the location of the minimum pressure and the cavitation onset are almost the same. However, it should be noted that the leading edge roughness not only changes the location of the cavitation inception but also can influence cavitation dynamics and its erosion aggressiveness making it much more sophisticated to be modelled via CFD tools [50].

One of the main issues in the simulation of cavitating flows using TEM is choosing the phase change model coefficients [17]. These coefficients represent the relaxation time that vapour or liquid phase needs to transfer into the other phase. For instance in the phase change models which are developed based on the bubble dynamics [1], the derivative of the bubble radius over time represents the relaxation time. However, when the region covered with vapour is larger than one bubble, using this term as the relaxation time may no longer correctly represent the accurate time scale of the phase change making it necessary to modify the coefficients. The chosen values for these coefficients therefore will have direct effects on the final results. Another issue which should be taken into account is the dependency of the cavitation characteristics to the local flow properties. Using constant coefficients for mass transfer modelling, or in another word phase change relaxation time, without considering the local properties may impose unrealistic constrains. So, since the cavitation and phase change rate interact locally with the flow properties, one can expect a correlation between flow local time scales and the phase change relaxation time.

One option for the time scale can be the main flow non-dimensional time scale which has been tried previously, [32]. However, since it is a constant value throughout the flow domain, it is not a perfect choice for phase change relaxation time scale which has a strong relation with local flow parameters. For cases where the cavitating flow is fully turbulent, like flow around a hydrofoil having roughness on the leading edge, turbulent time scales can be the next choice. Turbulent time scales consist of many scales ranging from the main flow time scale to the Kolmogorov time scale, which is related to the smallest eddy time scale. In linear turbulence models, it has been assumed that the turbulence stresses have direct relation with the symmetric part of the velocity strain rate [51]. Using the similar analogy here, the symmetric part of the velocity strain rate is proposed to be considered for correction of the local phase change relaxation time scale.

Since the modified coefficient is usually bigger than one, using this modification for coefficients will increase the rate of condensation and evaporation. It has been observed that in cavitating flows, the vapour production coefficient should be large, as high as possible according to [52], to satisfy near instantaneous evaporation. The destruction term, however, allows for some retardation in the condensation [52]. Therefore, the coefficient modification is limited to the evaporation coefficient, C_v where the main flow time scale, $t_\infty = \frac{L_\infty}{U_\infty}$, is employed to normalize the velocity strain rate,

$$C_{v\text{-mod}} = C_v \left(1 + t_\infty \left| \frac{1}{2} \left(\frac{\partial u_i}{\partial x_j} + \frac{\partial u_j}{\partial x_i} \right) \right| \right). \quad (4.1)$$

4.2 Viscous shear stress effects

The thermodynamic saturation pressure is calculated in conditions where the fluid is completely steady and in equilibrium state during the phase change. Therefore, the rupture of the liquid pocket is just due to the pressure tensile, and effects of the shear stresses are neglected. In the static or quasi static conditions where the static pressure in major part of the liquid is much larger than the viscous shear stresses, this assumption is reasonably accurate, but not for regions of the flow where viscous shear stresses are considerable and can be comparable with the static pressure. A criterion of maximum tension which unifies the theory of cavitation, the theory of maximum tensile strength of liquid filaments, and the theory of fracture of amorphous solids, was proposed the first time by Joseph [53, 54]. Later on, a few researchers continued to investigate effects of shear stresses on cavitating nozzle flows and therefore development of this model stayed limited to high speed flows where flows speed were as high as 100 m s^{-1} [55, 56]. In this research, considering viscous shear stresses in the calculation of the pressure threshold has been extended into marine applications, e.g. propellers and 3D hydrofoils. For these applications due to the high gradient of the velocity, the shear stresses are considerable at the leading edge which is the source of vapour generation and also at the cavity closure region which is the cavity collapse region. In order to consider the viscous stresses in the liquid rupturing, the maximum eigenvalues of the stress tensor should be considered as the criteria that the flow withstands against rupturing or phase change, $\max(\tau_{ij}) < p_{\text{Sat}}$, where

$$\tau_{ij} = \begin{bmatrix} -p + S_{11} - \frac{2}{3}\mu \frac{\partial u_i}{\partial x_i} & S_{12} & S_{13} \\ S_{21} & -p + S_{22} - \frac{2}{3}\mu \frac{\partial u_i}{\partial x_i} & S_{23} \\ S_{31} & S_{32} & -p + S_{33} - \frac{2}{3}\mu \frac{\partial u_i}{\partial x_i} \end{bmatrix}. \quad (4.2)$$

Note that in a stationary fluid, the eigenvalues of the stress tensor are the same, and equal to the static pressure. Generally the eigenvalues of the stress tensor are equal to the diagonal terms of the tensor transformed into the principal coordinate. As it can be seen from Equation 4.2, calculation of the eigenvalues of the stress tensor for all of the computational cells will demand a significant computational cost. To simplify the calculation, one can use the same methodology used in the turbulence models where the maximum viscous stress tensor is assumed to be of the same order as the shear strain rate, $\dot{\gamma}$, in $\dot{\gamma} = \sqrt{2D_{ij}D_{ij}}$. Shear strain rate represents the rate of change in strain (deformation) of the flow with respect to time. It comprises both the rate at which the flow is expanding or shrinking (i.e. the expansion rate), and also the rate at which the flow is being deformed by progressive

shearing without changing its volume (the shear rate). Therefore, the magnitude of stress tensor in its principal coordinates can be estimated by,

$$|\tau_{ij}| = |-p\delta_{ij} + S_{ij}| \approx |-p\delta_{ij} + \mu\dot{\gamma}\delta_{ij}|. \quad (4.3)$$

Using this simplification, the pressure threshold, which determines the onset of cavitation in the flowing fluid, can be written as,

$$p - \mu\dot{\gamma} < p_{\text{Sat}}, \quad (4.4)$$

$$p_{\text{threshold}} = \mu\dot{\gamma} + p_{\text{Sat}} = p_a + p_{\text{Sat}}. \quad (4.5)$$

This added pressure, $p_a = \mu\dot{\gamma}$, is important if either shear strain rate or effective viscosity is large, and comparable with the saturation pressure. For the flow around the foils, this is the case near the leading edge or during the collapse when the velocity variation is very high, and for the flow around the propellers this is the case both at the tip and leading edge regions.

5

Numerical Results - 2D and 3D hydrofoils

This chapter contains the results of numerical simulations around NACA0009 hydrofoil, NACA66MOD hydrofoil and Twisted Delft hydrofoil. These cases have been used widely as the benchmarks to test and validate the capabilities of numerical tools in prediction of cavitation. The current simulations are performed in order to address and test the accuracy of computational algorithm in prediction of cavitating flows, the effects of mass transfer rate on the cavitation prediction, mesh resolution requirement for cavitation prediction with emphasis on the cavitation inception and collapse, and to validate the proposed modifications for pressure threshold and mass transfer calibration.

5.1 NACA0009

The Schnerr-Sauer phase change model requires that the initial number of nuclei and initial nuclei diameter are predefined to adjust the phase change rate. A modification is proposed by Kim and Brewton[57] to also include two coefficients in the model to manually calibrate the mass transfer between phases. In order to investigate effects of the phase change model parameters and coefficients on cavitation behaviour, the cavitating flow around NACA0009 is considered. The experimental tests have been done in EPFL at different velocity speeds and cavitation numbers [18]. The main interest here is to test effects of number of nuclei and diameter on the cavitation development in a semi-steady flow over a simple geometry. The threshold pressure modification and also the phase change rate modification are also tested in this section. Since the experimental data do not report time dependency, time averaged numerical results are used for comparison and verification.

5.1.1 Experimental setup

The experimental tests of cavitation over NACA0009 hydrofoil are performed in EPFL cavitation tunnel, Figure 5.1. The rectangular test section of the tunnel has inner dimensions of 150 x 150 x 750 mm. Typical tested hydrofoils tested in this tunnel have chord length of 100 mm and a maximum span of 150 mm, corresponding to the width of the test section, for more details see [18, 58].

For the experiment test, the foil geometry is truncated at 90% of the original chord length which the final foil has 100 mm chord length and 150 mm span length to fit the test tunnel in EPFL. Hydrodynamic forces, pressure, and velocity profiles are measured at different sections of the foil during the experiment. The foil is especially constructed for the pressure measurements. 19 x 3 pressure sensors at three different sections of the foil are installed to measure the pressure. The velocity profiles are also measured using two components LDV technique. Cavitation and flow characteristics have been measured at different operating conditions including different angles of attack, cavitation numbers, and inlet velocities during the experiment. Detailed information about the experimental procedure, including the different filtering and correction techniques, can be found in [58]. In this work, the focus is in simulation of the operating condition having inlet velocity $15m/s$, outlet cavitation number $\sigma = 0.75$, and foil angle of attack 4 degree.

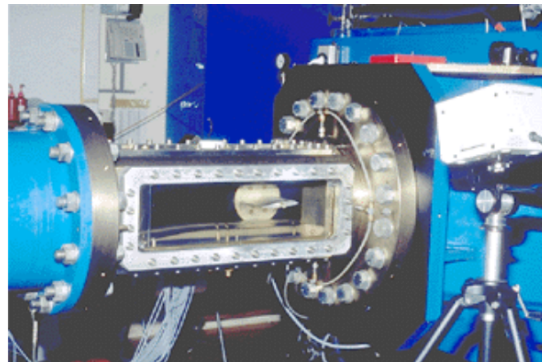


Figure 5.1: EPFL high speed cavitation tunnel[18]

5.1.2 Numerical setup

Considering the steady two dimensional cavitation pattern observed in the selected operating condition, a 2D computational domain is considered for numerical simulation of NACA0009 hydrofoil, Figure 5.2. In the used configuration, the inlet is located 2C upstream of the foil, outlet is located 4C downstream of the foil and the tunnel height is 2C, where C is the chord length of the foil. The mesh consists of 24000 hexahedral cells which are clustered towards the foil surfaces. Moreover, finer resolution is provided near the leading edge and also trailing edge. The boundary conditions of the numerical simulation are described in Table 5.1. In order to avoid the effects of the tunnel walls, slip condition is applied for these

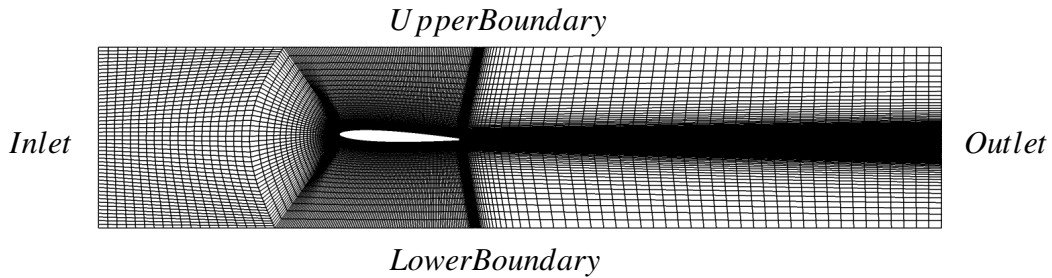
Table 5.1: Boundary conditions for cavitation simulation around NACA0009

boundary	velocity	pressure	nuSgs	alpha
Inlet	fixed value	zeroGradient	zeroGradient	fixed value
outlet	zeroGradient	fixed value	zeroGradient	zeroGradient
Foil	no slip	zeroGradient	Wall function	zeroGradient
Upper	slip	zeroGradient	zeroGradient	zeroGradient
Lower	slip	zeroGradient	zeroGradient	zeroGradient

Table 5.2: Investigated parameters for cavitation simulation around NACA0009

—	Fixed parameter(s)	Varied parameter(s)
Effects of nuclei number	$d_0 = 10^{-5}m$	$n_0 = 10^6, 10^8, 10^{10}, \text{ and } 10^{12}$
Effects of nuclei diameter	$n_0 = 10^8$	$d_0 = 10^{-3}, 5 * 10^{-4}, 10^{-4}, 10^{-5}, 10^{-6}, \text{ and } 10^{-7} m$
Modified coefficients	$n_0 = 10^8 \text{ and } d_0 = 10^{-5} m$	Coefficients

boundaries. The uniform inflow, $15m/s$, is used as the inlet boundary for velocity and constant pressure is applied to the outlet boundary condition to meet the flow cavitation number, $\sigma = 0.75$. In Table 5.2, the investigated parameters for cavitation simulation around NACA0009 at the selected operating condition are presented.

**Figure 5.2:** Cavitation simulation settings, NACA0009

5.1.3 Schnerr-Sauer model parameters tuning

In Figure 5.3, the pressure coefficient distribution over the foil is presented for different number of nuclei, $10^6, 10^8, 10^{10}, \text{ and } 10^{12}$. The nuclei diameter is kept constant equal to 10^{-5} for number of nuclei variation part. As it can be seen in this figure, using very small value for number of nuclei will lead to underprediction of the cavity. Moreover, at this condition the pressure at the leading edge becomes negative which can not be true for the foil with roughness applied on the leading edge. By increasing the number of nuclei, the accuracy of cavity size prediction and pressure distribution increases. For the current condition, it was noticed that increasing the number of nuclei to values higher than 10^{12} does not change the results any further. However, for different cases and different operating conditions

different values may be suitable.

Effects of nuclei diameter variation are presented in Figure 5.4. For these simulations the number of nuclei is kept constant equal to 10^8 . This relatively small value for number of nuclei has been selected in order to make the mass transfer rate more sensitive to the variation of nuclei diameter. Later on, the relation between the number of nuclei and mass transfer rate is discussed, and it is formulated how they are correlated.

Increasing the diameter of the nuclei will lead to larger cavity size, and better prediction of the pressure distribution. However, even for very big nuclei diameter, e.g. 10^{-3} m, still the accuracy of the results is very poor. The results also indicate that the mass transfer rate is more dependent on the number of nuclei than the nuclei diameter.

The quality of the water can be measured during the tests, and then the averaged number of nuclei and diameter can be used as phase change model parameters for simulation. For the cases that the quality of the water is unknown, however, it can be very laborious to find the appropriate values to meet reasonable results.

The diameter of the nuclei can be determined through $R_B = \sqrt[3]{\frac{3}{4\pi n_0} \frac{1 + \alpha_{\text{Nuc}} - \alpha_l}{\alpha_l}}$. In the Schnerr-Sauer phase change model the diameter of the vapour bubble is in the denominator of the model, thus the phase change rate is proportional to $\sqrt[3]{n_0}$. As a result, one way to compensate for the underprediction of the number of nuclei is using appropriate large enough coefficients in the phase change model. It should be noted that the presented definition of nuclei radius is a slightly different from the original definition of the model in a way that it takes into account the volume fraction of nuclei, α_{Nuc} , according to OpenFOAM notations.

As it is presented in Figure 5.5, applying the strain rate modification proposed in Chapter 4, clearly improves the accuracy of the results.

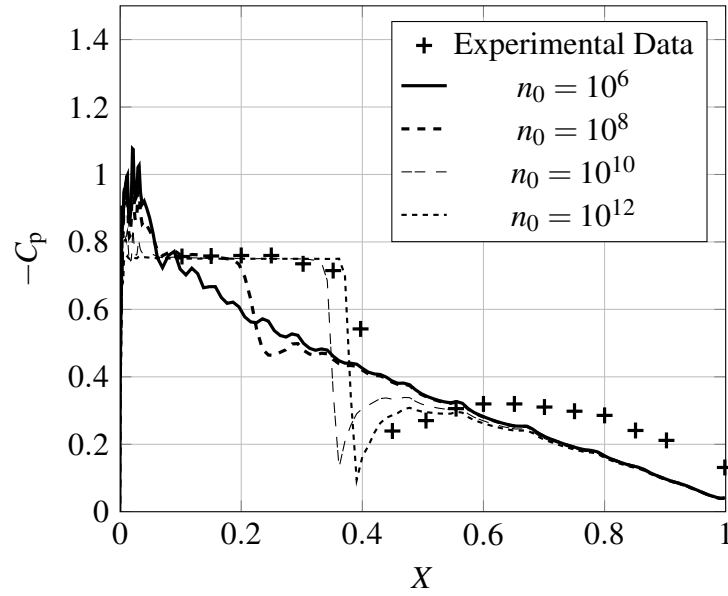


Figure 5.3: Pressure distribution of NACA0009 for different number of nuclei, $\sigma = 0.75, V_{in} = 15m/s$

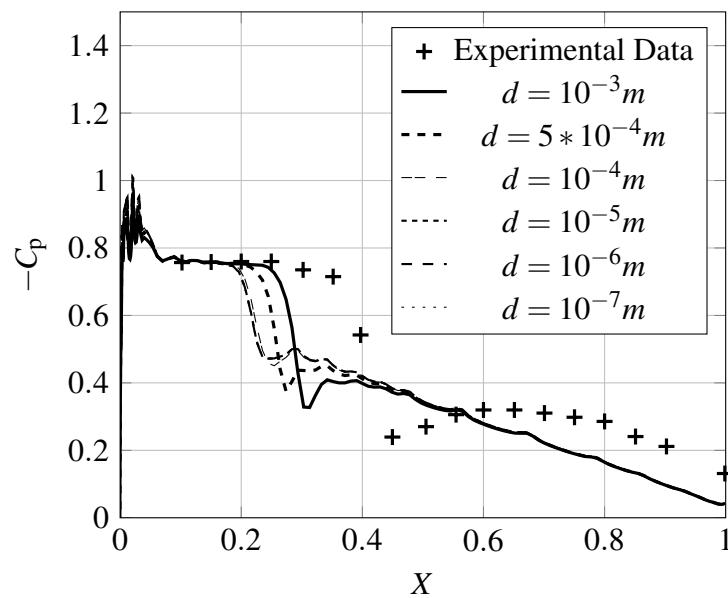


Figure 5.4: Pressure coefficient distribution over NACA0009 for different nuclei diameters, $\sigma = 0.75, V_{in} = 15m/s$

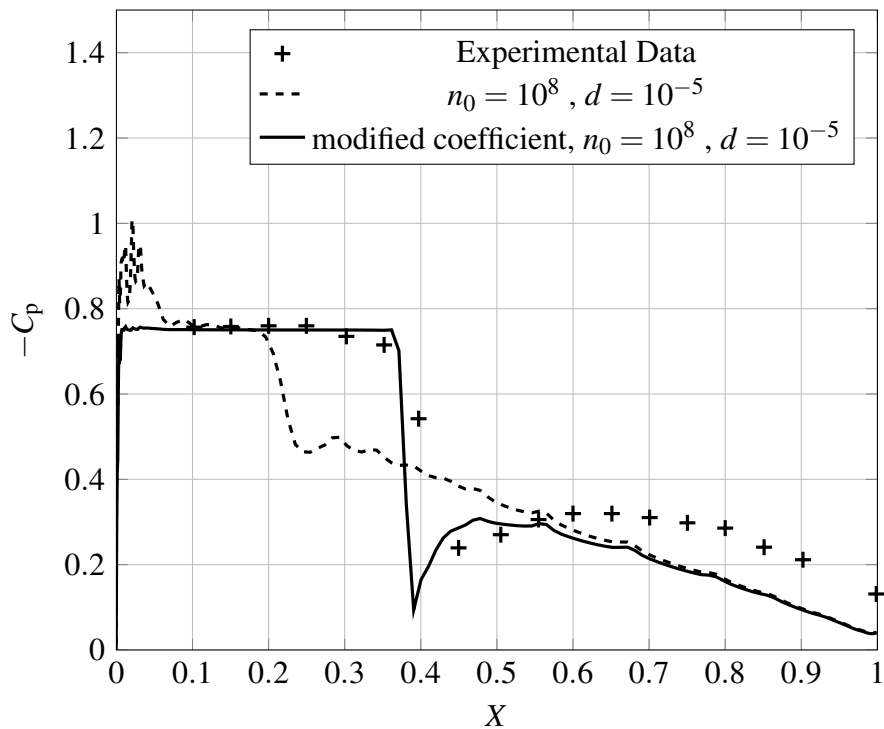


Figure 5.5: Pressure comparison between modified and original coefficients for the Schnerr-Sauer mass transfer model, $\sigma = 0.75, V_{in} = 15m/s$

5.2 NACA66MOD

In this section, numerical results of 2D sheet cavity simulation around the NACA 66 (MOD) foil are presented. The leading edge and mid-chord cavitation on a hydrofoil is of particular interest for propeller cavitation studies, as it represents the two-dimensional characteristics of propeller blade cavitation [59]. The study here is focus on the mesh resolution effects on the cavitation simulation and force distribution under three different operating conditions.

5.2.1 Experimental setup

The experiments were performed in the High Speed Water Tunnel in the Graduate Aeronautical Laboratories of the California Institute of Technology. The original geometry of the foil was modified for the experimental tests to meet the requirements of the tunnel test, so called NACA66MOD. The tested foil has camber ratio of 0.02, mean line of 0.8 m and thickness ratio of 0.09. During the experiment, different operating conditions are tested and flow characteristics such as pressure coefficients on 13 taps and cavity size are measured, for further information see [60].

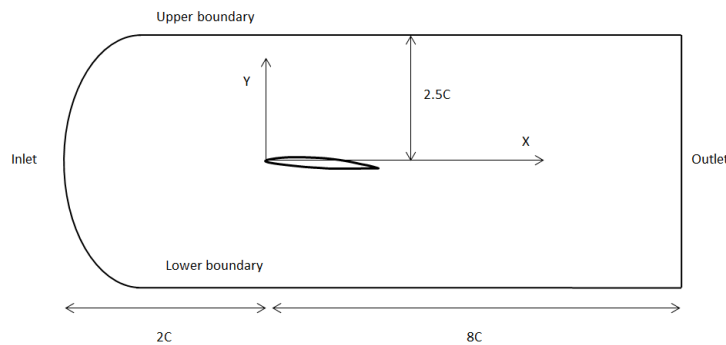
Table 5.3: Boundary conditions for cavitation simulation of NACA66MOD

boundary	velocity	pressure	nuSgs	alpha
Inlet	fixed value	zeroGradient	zeroGradient	fixed value
outlet	zeroGradient	fixed value	zeroGradient	zeroGradient
Foil	no slip	zeroGradient	Wall function	zeroGradient
Upper	slip	zeroGradient	zeroGradient	zeroGradient
Lower	slip	zeroGradient	zeroGradient	zeroGradient

5.2.2 Numerical setup

Based on the experimental observations, a 2D computational domain is employed for numerical simulation of cavitation around NACA66MOD foil. In the used configuration, the inlet is located $2C$ upstream of the foil, outlet is located $8C$ downstream of the foil, and the tunnel width is set equal to $5C$, where C is the chord length of the foil, Figure 5.6. The boundary conditions and simulation settings for this case are presented in Table 5.3. Numerical simulations are carried out for three different cavitation numbers where the angle of attack, 4 degree, and the flow Reynolds number, 2×10^6 , are kept constant. The Reynolds number is calculated based on the chord length and inlet velocity.

The computational domain consists of 21000 hexahedral cells which are clustered towards the leading edge, where the pressure gradients are stronger and therefore finer resolution is necessary to capture the flow physics. The cells are also clustered near the foil to provide averaged normal to surface resolution (y^+) equal to 5.

**Figure 5.6:** cavitation simulation setting of NACA66MOD

Three different cavitation numbers have been tested, 0.84, 0.91 and 1.0. The outlet pressure is adjusted to meet these cavitation numbers while the inlet velocity has been kept constant in the simulations.

5.2.3 Cavitation simulation

In Figure 5.7, the pressure coefficient distributions for different cavitation numbers are presented over the foil in the streamwise direction which is normalized by the chord length. Comparing the numerical results with experimental data at the leading edge region indicates that the cavitation has been predicted reasonably well. The main difference between the numerical results and experimental data is at the end of cavity. There, due to the higher pressure values, the condensation is stronger and cavitation simulation would be affected mainly by the accuracy of condensation prediction. At the cavitation number $\sigma = 1.0$, the pressure coefficient curve is sharp at the end of the cavity showing clear stagnation point while in the lower cavitation number, e.g. $\sigma = 0.84$, the variation of the pressure is smoother.

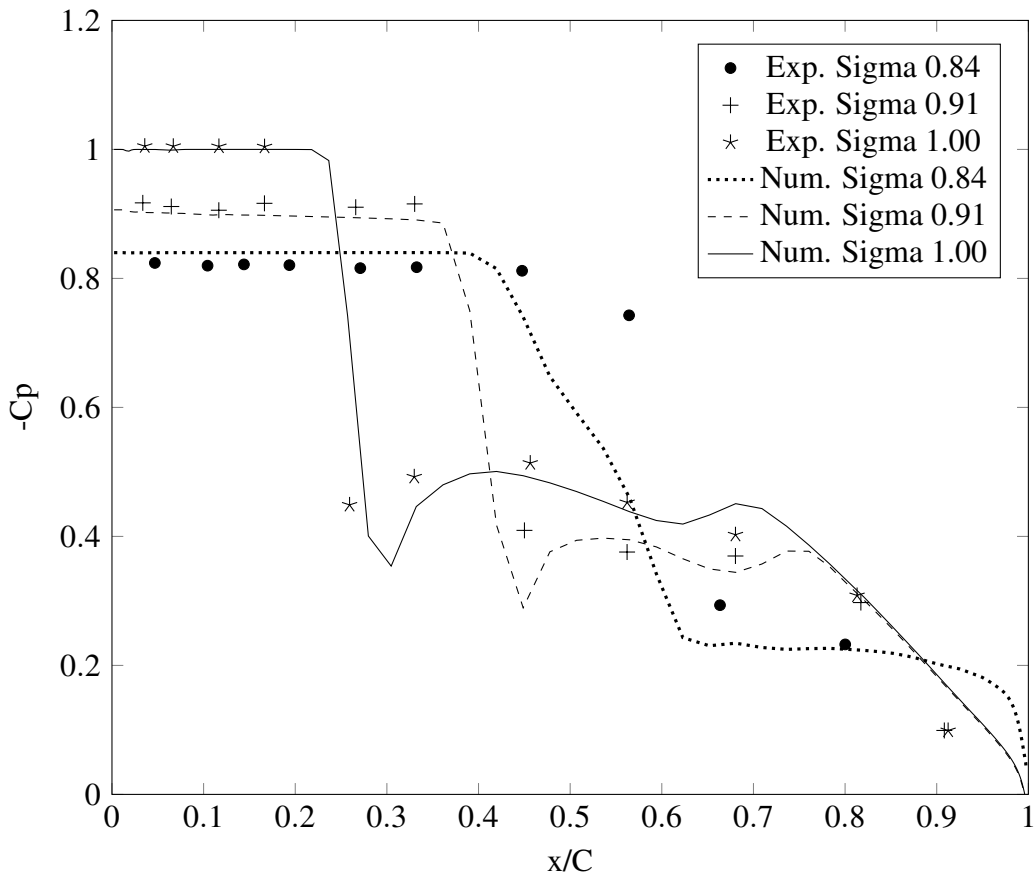


Figure 5.7: Pressure coefficient of NACA66MOD for different cavitation numbers

At $\sigma = 1.0$, the numerical simulation is able to predict the cavitation size and stagnation point very well. At $\sigma = 0.84$, the numerical simulation is able to predict the trend well but the discrepancy between the numerical results and experimental data at the end of the cavity is noticeable. In Figure 5.8, the averaged liquid

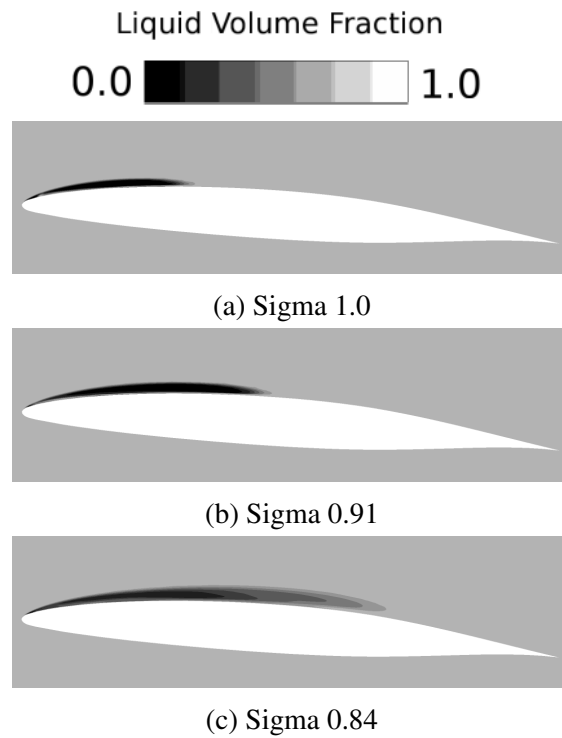


Figure 5.8: Averaged cavity distribution around NACA66MOD for different cavitation numbers

volume fraction for different cavitation numbers are presented.

As it can be observed from Figure 5.7, the discrepancy between numerical results and experimental data at the closure region ($0.4 < x/C < 0.8$) is higher for $\sigma = 0.84$. Assuming that the transportation of vapour from the leading edge to the closure region is done reasonably acceptable, the pressure distribution at this region is highly dependent on the accuracy of vapour to liquid phase change simulation. Condensation phase change model, compressibility effects, and also numerical settings such as mesh resolution and alpha transportation scheme are some of the parameters that can affect the accuracy of condensation prediction. One possible candidate for the discrepancy between the numerical results and the experimental data is the spatial mesh resolution. As it is stated previously, the mesh has been clustered towards the leading edge and also trailing edge in order to capture the high flow gradients at those region. Therefore, the spatial resolution is coarser at the middle region of the foil. By decreasing the cavitation number, the cavity size will increase and gets closer to the middle of the foil which as described has coarser mesh resolution, e.g. in $\sigma = 0.84$ the closure region is around $0.4 < x/C < 0.6$. In order to investigate the effects of the mesh resolution, the mesh has been refined in the streamwise direction in two steps. At first step the cells inside $0.25 < x/C < 0.9$, and then at the second step the cells inside $0.375 < x/C < 0.8$ are refined. So the cells inside the second box would be four times smaller than the initial cells at that location, Figure 5.9. The final mesh

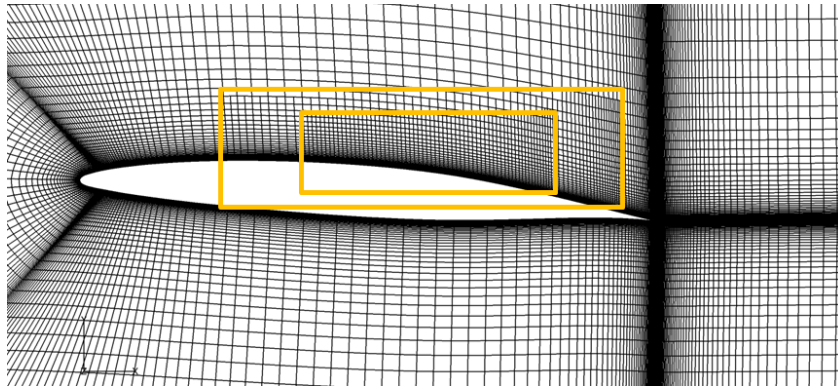


Figure 5.9: Local mesh refinement at the cavity closure region, NACA66MOD

resolution has around 23 000 cells which is around 10% higher than the initial cell size.

Once the cavity develops and vapour covers the surface of the foil, the local Reynolds number decreases due to the reduction of the local density. This will lead to increase of the non-dimensional normal distance from the wall (y^+). While using the wall model, it is important to keep the first cell y^+ in the log-law region. For $\sigma = 0.84$, the y^+ based on the wet flow simulation is around 5 while in the cavitating flow and based on the averaged fields, the y^+ is around 17. This indicates that the spatial resolution in the normal direction of the wall is enough, and there is no need for further refinement at the normal direction.

In Figure 5.10, the numerical results of different spatial resolutions are compared with the experimental data for $\sigma = 0.84$. As it can be seen from the results, the refinement of the spatial resolution at the closure region has increased the accuracy of prediction of pressure distribution specially at $0.5 < x/C < 0.6$.

For sheet or semi-steady cavities, it is possible to refine the spatial resolution based on the primary results to get more accurate results later without increasing the computational cost considerably. However, for shedding cavity or vortex cavitation where usually the flow is also three dimensional, providing appropriate spatial resolution to reasonably model the condensation is not straight forward.

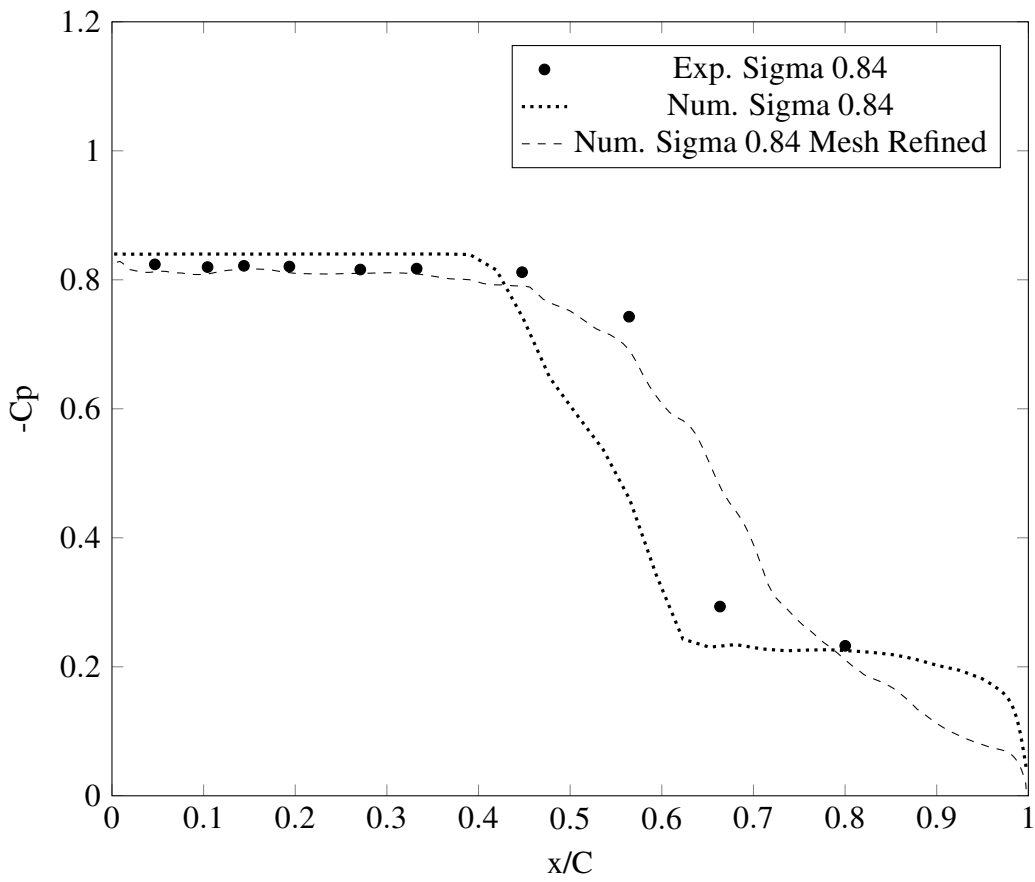


Figure 5.10: Effects of the mesh resolution at the closure region, NACA66MOD
Effects of the mesh resolution at the closure region of the cavity on the pressure distribution and cavity size, NACA66MOD, $\sigma = 0.84$

5.3 Twisted Delft hydrofoil

Twisted foils are considered and tested to improve the knowledge regarding the three dimensional effects on the cavitation and its characteristics such as interactions of the cavity with re-entrant jets, cavitation collapse, noise, vibration and erosion risk. These foils generate cavitation which resembles propeller cavitation but in a more well defined and easily studied set up which makes it an attractive test case for evaluation of computational approaches for predicting cavitation. Therefore, in this section numerical study of cavitating flows around the Delft Twist11 hydrofoil is presented. The 3D Delft Twist11 hydrofoil spans the cavitation test tunnel from wall-to-wall and is symmetric with respect to its mid-span plane. The foil has a spanwise varying geometric angle of attack (twist) from zero degree at the tunnel wall to 11 degree at its mid-section. This avoids the interaction of the cavitation sheet with the boundary layer along the tunnel wall [11, 61, 62].

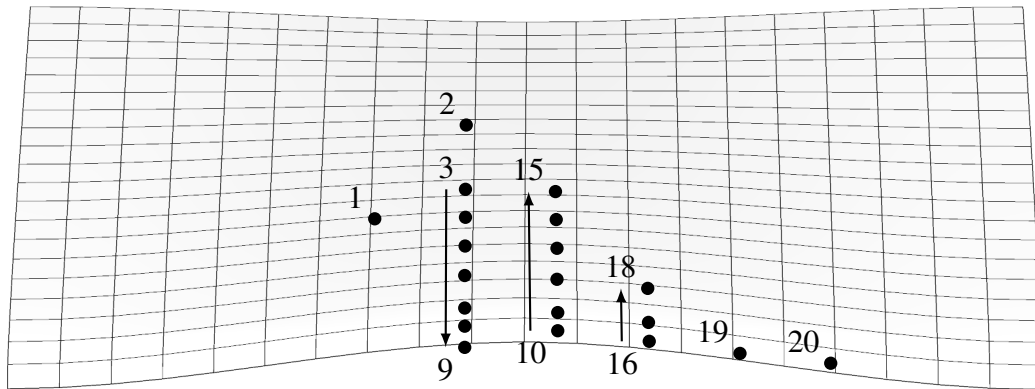


Figure 5.11: Pressure probes locations and numbers on the Twist11 foil, [61]

5.3.1 Experimental setup

The experimental tests are carried out for the 3D Twist11 hydrofoil in steady and unsteady inflow conditions in the cavitation tunnel at Delft University. The main interest was to generate three dimensional sheet cavities that in character are similar to ones that occur on ship propellers. Due to the spanwise variation of the angle of attack, the sheet cavity is three-dimensional and the closure line of the cavity is convex-shaped. In order to eliminate the possible effects of laminar boundary layer on the cavitation, sand grains are applied to the leading edge of the foil to provide appropriate roughness to intrigue the flow into the fully turbulent flow. Pressure distribution, lift and drag forces, velocity profile, and cavitation pattern are observed and measured during the experiment. For further information, see [61].

It should be noted also that the Twist11 foil experimental tests were conducted in two different cavitation tunnels, Delft and EPFL institutes cavitation tunnels where the foil used in EPFL had scale factor 0.5 comparing to the one used in Delft [61]. However, since the flow Reynolds number is around 1×10^6 , and the flow is fully turbulent over the foil due to the leading edge roughness, it is possible to use both experimental data for validation of the related numerical simulations. In the current study the foil related to the Delft experimental tests is considered for numerical modelling, however, the numerical results are also compared with the EPFL results.

In order to measure the pressure distribution over the foil, several pressure probes were installed on the foil to measure the pressure distribution, Figure 5.11. The numbering of the probes in this figure is kept the same as the reference. In the experimental report further information about these probes, their locations, and their related uncertainty is provided [61, 62].

5.3.2 Geometry and mesh structure

The geometry of the hydrofoil consists of a NACA0009 profile, with chord length, C , equal to 150mm, that has a spanwise varying angle of attack, ranging from zero

degree at the cavitation tunnel wall to 11 degree at the center line and then back to zero degree symmetrically with respect to the center plane, with a total span of two chord length [62]. For the current study, simulation of the foil having -2 degree angle of attack is conducted. Taking advantage of the symmetry only half of the domain is considered for numerical simulation. The computational domain for the most of the cases extends $6.5C$ in the streamwise direction, starting $3C$ upstream of the leading edge and ending $2.5C$ behind the trailing edge. In one case in order to investigate the effects of the outlet boundary location on the numerical simulation, the outlet boundary is moved $9C$ downstream of the foil. In the vertical direction, the domain extends $2C$, with the hydrofoil mounted in the center. Structured surface mesh is used on the foil surface, along with the extrusion method to create appropriate boundary layer mesh around the foil. Number of layers is selected large enough to be able to use tetrahedral cells far from the foil. This will decrease the mesh concentration on the regions that are not disturbed by the foil and therefore less interesting physics are happening there to be captured, Figure 5.12.

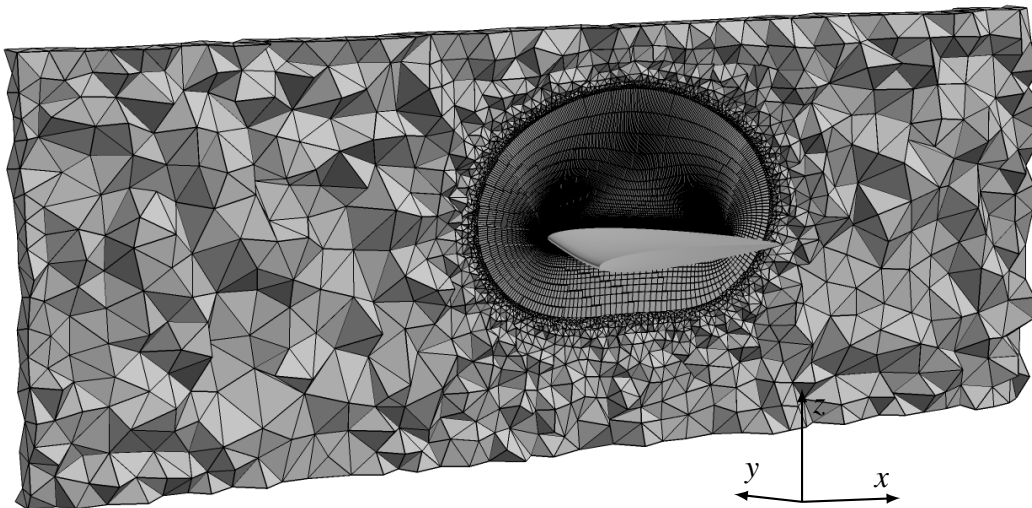


Figure 5.12: Computational domain of Twist11 simulation

5.3.3 Flow conditions

Standard inflow boundary condition is used as the inlet where the flow velocity is set equal to 6.97 m s^{-1} , giving $Re = 1.05 \times 10^6$. At the outflow boundary a fixed pressure of 2970 Pa is used, regarding the outlet cavitation number equal to 1.07 . At the upper, lower and side walls of the tunnel slip boundary condition is employed. Symmetry plane is used at the centre of the tunnel, and no-slip boundary condition is specified on the hydrofoil surface.

5.3.4 Computational mesh description

The mesh resolution study is categorized in two parts. The first part focuses on the mesh independency study based on the wetted flow analysis and the second part focuses on the mesh resolution effects on the cavitation simulation.

In the wetted flow mesh independency study, at first the effects of the streamwise and spanwise resolutions (called surface mesh resolution in this work) on the flow prediction are investigated while keeping the wall normal resolution constant ($y^+ = 50$). In Table 5.4, name, size and specifications of the mesh resolutions used for surface mesh independency study of the first part are presented. Four different surface mesh resolutions are considered with constant $y^+ = 50$. In this table, n_{suction} is the number of cells on the suction side of the foil in the streamwise direction, n_{spanwise} is the number of cells in the span direction, n_{layer} is number of boundary layers cells, respectively. It should be noted that since the gradient of the pressure and velocity at the leading edge are much higher than in other regions of the foil, the mesh points are clustered towards the leading edge. Moreover, the number of cells on the pressure side in the streamwise direction is kept constant, 70, in all of the meshes. The numbers $n_{\text{structured}}$ and n_{total} represent the number of structured and total volumetric cells.

Table 5.4: Surface mesh specification for mesh independency study, $y^+ = 50$

Mesh	n_{suction}	n_{spanwise}	n_{layer}	$n_{\text{structured}}$	n_{total}
T11-I	70	70	34	367k	658k
T11-II	140	70	34	478k	818k
T11-III	280	70	80	1932k	2461k
T11-IV	560	140	80	7005k	8733k

In order to investigate the effects of the first mesh height and its interactions with the selected wall model, five different y^+ have been selected and tested in the wetted flow mesh independency study, presented in Table 5.5. For these resolutions, the surface mesh resolution is the same as mesh T11-III in Table 5.4.

Table 5.5: Mesh specification for mesh independency study with different y^+

Mesh	T11-V	T11-III	T11-VI	T11-VII	T11-VIII
y^+	100	50	30	5	1

In the second part, the mesh resolution obtained from the first part is considered and effects of the mesh resolution on the cavitation prediction is investigated. Four different mesh resolutions are considered. The resolution in streamwise, spanwise and normal to the wall is varied while keeping $y^+ = 1$. The specifications of these mesh resolutions are presented in Table 5.6. It should be noted that the Mesh T11-A has the same resolution as mesh T11-VIII. It can be seen from the table

that mesh T11-B has four times finer surface mesh resolution comparing to mesh T11-A while the normal mesh distribution has been kept the same. Mesh T11-C and T11-D have the same surface mesh as Mesh T11-A and Mesh T11-B respectively, but with finer mesh resolution in the normal to the wall direction. Here, normal to the wall resolution does not imply just on the first cell height. For all of the cases in this section, the y^+ value is kept lower than one. Then, by varying the extrusion coefficient, different resolutions in the normal direction are created. It should be noted that the number of cells on the pressure side in the streamwise direction is kept constant, 70, for all of the meshes.

Table 5.6: Mesh specification for cavitation simulation, $y^+ = 1$

Mesh	n_{suction}	n_{spanwise}	n_{layer}	$n_{\text{structured}}$	n_{total}
T11-A	280	70	80	1932k	2461k
T11-B	560	140	80	5954k	7641k
T11-C	280	70	200	4830k	5374k
T11-D	560	140	200	17514k	19277k

5.3.5 Wetted flow simulation

5.3.5.1 Surface mesh resolution effects

In Table 5.7, the lift coefficients of non-cavitating simulations are presented and compared with the experimental data. It can be seen that by increasing the surface mesh resolution, the lift coefficient approaches 0.423. This comparison indicates that results of the mesh T11-III is independent of the surface mesh resolution and can be considered as an appropriate surface mesh resolution for further study. The presented experimental data for the lift coefficient has been interpolated from the reference based on the flow Reynolds number, [61].

Table 5.7: Lift coefficients for various mesh resolutions, wetted flow Twist11, $U_{in} = 6.97 \text{ m s}^{-1}$, $y^+ = 50$

Mesh	C_l	Error %
T11-I	0.433	-5.0
T11-II	0.413	-9.4
T11-III	0.423	-7.2
T11-IV	0.423	-7.2
Exp. [61]	0.456	-

5.3.5.2 y^+ effects

The selected y^+ values ranging from 1 to 100 covers different sections of the turbulent boundary layer, and since it also affects the wall normal spatial resolution outside the boundary layer, it will contribute to the vortex capturing accuracy. For all values, similar wall model has been used except for y^+ equal to one where no wall modelling is required. The surface mesh of the foil is the same as the mesh T11-III for all of the considered y^+ . In Table 5.8, the lift coefficients of the non-cavitating simulations are presented. As it can be seen, by reducing the height of the first cell, the accuracy of prediction of the lift coefficient is increased. The mesh with y^+ equal to one is selected as the selected normal resolution to test the proposed models for cavitation simulation, mesh T11-VIII.

Table 5.8: Lift Coefficient for different y^+ , wetted flow Twist11

Mesh	y^+	C_l	Error %
T11-V	100	0.426	-5.9
T11-III	50	0.423	-7.2
T11-VI	30	0.449	-1.5
T11-VII	5	0.441	-3.3
T11-VIII	1	0.454	-0.4
Exp.[61]	-	0.456	-

5.3.6 Evaluation of mass transfer modelling modifications

In this section numerical results of cavitating flow around the Twist11 foil are presented in order to evaluate the proposed mass transfer modelling modifications. Based on the wet flow mesh independency study performed in the previous section, the mesh T11-VIII having $y^+ = 1$ is selected. For this mesh resolution, cavitation is simulated in three different states. These three states are presented in Table 5.9 as model A, B, and C. Model A is based on the original settings of the Schnerr-Sauer model. In the model B, the phase change model coefficients are modified according to the proposed modification from turbulent time scale while the pressure threshold is keep constant equal to the saturation pressure. In model C, the threshold pressure is also modified to consider the shear stress in the liquid pocket rupturing and cavitation formation.

5.3.6.1 Verification of the proposed model for phase change rate

In Figure 5.13, the averaged vapour volume fraction and the averaged pressure distributions on the foil for the three different models (A, B, and C) are presented.

Table 5.9: Coefficients of the three different models investigated

Model	C_c	C_v	$p_{\text{threshold}}$
A	1.0	1.0	p_{Sat}
B	modified	modified	p_{Sat}
C	modified	modified	$p_{\text{Sat}} + p_a$

To present vapour volume fraction, two different values (50% and 10%) are used to create the iso-surfaces.

As it can be observed from the averaged pressure coefficient of model A, Figure 5.13b, the minimum pressure coefficient is lower than the minus cavitation number (-1.07) which indicates that the pressure is negative at those regions. This indicates that the cavitation (i.e. vapour liquid phase change rate) has not been modelled correctly. Moreover, based on the vapour iso-surfaces, Figures 5.13a the content and volume of vapour in Model A is under predicted significantly. Two parameters can cause such an under prediction. The first one is the number of excited nuclei and the other is the rate of the mass transfer. Since these two parameters have similar contributions according to the Sauer mass transfer model, here we have put the focus on the mass transfer rate.

To adjust the value of the mass transfer rate, one approach is to manually increase the C_v coefficient in order to increase the cavitation production, until a point that the negative pressure disappears. The reason that in different literature different values for C_v and C_c are used are related to this fact that depending mainly on the flow, mesh resolution, turbulence model and to some extent the discretization schemes; different values of C_v have to be used to prevent appearance of negative pressure in the cavitation results. It should be noted that it is a case in the fully turbulent cavitating flows, and in the laminar cavitating flows, experimental observations show the possibility of negative pressure before the reattachment point. The proposed modification for the coefficients will create a better relation between phase change rate and local flow properties. It can be observed from the obtained results, Figure 5.13, that using the modification leads to having positive pressure throughout the computational domain, and therefore more precise prediction of cavitation (e.g. size and shedding behaviour).

5.3.6.2 Investigation of shear stress effects on pressure threshold

In Figure 5.14, the added pressure to the pressure threshold based on the shear stress modification is presented, Model C. As expected, the results show that this modification is effective at the region where velocity strain is high, e.g. leading edge and cavity closure regions. For the studied case the maximum added pressure to the saturation pressure is around 1000 Pa. It should be highlighted that this modification will lead to increase in cavitation production at the leading edge as

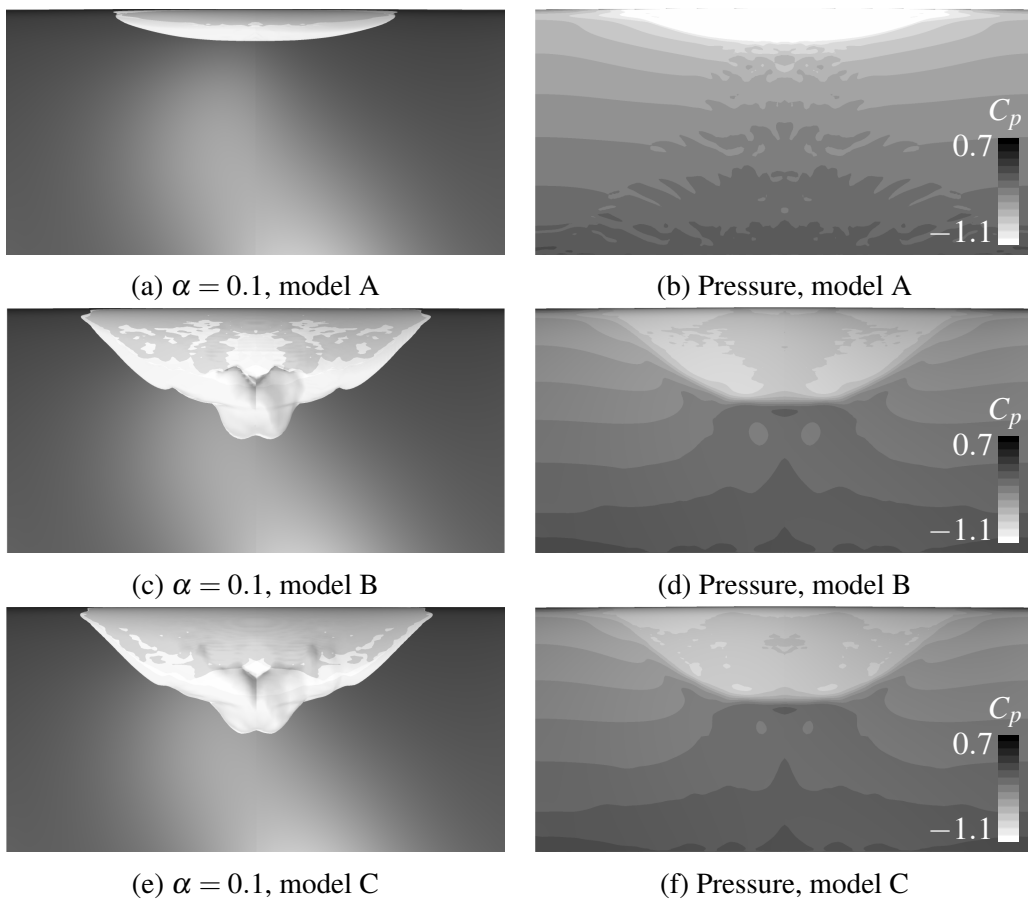


Figure 5.13: Averaged vapour iso-surfaces and pressure distribution around Twist11 with $y^+ = 1$.

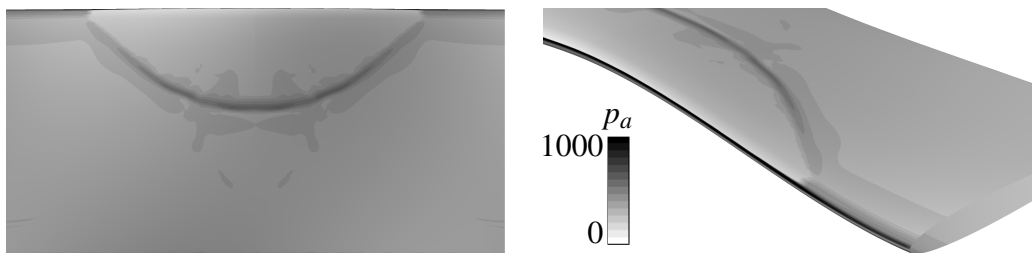


Figure 5.14: Added Pressure to the threshold pressure due to the viscous effects for cavitation around Twist11

well as to increase in condensation rate due to having higher threshold pressure at the downstream region and cavity closure region.

5.3.6.3 Pressure distribution

In Figure 5.15, the obtained numerical results for pressure distributions at different sections are compared with the experimental data. In this figure, the negative pressure coefficient is plotted versus distance from the leading edge which is normalized with the chord length, $C = 0.15m$. The results indicate that the proposed models can provide better prediction of the pressure over the foil comparing to the original model. Since the cavitation number is $\sigma = 1.07$, $-C_p$ values greater than 1.07 means having negative pressure. As it can be seen for Figure 5.15, the model A predicts negative pressure at the leading edge while the modified coefficients (models B and C) correctly predict positive pressure.

In the Delft experimental report, it is mentioned that due to the strong collapse near probe 7, the probe was damaged and the measured data was not realistic, and therefore its related measurements were removed from the report. Comparing the numerical results and Delft experimental data in $y/S = 0.5$ (middle plane of the foil) shows that the proposed modifications are in good agreement with the experimental data except for probe 6. Considering the flow cavitation number ($\sigma = 1.07$) and measured pressure value by this probe ($-C_p = 1.3$) it can be deduced that the average pressure at this location is much lower than zero which cannot be correct, since based on the experimental observation this region is mostly covered by vapour. The same uncertainty about the measured pressure by the probes 11, 12, 13, and 18 exists. The values measured by these probes show negative pressure in the region where the pressure is expected to be positive. The main interpretation is that during the measurement, the probes probably got hit by the collapse pressure pulse and damaged. Therefore, there are some uncertainty about the accuracy of the experimental data for these probes. The experimental data of EPFL is also plotted in Figure 5.15. As it can be observed from the figure, the numerical results have very good agreement with the experimental data measured at EPFL.

Comparing the pressure distribution predicted by model B and model C in the middle chord region of the foil ($0.4 < X < 0.6$), suggests that the model B has better prediction, and model C has over predicted the pressure at the end of the cavity region where most of the collapse occurs. However, it may not be the complete story since in this case the cavitation collapse structure consists of the rebound formation of the cavitation which is a compressibility dependent phenomenon. Another support for this claim is that in $y/S = 0.3$, the two models have similar prediction while by getting close to the $y/S = 0.5$ which is a region with stronger collapse the models predictions deviate from each other.

5.3.6.4 Lift coefficient

In Table 5.10 the numerical results for the lift coefficient is presented and compared with experimental data. The estimated error for lift prediction is between -10.8% to -13.4% . The lift force consists of lift induced by pressure force and by viscous force where the pressure force has the major role for the foils. As

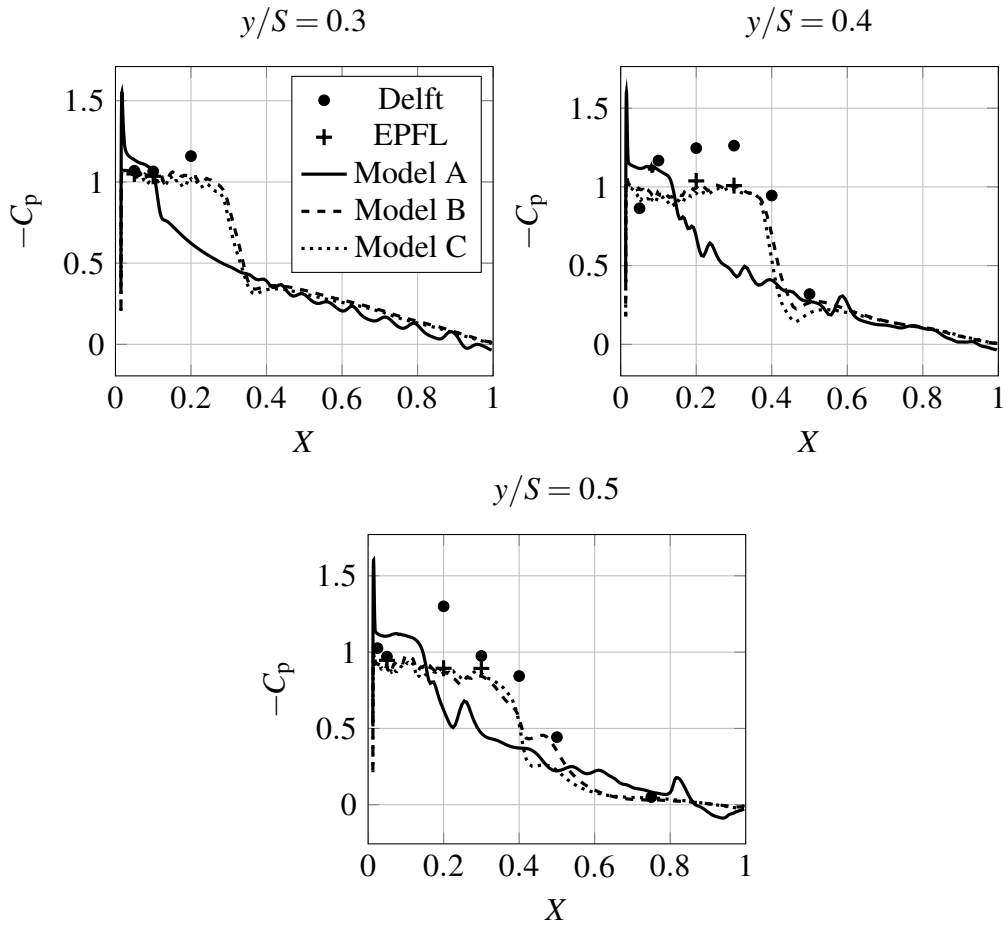


Figure 5.15: Comparison between numerical and experimental data for pressure variations at different sections of the Twist11 foil, experimental data derived from [61]

it is discussed in previous section, the model B and model C have much better agreement with the experimental data of pressure distribution than the model A. Therefore, it was expected that these two models could provide better lift force prediction. One possible explanation that this is not the case is that in model A, the pressure at the leading edge is negative which will help to have higher lift force. In model B and C, this negative pressure is replaced by pressure close to the threshold pressure due to the higher phase change rate. Due to the lack of enough spatial mesh resolution, the simulation is not able to follow and model the separated two-phase vortex. Therefore, the vortex cannot be transported appropriately to the downstream of the flow. As the strength of the vortex is underpredicted, the pressure inside the vortex is smeared and over predicted. This will lead to predicting lower lift force.

The lift coefficient variation over time, Figure 5.16, shows that at some conditions the lift coefficient becomes negative, lowest value around -0.15 . In Figure 5.17, the flow behaviour close to the time of getting negative lift force is presented. The time step between the pictures is 1×10^{-3} s, and the results are related to the model C. As it can be seen form Figure 5.17, the negative lift force is related to the time that the flow experience strong condensation and the separated cavity collapses very fast posing very strong pressure pulse to the foil. In Figure 5.18, fluctuations of the pressure are plotted for different probes. Probes closer to the collapse region (probes 2 and 3) experience very high pressure pulse, around 2 atm. Since the middle plane of the foil is affected by two separated cavity collapses, the magnitude of the pressure pulse is much larger near the middle of the foil ($y/S = 0.5$) than the neighboring section, $y/S = 0.4$. In reality this type of sudden collapse will be followed by regeneration of cavitation. This phenomenon is highly compressible and therefore, the incompressible modelling approach cannot capture it. This drawback of incompressible modelling of cavitation might be also a reason for discrepancy between numerical and experimental cavity behaviour and cavity size.

Table 5.10: Lift coefficients results of different cavitation models (T11-VIII)

Model	C_l	Error (%)
A	0.455	-10.8
B	0.447	-12.3
C	0.441	-13.4
Exp. [61]	0.51	-

5.3.7 Effects of the outlet boundary distance

In the presented numerical results, fixed value condition is used for the pressure outlet boundary. Depending on the distance between the outlet and the foil, using

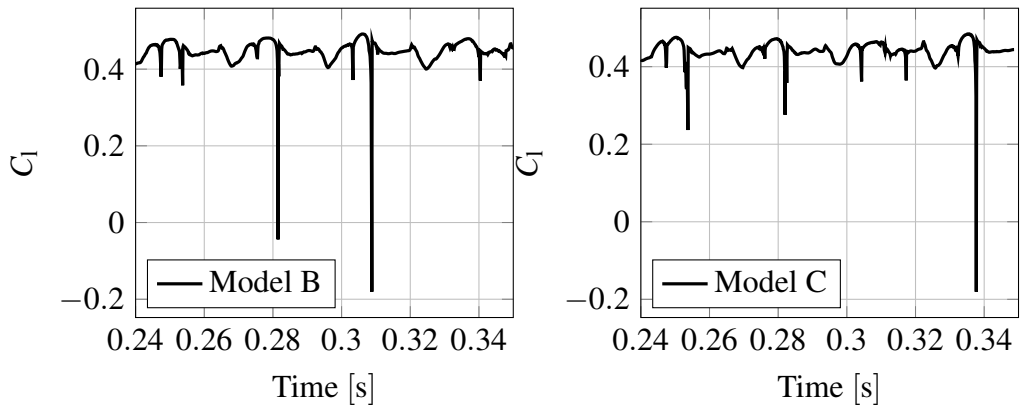


Figure 5.16: Variation of lift coefficients for model B and model C versus time

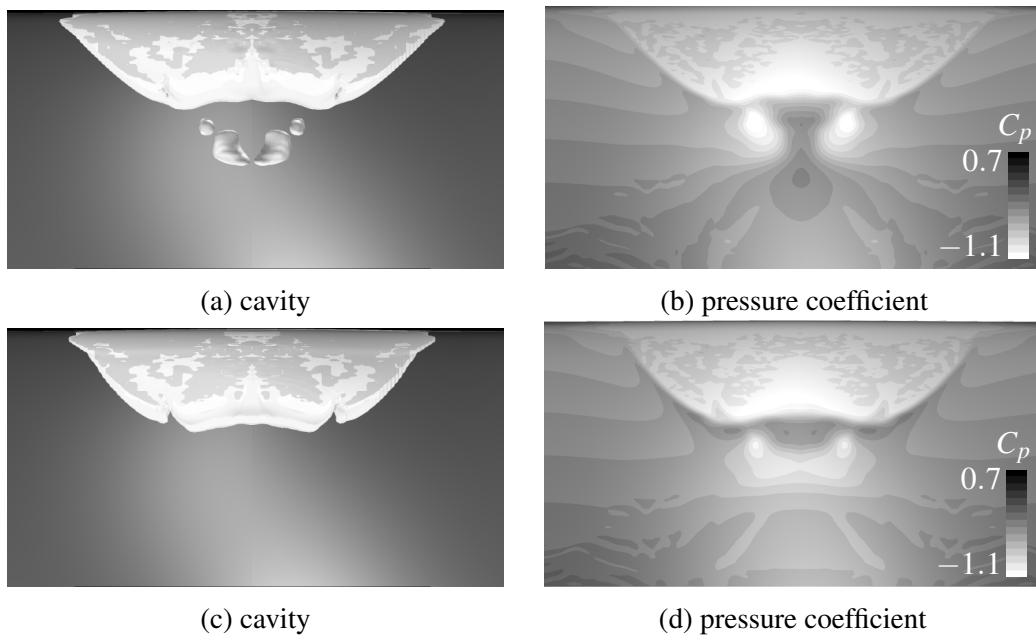


Figure 5.17: Cavity and pressure distribution before (a, and b) and after (c, and d) having negative lift force

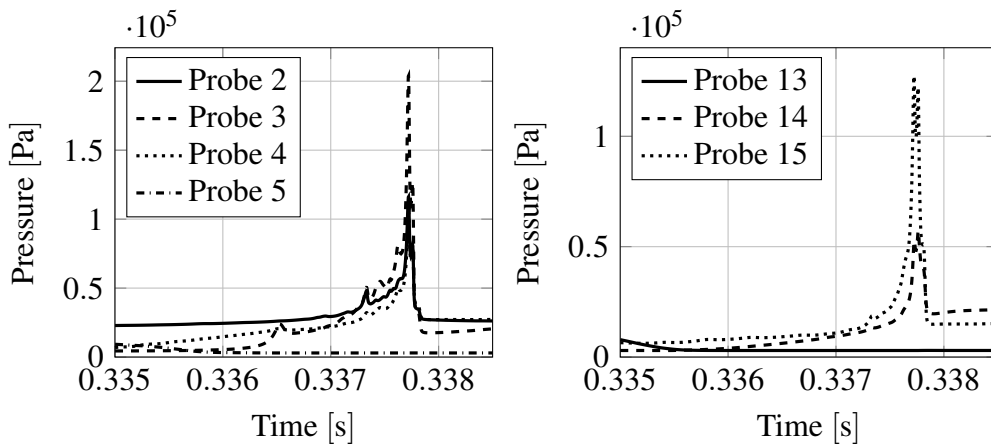


Figure 5.18: Pressure variations calculated at different probes location during experiencing negative lift force

constant value at the outlet plane may affect the pressure distribution and flow characteristics around the foil. In order to investigate this possible effect at the current simulation, for one case the outlet boundary condition is moved $9C$ downstream of the trailing edge. Other mesh properties are the same as the case used in the cavitation simulation sections (Mesh T11-VIII) with model C.

In Figure 5.19, the pressure coefficient distributions for different outlet distance are plotted versus experimental data at the two sections of the foil. At the section $y/S = 0.4$, the results for two cases are very similar and noticeable differences have not been observed. At section $y/S = 0.5$, however, the effects of the outlet boundary condition are more visible, especially near the middle of the foil. The offset between two pressure distribution curves indicates when the outlet boundary condition is further distanced from the foil, it will let the cavity to be transported slightly further downstream, especially at the central region of the foil ($y/S = 0.5$). Therefore, it could be expected that by having outlet boundary condition far enough from the foil, cavitation can be transported further downstream. The obtained results, however, show that cavitation behaviour (size, and shedding) for both cases are very similar. It is observed that the case with closer outlet ($2.5C$) has slightly higher concentration of the vapour near the closure area at the central part of the foil. The main reason for a such a behaviour could be predicted from Figure 5.20. Having outlet boundary close to the foil would put more constrain on the cavity closure area leading to more concentrated cavitation at the separated vortex.

5.3.8 Spatial mesh resolution effects on cavitation simulation

In Section 5.3.5, the mesh independency study was carried out based on the wet flow analysis. Then, the cavitation simulation performed on that spatial mesh resolution which has been presented in Section 5.3.6. When cavitation occurs in a flow, due to the different vapour and liquid density values, the mass fluxes at the

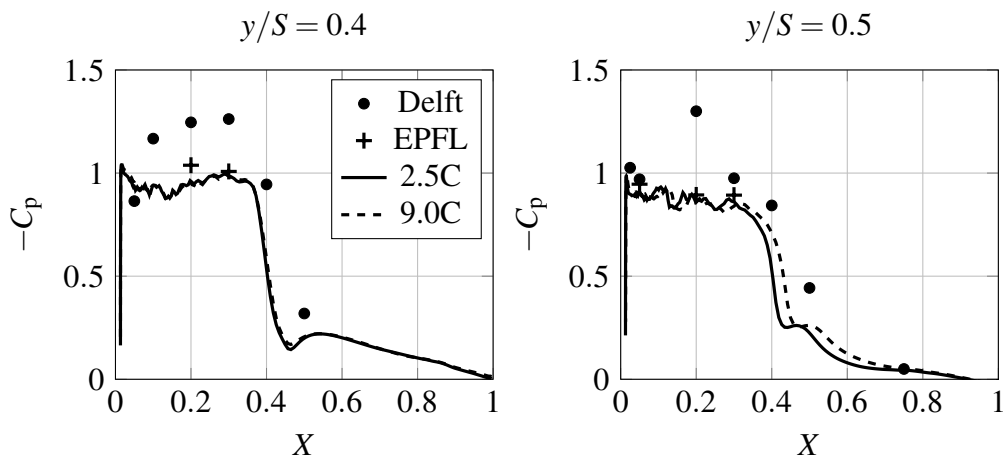
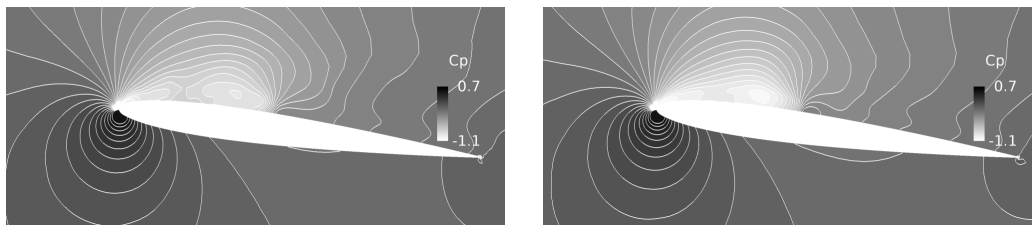


Figure 5.19: Pressure distributions for different outlet boundary distances over the Twist11, at different sections of the foil



(a) Outlet at $9C$ from the trailing edge

(b) Outlet at $2.5C$ from the trailing edge

Figure 5.20: Pressure coefficient distributions at the section of $y/S = 0.5$ for different outlet boundary distances

interface of the cavity will become different. This can also be deduced from the non-zero divergence of the velocity in the cavitating flows that at the interface of the cavity due to having phase change and varying density over time, the summation of mass fluxes on the faces of the computational cells are not zero. Therefore, capturing the cavity interface, and cavity behaviour, will be dependent on the spatial resolution especially where the cavity interface exists. In the current section, the effects of the spatial resolution in the streamwise, spanwise and normal to the wall directions, on the cavitation are studied. Here, normal to the wall resolution does not imply just on the first cell height. For all of the cases in this section, the y^+ value is kept lower than one. Then, by varying the extrusion coefficient, different resolutions in the normal direction are created.

5.3.8.1 Non cavitating conditions

Comparison of the numerical results for the wet flow simulation with the experimental data is presented in this section. In Figure 5.21, the pressure coefficient distributions, and in Table 5.11, the lift and drag coefficients are presented for

different mesh resolutions. As it is expected for the wet flow simulations, the comparison shows good agreement between the numerical results and the experimental data.

Table 5.11: Lift and drag coefficients for various mesh resolutions, wetted flow simulation

Mesh	C_l	Error %	C_D
T11-A	0.454	-0.4	0.014
T11-B	0.453	-0.44	0.013
T11-C	0.465	+1.9	0.013
T11-D	0.453	-0.44	0.012
Exp. [61]	0.456	-	-

5.3.8.2 Pressure Distribution

In Figure 5.22, the predicted average pressure at two different sections of the foil is compared with the experimental data. Both the experimental data measured at EPFL and Delft laboratories are considered for the comparison.

The numerical results for all of the spatial resolutions have similar level of accuracy in the region near to the leading edge, $X < 0.4$. However, mesh T11-B and mesh T11-D which have the same surface resolution, show better prediction in the region close to $X = 0.2$. The results also show that increasing the spatial resolution in the normal to wall direction will increase the accuracy of predicting the pressure distribution, especially at the region $0.4 < X < 0.6$. Although mesh T11-C shows better prediction of the pressure at $0.4 < X < 0.6$, it overpredicts the pressure at the trailing edge region.

5.3.8.3 Lift Coefficient

The comparison between the averaged numerical results and experimental data of the lift coefficient is presented in Table 5.12. As it can be seen from this table, although all of the selected resolutions were able to predict the lift coefficient very well in the wet flow simulations, the error level in the cavitating simulations is around 11%. There are several factors affecting the lift force prediction in the cavitating flows around the foil.

The lift force consists mainly of the pressure force. It is the pressure value that also defines the cavity content and size. Pressure, velocity and volume fraction are linked to each other through the non-linear governing equations. Considering the pressure distribution, presented and discussed in section 5.3.8.2, it may be deduced that over prediction of the pressure at the down stream region of the

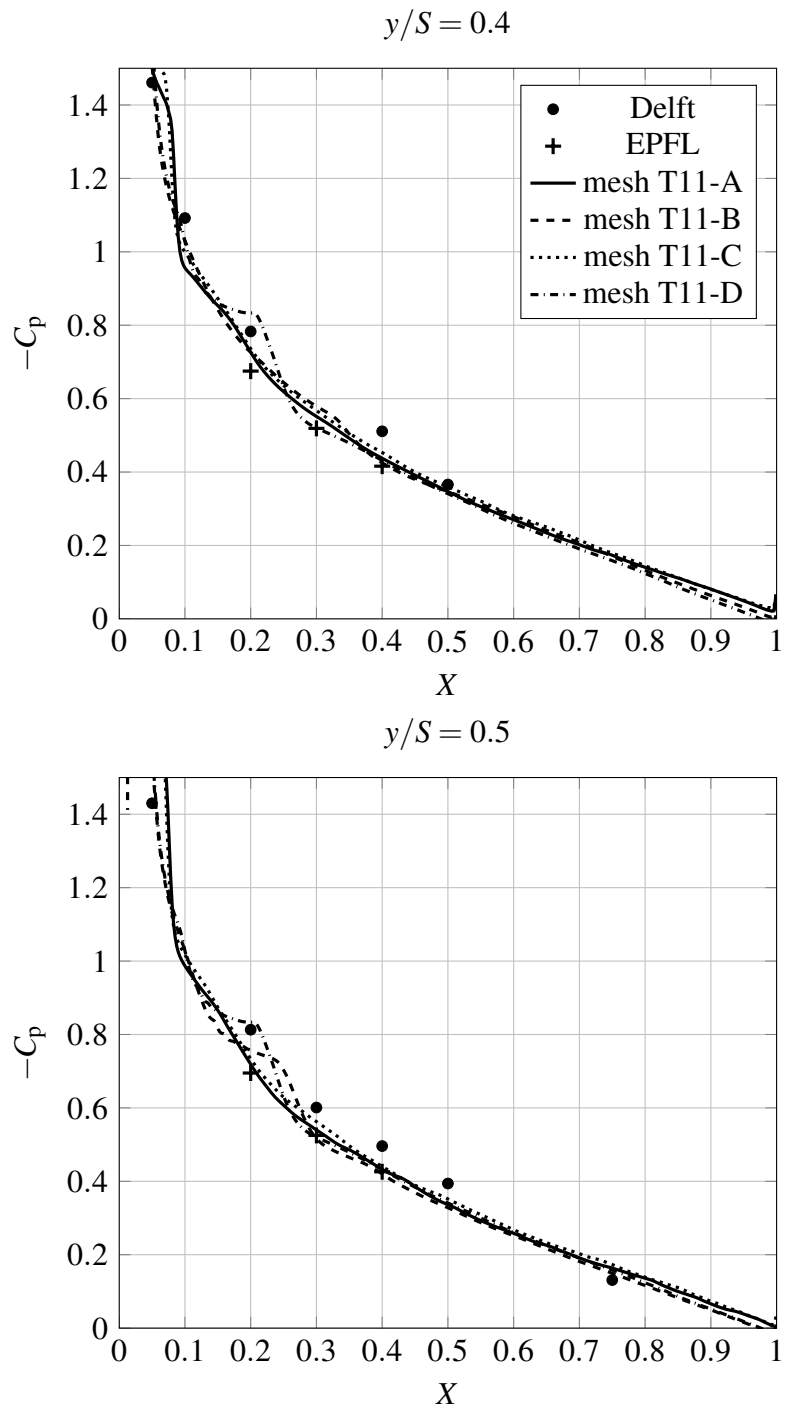


Figure 5.21: Pressure coefficient distributions over Twist11 for different mesh resolutions, at different sections of the foil in the wetted flow condition

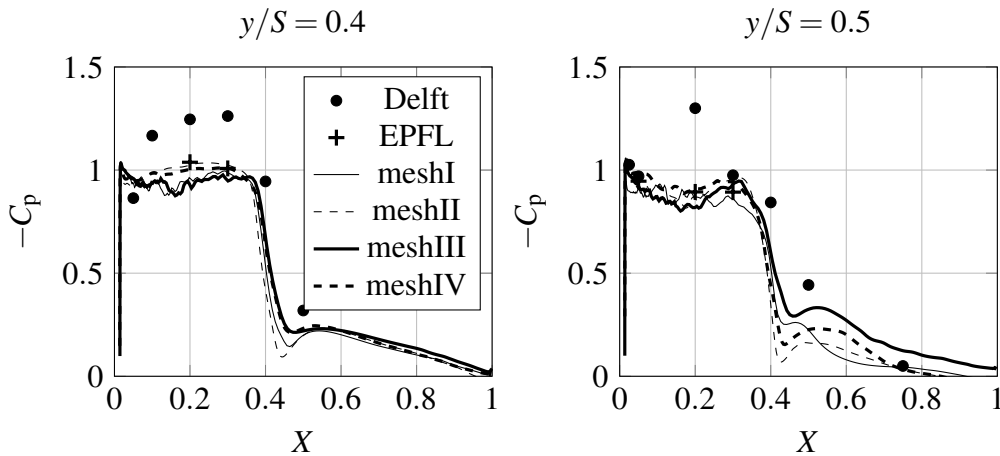


Figure 5.22: Pressure coefficient distributions over Twist11 for different mesh resolutions, at different sections of the foil

cavity, $0.4 < X < 0.6$, can be a reason for under prediction of lift force. From Figure 5.22, it can be seen that mesh T11-C has better prediction of pressure at the mid-chord region of the foil, $0.4 < X < 0.6$. As a result, this case has better lift prediction comparing to other spatial mesh resolutions, Table 5.12. The main reason for over prediction of the pressure at that region is related to the lack of sufficient spatial resolution to follow the separated vortex.

In Figure 5.23, variation of the lift coefficient in one typical shedding cycle is presented for each mesh resolution. There is one significant difference between the lift coefficients predicted by different meshes. Mesh T11-A and mesh T11-C which have the same surface mesh resolution predicts strong force acting on the foil during the cavity collapse at the down stream. This strong force, which is due to a strong pressure pulse, has caused the negative lift at the collapse time while the two other mesh resolutions show positive lift prediction throughout the shedding cycle.

Table 5.12: Lift coefficient for various mesh resolutions in cavitating flow simulation

Mesh	C_l	Error %
T11-A	0.441	-13.5
T11-B	0.444	-12.8
T11-C	0.454	-10.9
T11-D	0.449	-11.9
Exp. [61]	0.51	-

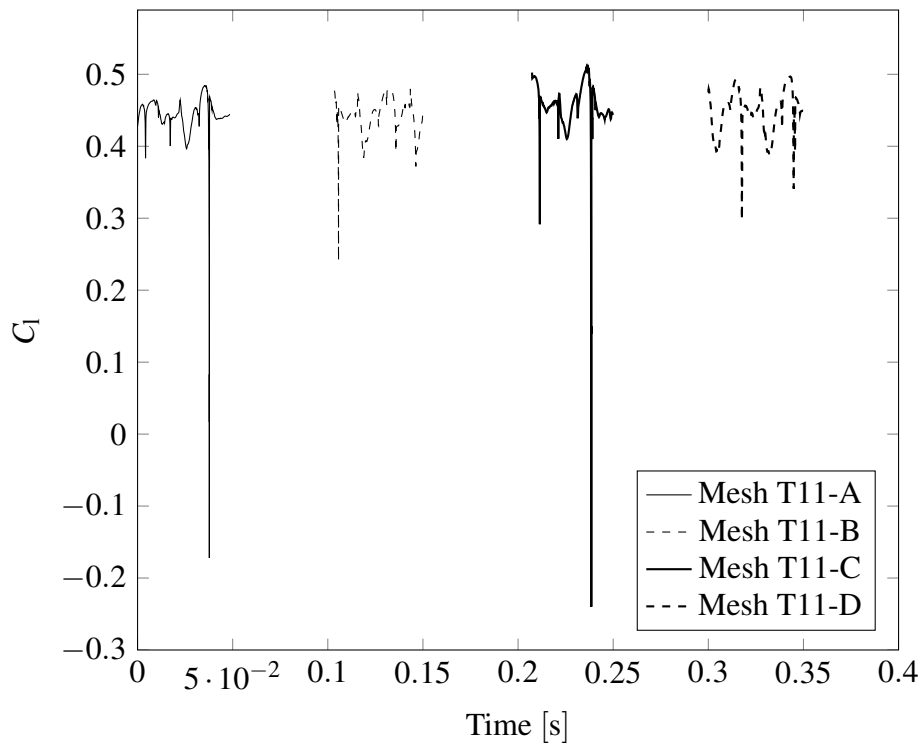


Figure 5.23: Variation of lift coefficient for various mesh resolutions, cavitating flow

5.3.8.4 Cavitation shedding behaviour

Integrating the vapour volume fraction over time, Figure 5.24, shows that the cavity size is directly dependent on the mesh resolution. The finest mesh resolution, mesh T11-D, shows around three times bigger cavity size than the other resolutions. To some extent, this behaviour was predictable since the cavity amount is directly proportional to the pressure distribution which for vortex based flow is dependent on the spatial resolution. Based on the vapour volume fraction variations over time, the frequency of the shedding is calculated and presented in Table 5.13. It is noticeable from this table that increasing the resolution and therefore better prediction of the cavity amount will increase the accuracy of the cavitation transportation, i.e. frequency of the flow.

5.3.8.5 Cavitation pattern

In Figure 5.25, the vapour iso surface 10 % is presented for different resolutions. The main difference is near the middle of the foil where the cavitation and the separated vortex have stronger coupling and interaction. Since the finer mesh can predict the vortex strength better than the others, the cavitation content near the middle plan is bigger for the finer mesh.

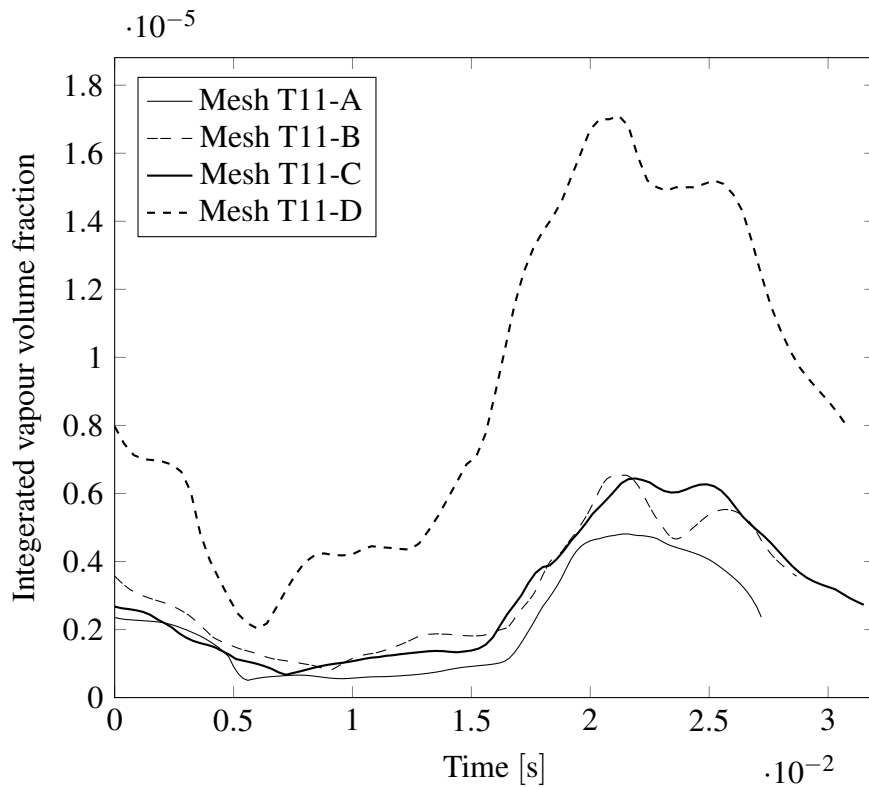


Figure 5.24: Integrated vapour volume fraction for different mesh resolutions in one typical shedding cycle

Table 5.13: Comparison of the shedding frequency of the cavitating flows

Mesh	$f_{FO}Hz$	Error %
I	36.7	12.7
II	34.8	7
III	31.7	-2.6
IV	32.5	-0.1
Exp. [61]	32.55	-

In Figure 5.26, the numerical results of cavitation shedding behaviour are presented and compared with the experimental data in one typical shedding cycle. The pictures are related to the coarsest resolution, mesh T11-A, and the finest resolution, mesh T11-D. It should be noted that since the frequency of the flow predicted in the mesh T11-A is higher than the experimental data, the time difference between each step is adjusted to find the relative cavity pictures. As it can be seen from the Figure 5.26, the coarse mesh fails in predicting and transporting the separated two-phase vortex, e.g. Figure 5.26a, while the finer mesh can preserve the vortex until the trailing edge of the foil.

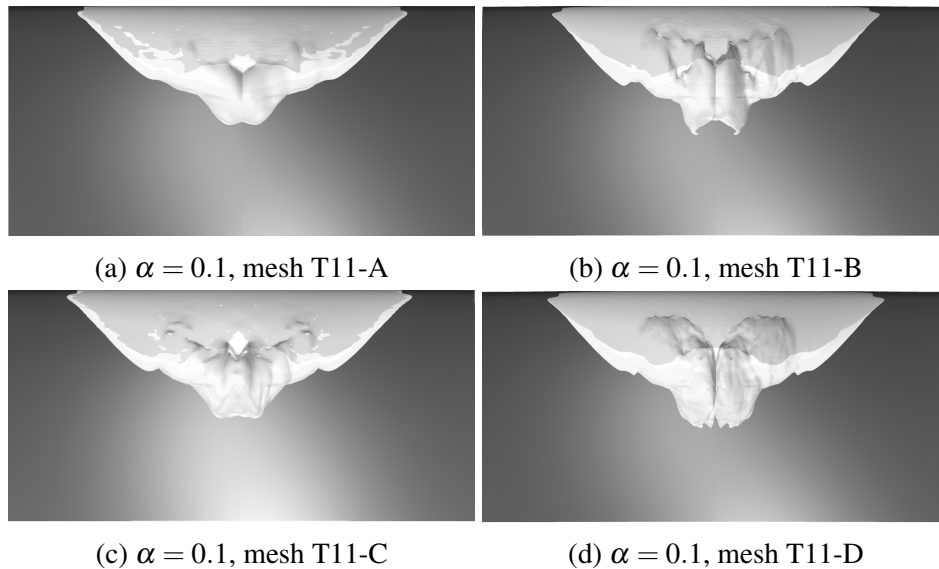


Figure 5.25: Averaged vapour iso-surfaces 10% around Twist11 with $y^+ = 1$ for four different mesh resolutions.

For the finest resolution, the amount of the separated cavity is reasonably in good agreement with the experimental data. It indicates that the spatial resolution at the leading edge region ($X < 0.4$) is well enough to capture the 3D sheet cavity generation and separation, Figure 5.26d. Moreover, it shows that the pressure distribution and liquid to vapour phase change have been modelled appropriately. There is, however, a small difference between numerical results and experimental data regarding the cavity width.

During the transportation to the downstream, due to over prediction of pressure which itself can be a result of lack of spatial resolution, the cavity shrinks in the simulation much faster than in reality. When the separated cavity reaches the trailing edge region of the foil, the discrepancy between the numerical results and experimental data becomes more obvious, Figure 5.26j. This indicates that the rate of phase change from vapour to liquid is over predicted in the down stream region. The accuracy of condensation prediction depends on several factors such as condensation phase change model (modelling perspective), and computational time and spatial resolution (numerical perspective). The condensation model used in this study is based on the dynamic of a single bubble during the bubble growth which does not include effects of compressibility and strong bubble collapse jet. As it is stated before, the mesh resolution affects the pressure distribution prediction accuracy. Lack of enough spatial mesh resolution will lead to overprediction of vortex coarse pressure which means higher condensation rate for separated cavity.

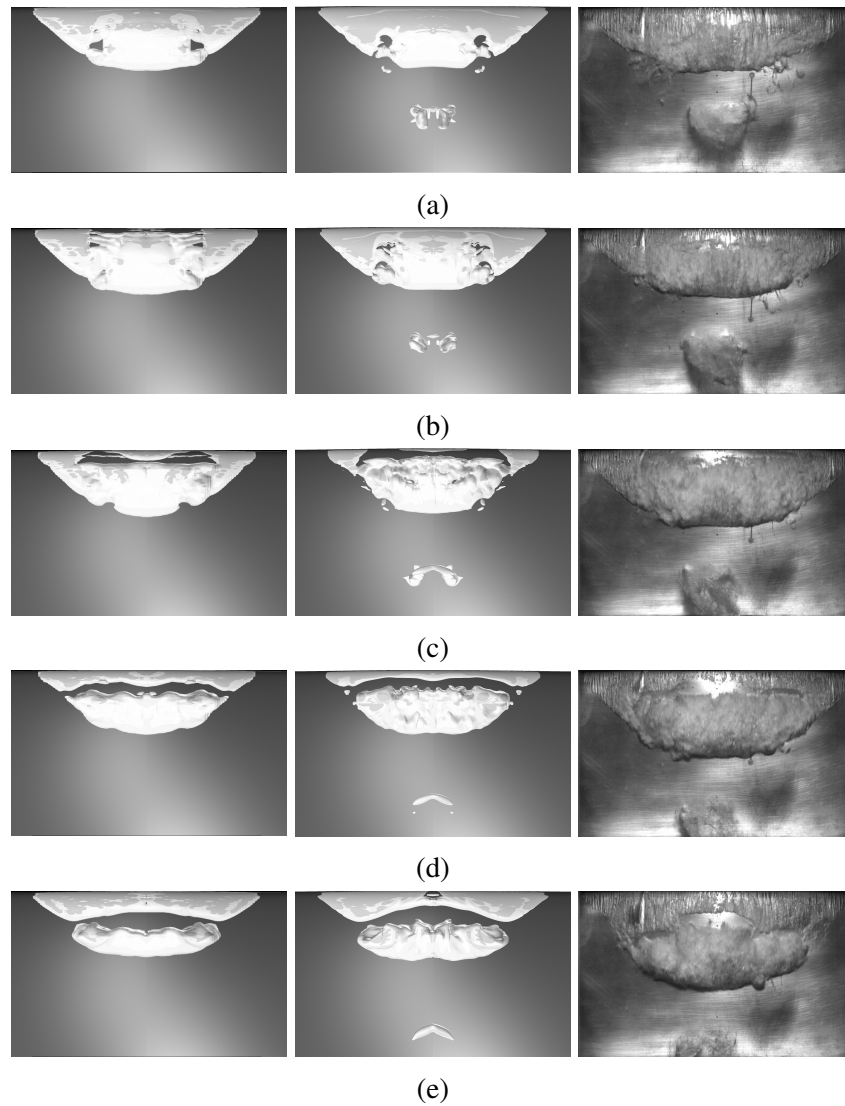


Figure 5.26: Part one - Comparison between numerical results (first column from left: mesh I, second column: mesh IV) and experimental snapshots for cavitation shedding, time step = $1/10T$, vapour iso-surface 10%

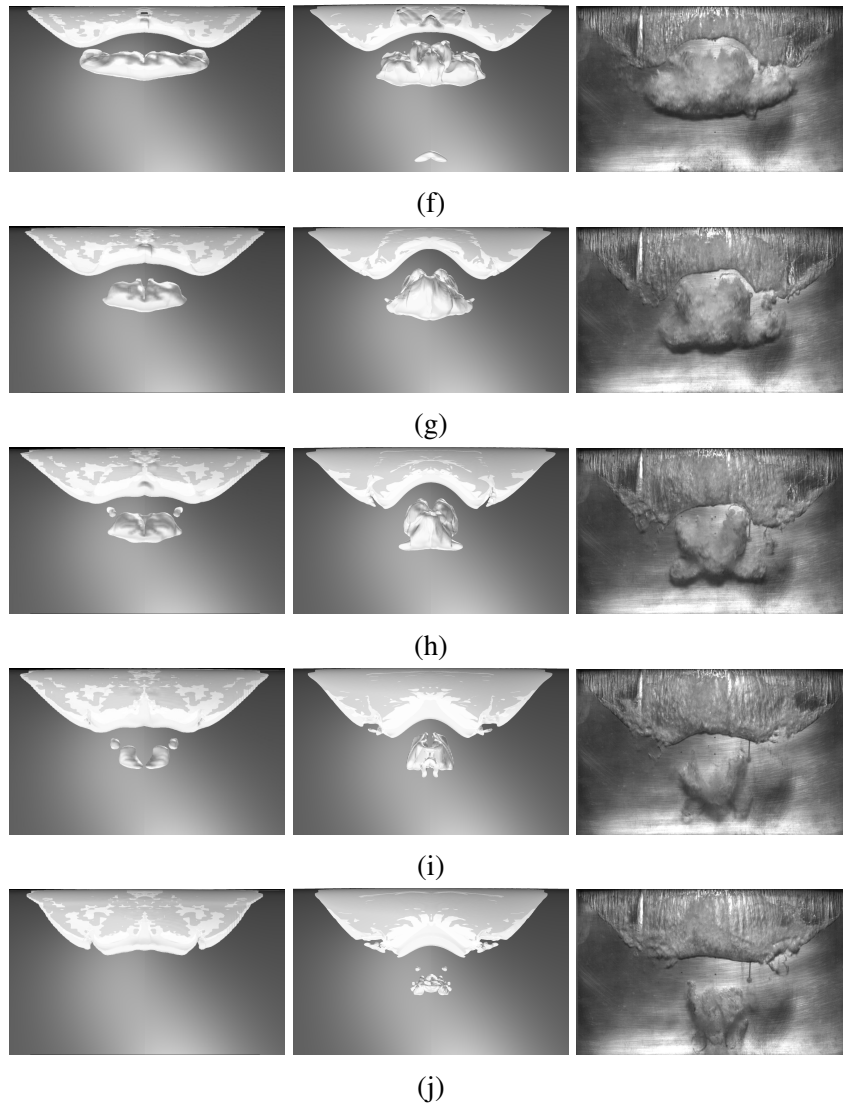


Figure 5.26: Part two - Comparison between numerical results (first column from left:meshI, second column:mesh IV) and experimental snapshots for cavitation shedding, time step = $1/10T$, vapour iso-surface 10%

6

Numerical Results - Cavitating propellers

The most common way to investigate and study cavitating propeller performance is through model scale experiment tests. Considerable cost, long execution time, and scale effects are some of the drawbacks of the experimental analysis of the propellers. Another limitation, and perhaps the most important one, is the limited measurable data that sometimes can only indicate the possible existence of a certain problem (e.g. cavitation) and that will give limited guidance regarding opportunities to redesign a problematic propeller [63].

During the last few decades, numerical methods have been developed to support, and in many cases replace, experimental methods. Even though that some of the todays commonly used numerical tools cannot capture some important characteristics of cavitation which often can be captured in well-executed experiments; these numerical methods require moderate computer resources, and thus can be applied for preliminary analysis and design. However, there is still a need for more advanced computational tools that can approach or in some respects surpass the ability of experimental methods. An application of such advanced methods may thus provide understanding of some cavitation phenomena that are not easily unfolded by experiments, and in this way, contribute to improved prediction and design work [38, 63].

In this chapter numerical analysis and simulation results of cavitation around four model scale propellers are presented. Geometry, experimental details and open-water performance of two of the propellers are openly accessible, the E779A and PPTC propellers. The other two propellers, high skew research propellers from Rolls-Royce having limited openly published data. In order to give different inflow conditions and loads to the blades, PPTC and RR propellers shafts are inclined towards the water flow direction. The inclination of the shaft gives a nonuniform inflow to the propeller which is well defined and gives a load variation on the blades during the rotation. These propellers are selected firstly to verify the computational setup and employed numerical algorithm, secondly to show the

consistency with the previous numerical simulations, and finally to investigate the numerical development and also to analyze the propeller design impact on the flow structure and mostly on the cavitation pattern. Description of experimental tests, mesh topology, and also simulation settings are presented for each of these cases.

The simulations consist of wet flow and cavitating flow conditions. Comparison of thrust and torque coefficients and also the cavity extent at different positions of the blade between numerical simulation and the experimental data are also performed and presented.

For all of the cases, the cavitation simulations are started from the developed wetted flow where the cavitation source were deactivated for the first few time steps to achieve a stabilized pressure field. For wetted flow simulations, nearly 10 time steps per degree of rotation is used, and for cavitating flow simulations, approximately 25 time steps per degree of rotation is used. The first order UPWIND scheme is used for calculation of the convection term in the vapour volume fraction equation, $\text{div}(\phi, \alpha)$ in OpenFOAM. For calculation of the convection term in the Navier-Stokes equation, blended scheme with value 0.2 is used, $\text{div}(\rho\phi, U)$ in OpenFOAM. Second order backward scheme is used to discretize equations in time. The residual of solving equations are set 10^{-6} for wetted flows simulations and 10^{-12} for cavitating flows simulations.

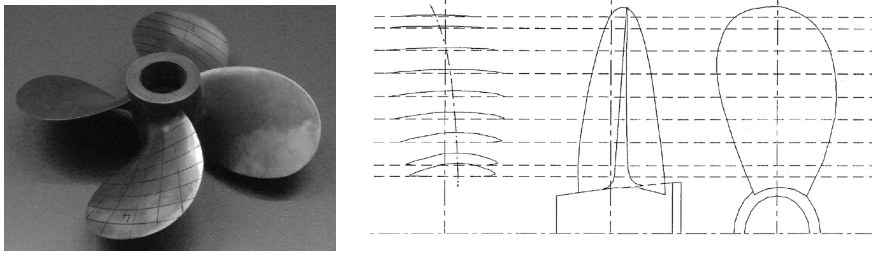


Figure 6.1: E779A propeller

6.1 E779A

INSEAN E779A model propeller is a modified Wageningen propeller characterised by a constant pitch distribution and very low skew. The propeller has been extensively tested experimentally at the Italian Ship Model Basin, INSEAN, and there are some numerical results published for this propeller at different operating conditions [64, 65, 66]. The experimental data and operating conditions of the tested propeller are reported in [67, 68, 69].

E779A propeller has four blades with a uniform pitch (pitch/diameter = 1.1), a forward rake angle of 4 degrees with the diameter of 227.2 mm, Figure 6.1.

6.1.1 Computational domain, grids and simulation conditions

In order to model the moving mesh (i.e. relative motion between the propeller and the external domain), the computational domain has been decomposed in two regions connected to each other through AMI (Arbitrary Mesh Interpolation) boundaries. While the outer region is stationary, the rotation of the region close to the propeller has been handled by `solidBodyMotionFvMesh` library of OpenFOAM. The domain is simplified to a cylinder extending one D_p upstream the propeller and $3.75 D_p$ downstream of the propeller. The surrounding cylinder has the radius of 0.334 m, yielding the same cross-sectional area as the cavitation tunnel, Figure 6.2.

The computational grids have approximately 3.65 million cells composed of tetrahedrals with prisms in the boundary layer region of the blades, see Figure 6.3. In order to appropriately capture the boundary layer over the blades, the surface mesh is extruded normal to the surface to create the prisms cells. The non-dimensionalized height of the first cell (y^+) is set equal to 10 except near the leading edge, where higher velocities lead to slightly higher values.

The flow around the E779A is simulated in three different conditions presented in Table 6.1. In order to validate the employed settings, moving mesh strategy and also to check the quality of the mesh, in two different J values, the noncavitating flows are simulated, and then for $J = 0.71$ the cavitating flow is simulated. For the cavitating flow, the outlet pressure is adjusted to meet the cavitation number

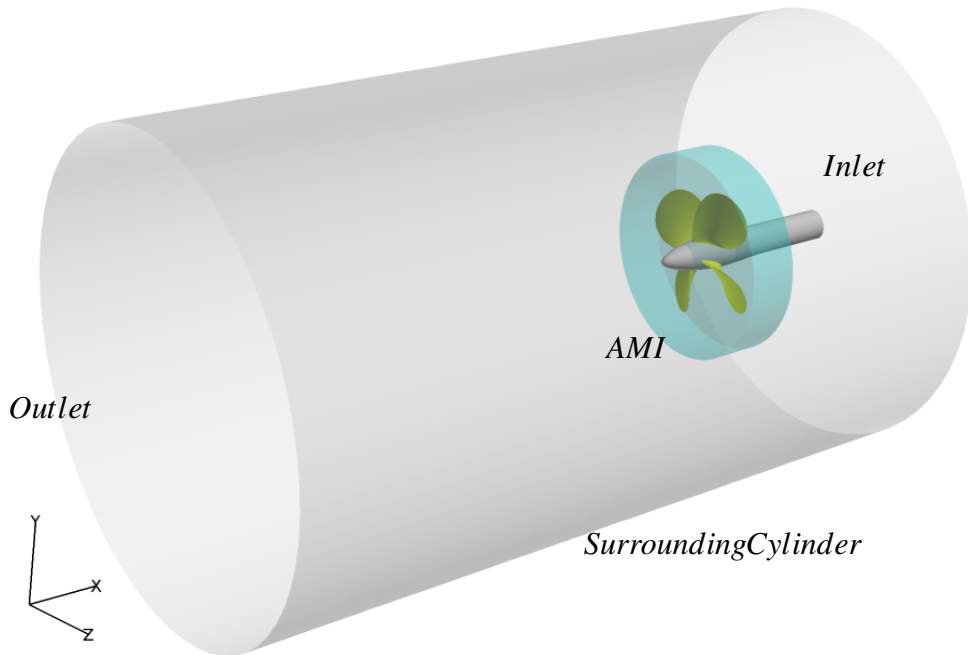


Figure 6.2: Boundaries setting for E779A propeller simulation

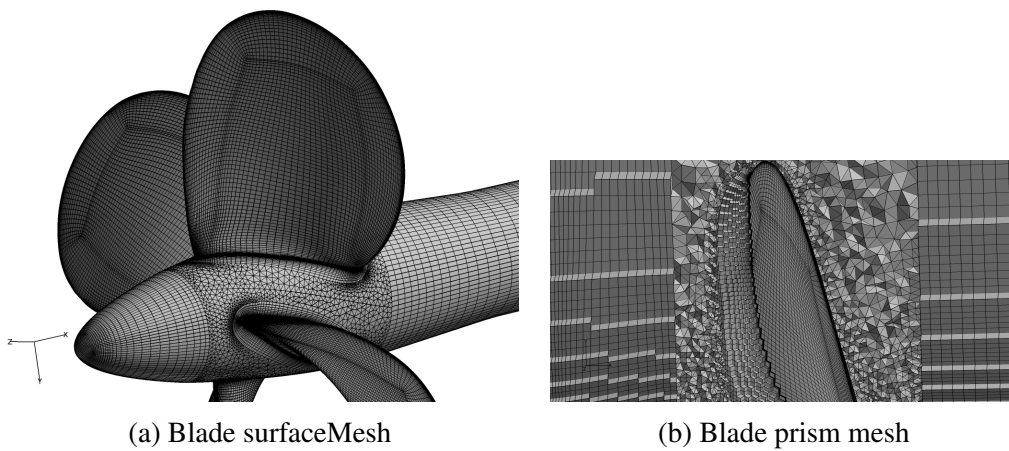


Figure 6.3: Mesh specification of E779A propeller

equal to $\sigma_n = 1.76$.

6.1.2 Noncavitating flow conditions

In Table 6.2, the comparison between numerical results and experimental data for open water characteristics of wetted flow are presented. The forces and moments are here computed for the blades only, in order to compare with the measure-

Table 6.1: Simulation conditions of E779A propeller

J	n (rps)	Inlet velocity (m/s)	Cavitation number
0.88	25	5	Noncavitating Flow
0.71	36	5.808	Noncavitating Flow
0.71	36	5.808	1.76

ments, where the thrust and torque values of the dummy hub condition (without the propeller mounted) are deducted from the total values. The agreement between numerical results and the experimental data is excellent in both cases, see Table 6.1. These two conditions have been chosen since the experiments are focused on $J = 0.88$ for the wetted flow conditions and $J = 0.71$ for the steady cavitating conditions with uniform inflow distribution. The cost to perform these computations using LES prohibits the evaluation of a full propeller characteristics curve.

Table 6.2: Wetted flow open water performance of E779A propeller

J		K_T	$10K_Q$
0.88	Exp	0.157	0.306
	LES	0.154	0.298
	Error(%)	-1.9	-2.6
0.71	Exp	0.256	0.464
	LES	0.256	0.435
	Error(%)	0	-6.2

6.1.3 Cavitating flow conditions

The numerical simulation of the cavitating flow around the E779A propeller is carried out based on the experimental conditions reported in [16, 66, 70, 71]. The selected operating condition has an undisturbed inflow which constitutes a steady cavitating condition, comparing with the experimental results presented in [70]. The rate of revolution of the cavitating condition is $n = 36$ rps and the inlet velocity $U = 5.808m/s$ and the outlet pressure was adjusted to reflect the cavitating condition of $\sigma_n = 1.76$.

The comparison of cavitation extent between numerical results and experimental data is presented in Figure 6.4. Three types of cavitation patterns are observed in the experiment, sheet cavitation on the blade, tip vortex cavitation and hub vortex cavitation. The sheet cavitation is separated from the blade by a vortex and creates tip vortex cavitation which lasts for a few revolutions. The numerical results predicts these two cavitation patterns reasonably good. It should be noted that finer

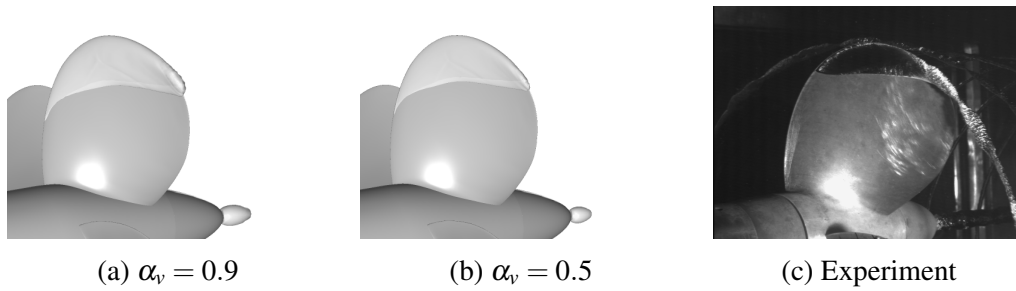


Figure 6.4: Numerical results comparison with experiment, E779A propeller

resolution is needed to capture the physics of a vortex and also to preserve them during transport to the downstream of the flow.

Effects of different mass transfer models (e.g. Kunz, Zwart, and Full Cavitation Model) and their coefficients adjustments on the cavitation extent of E779A have been investigated and reported in the literature, see [16, 66]. In Figure 6.5, the results of modified Schnerr-Sauer model from the current work are compared with the results of other calibrated mass transfer models, [16]. As it is described in the chapter 4, the advantage of using modified coefficients according to the strain rate is that there is no need to calibrate the model coefficients, and the model would be automatically calibrated based on the local flow conditions.

A glimpse conclusion from Figure 6.5 is that the calibrated model has predicted relatively similar cavitation patterns. Even though that the results of Schnerr-Sauer model have better agreement with the experimental observation in the extent of the cavity, results of all of the models over-predict the cavity size. This behaviour which also has been observed in most computations, using a variety of simulation techniques and models, [16, 64, 66], could be due to laminar flow on the blade, geometrical modelling problems, or similar effects.

The open water performance of the propeller in the cavitating condition, thrust and torque coefficients, are presented in Table 6.3. Comparison with the experimental data shows that the performance is correctly captured although slightly underpredicted but consistent with the overpredicted cavity extent.

Table 6.3: Cavitating flow open water performance of E779A propeller

J		K_T	$10K_Q$
	Exp	0.255	0.46
0.71	LES	0.253	0.44
	Error (%)	-0.8	-4.3

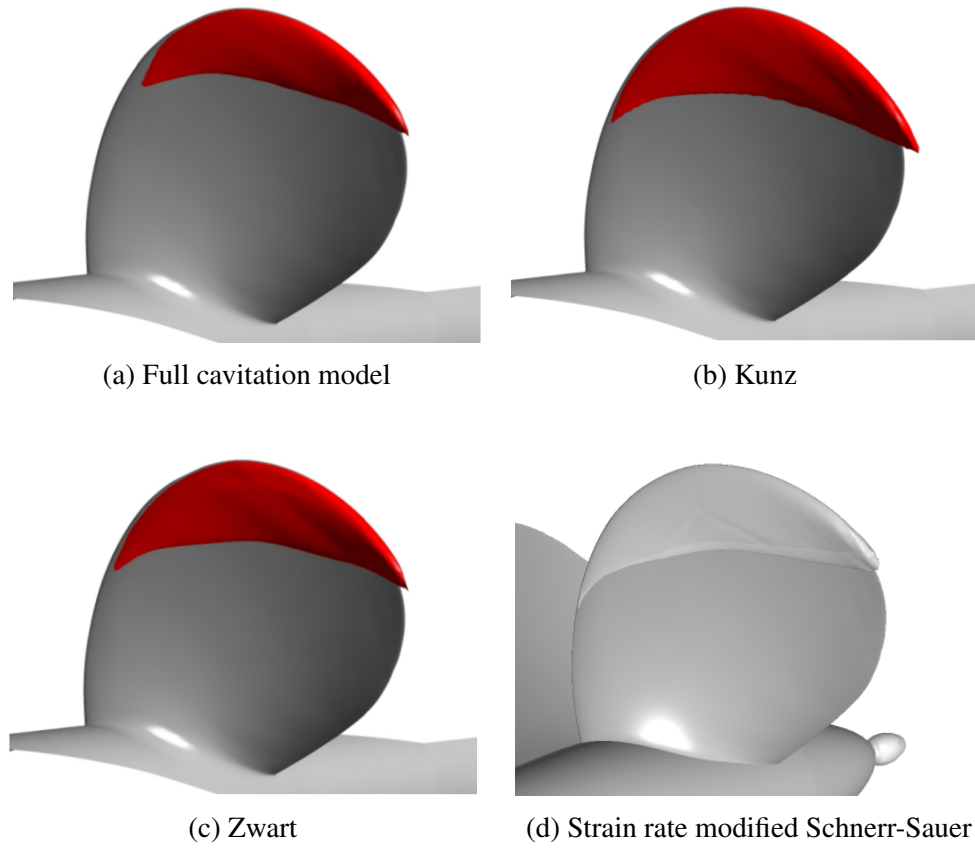


Figure 6.5: Comparison of different calibrated cavitation mass transfer models results for E779A propeller, iso-surface $\alpha_v = 0.5$, (a, b, c) from [16], (d) current results

6.2 PPTC propeller, SMP 2015

6.2.1 Introduction

In this section, numerical simulations of a model scale propeller known as Potsdam Propeller Test Case (PPTC), used as the reference geometry of the 2nd International Workshop on Cavitating Propeller Performance (2015), are presented for both non-cavitating and cavitating flow regimes. The focus of the current simulation is on the second case of the workshop, Cavitation Observation in Oblique Flow. The propeller is a model scale, five bladed propeller with a diameter equal to $D = 250$ mm. The geometry of the propeller including general description, propeller data sheet and also propeller description by radius is open-access and can be found on the webpage of the workshop [72, 73]. In Figure 6.6, the sketch of the propeller geometry is presented.

The open water experimental tests have been carried out for wetted and cavitating flows by SVA Potsdam GmbH in the cavitation tunnel K 15 A where the propeller was positioned with 12 degrees inclination towards the inflow direction, Figure

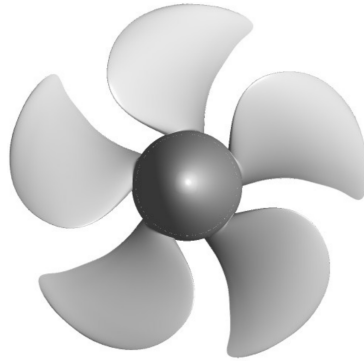


Figure 6.6: SMP'15 propeller geometry

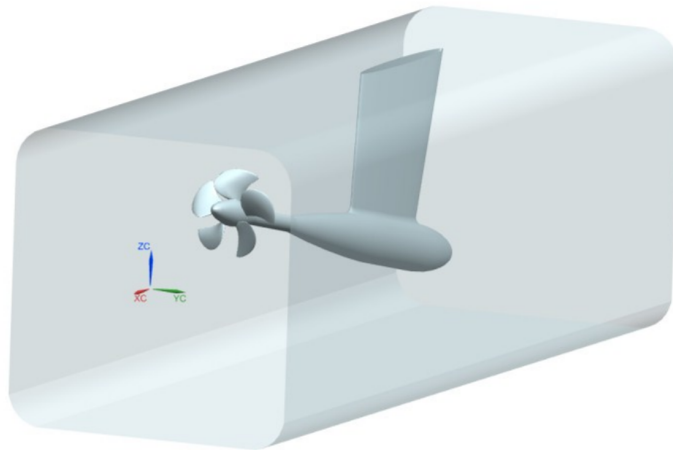


Figure 6.7: SMP'15 propeller and experimental tunnel sketch

6.7. In Table 6.4, the Case2 operating conditions are listed.

The open water performance of the propeller in wetted and cavitating flows is predicted for three operating conditions ($J = 1.019, 1.269$ and 1.408) using hybrid-unstructured grids. The same settings and approaches used in modelling E779A are employed here to simulate the PPTC propeller.

The results consist of the propeller performance predictions in the wetted and cavitating flows (thrust and torque coefficients). Since the experimental data is revealed for just one operating condition (Case2.1, $J = 1.019$ [72]), comparison between numerical results and experimental data is carried out just for this condition. For the cavitating flows, the cavitation pattern at different blade positions are also plotted and investigated. Possible sources of discrepancy between numerical prediction and experimental observations are also discussed.

Table 6.4: Case2 of SMP 2015 operating conditions

Case	J	σ_n	$V_{inlet}(m/s)$	n (rev/s)
2.1	1.019	2.024	5.095	20
2.2	1.269	1.424	6.345	20
2.3	1.408	2.0	7.04	20

Table 6.5: Case2 of SMP 2015 numerical boundary conditions

Boundary	Velocity	Pressure	nu_{sgs}	α
Inlet	Fixed value	Zero gradient	Zero gradient	Fixed value
Outlet	Zero gradient	Fixed value	Zero gradient	Zero gradient
Propeller surfaces	No-slip	Zero gradient	nutUSpaldingWallFunction	Zero gradient
Tunnel walls	Slip	Zero gradient	Zero gradient	Zero gradient

6.2.2 Computational domain and mesh specifications

Summary of the numerical boundary conditions is presented in Table 6.5. The uniform inlet velocity and uniform outlet pressure are adopted to adjust the flow advance ratio and cavitation number. Moreover, in order to reduce the requirement of mesh resolution near the tunnel wall, slip boundary condition is applied for the tunnel wall.

The blade surface mesh consists of quad surfaces which have been extruded in the wall normal direction, $y^+ = 10$, to create prism cells in order to better capture the boundary layer over the blades. The rest of the domain is filled with unstructured tetrahedral cells. Since the flow has higher gradients near the leading and trailing edges and also near the tip region of the blades, the mesh has finer resolution at these parts. In order to limit the mesh size in a reasonable range, the mesh gets coarser with increasing distance from the blades.

In order to handle the rotation of the propeller, the computational domain is decomposed in two regions, the rotating region close to the propeller, and the stationary region. The total size of the mesh is around 4.7 M cells, called SMP-Mesh-I. For this mesh, the domain size of the tunnel has been kept the same as the geometry provided by the workshop committee.

In the provided geometry of the tunnel, the inlet is located only 2D upstream of the propeller where D is the diameter of the propeller. Since the inlet is relatively close to the propeller, it is possible that using uniform inflow as the inlet velocity boundary condition affects the flow around the propeller (e.g. pressure distribution and cavitation pattern). Therefore, another mesh is also created where the inlet is moved 4D further upstream, SMP-Mesh-II in Figure 6.8.

In order to investigate the effects of the mesh resolution on the results, SMP-Mesh-III is created from SMP-Mesh-II where the prism cells around one blade is refined using refineMesh command in OpenFoam. This command splits a hex cell into 2 cells in each direction. Therefore, the final cells are 8 times smaller than the

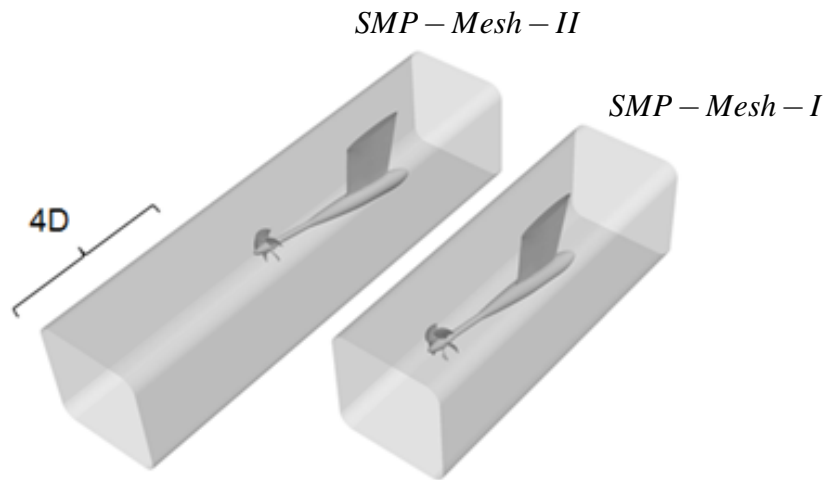


Figure 6.8: The computational domain of SMP-Mesh-I and SMP-Mesh-I

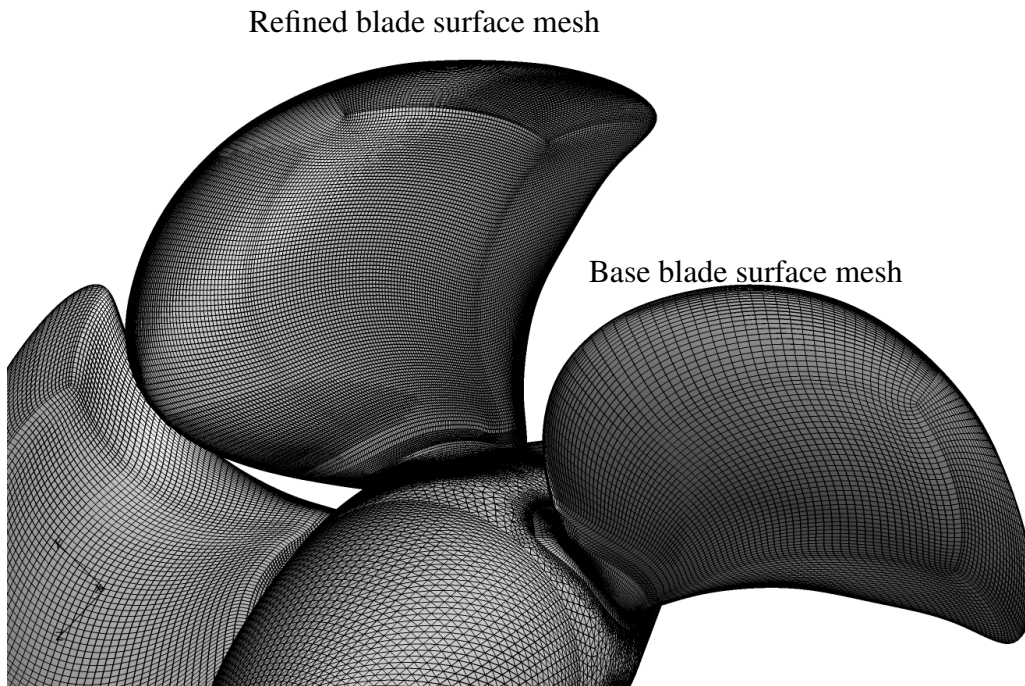


Figure 6.9: The blade surface mesh for SMP-Mesh-III

original one. The final total mesh size is around 8.5 M cells. The blades surface mesh is presented in in Figure 6.9.

6.2.3 Wetted flow numerical results

In Table 6.6, the numerical results for open water performance of PPTC propeller in non-cavitating conditions is presented and compared with available experimen-

tal data. In this table results related to the different computational domain size and also time scheme are also presented. The forces and moments here are computed for the blades only, in order to match with the experimental measurements setup. The comparison indicates good agreement between the numerical results and experimental data for case2.1. Using first order Euler time scheme will increase the numerical diffusion which will lead to higher friction forces acting on the blades which consequently will lead to higher K_Q .

The influence of the inlet distance (SMP-Mesh-I and SMP-Mesh-II) on the wet flow performance of the propeller is also investigated. Since the values presented here is the time-averaged value which do not represent the temporary small size oscillations, the effects of the inlet distance on the wet flow performance is so small and below the simulation error level.

Table 6.6: Wetted flow open water coefficients of PPTC propeller

Operating conditions	Mesh	Time scheme		K_T	$10K_Q$
			Exp	0.397	1.02
Case 2.1	SMP-Mesh-I	backward	ILES	0.405	1.01
	SMP-Mesh-I	Euler	ILES	0.408	1.01
	SMP-Mesh-II	backward	ILES	0.404	1.00
	SMP-Mesh-III	backward	ILES	0.406	1.01
Case 2.2	SMP-Mesh-I	backward	ILES	0.262	0.72
Case 2.3	SMP-Mesh-I	backward	ILES	0.181	0.55

6.2.4 Cavitating flow numerical results

In Table 6.7, the thrust and torque coefficients for three different operating conditions of cavitating flows are presented. For Case2.1 where the experimental data are available, comparison between numerical results and experimental data reveals that the error level of prediction is 8% for K_Q and 4% for K_T using backward scheme. However, the results related to Euler scheme show over prediction of K_Q by 35%.

The lines on the surface of the blades represent the radius ratio, r/R , where R is the propeller radius and r is the distance from the center of the propeller in the cylindrical coordinate system aligned with the propeller rotational axis, Figure 6.10.

6.2.5 Case2.1

In this section the cavitation results for Case 2.1 having operating conditions $J = 1.019$, $n = 20rps$, $\sigma_n = 2.024$ are presented and compared with the experi-

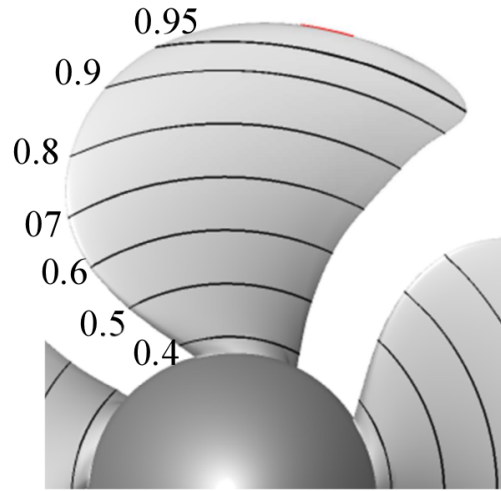


Figure 6.10: Description of radius ratio over the blade surface, view along x-axis

Table 6.7: Cavitating open water coefficients of PPTC propeller

Operating conditions	Mesh	Time scheme		K_T	$10K_Q$
			Exp	0.36	1.02
Case 2.1	SMP-Mesh-I	backward	ILES	0.373	1.07
	SMP-Mesh-I	Euler	ILES	0.351	1.34
	SMP-Mesh-II	backward	ILES	0.374	1.05
	SMP-Mesh-III	backward	ILES	0.375	1.04
Case 2.2	SMP-Mesh-I	backward	ILES	0.196	0.73
Case 2.3	SMP-Mesh-I	backward	ILES	0.157	0.53

mental data. It should be noted that the angular positions are counted in the direction of rotation (right-handed) where zero degree is equivalent to the 12 O'clock position.

In Figure 6.11 cavitation pattern for two iso-surfaces of vapour volume fraction (40% and 60%) are presented for suction and pressure sides of the propeller. These results are related to the SMP-Mesh-I with backward time scheme. Note that we do not see any pressure side cavitation, but the image only reveals the extended sheet of the suction side.

In Figure 6.12 and 6.13, the cavitation predictions are compared with the experimental sketches for Case2.1 for the suction side and pressure side at different blade positions. As it is shown in Figure 6.12, the general trend of the cavitation has been predicted reasonably well. The main difference between numerical results and the experimental data is related to the region with the bubble cavitation

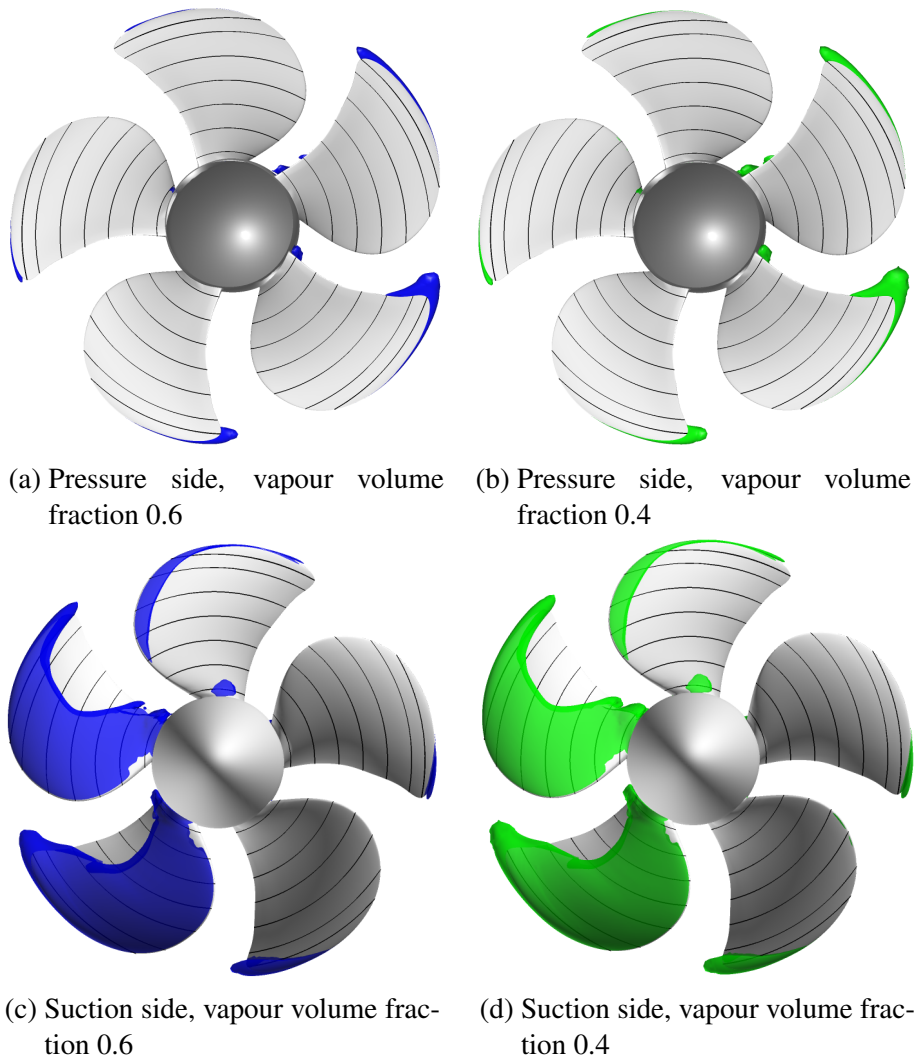


Figure 6.11: Vapor iso-surfaces for Case2.1, SMP-Mesh-I, view along x-axis

pattern in the experimental observation. In Figure 6.12a, the bubbly root cavitation is predicted as sheet cavity, and in Figure 6.12b the bubbly cavitation near the leading edge is predicted with the sheet leading edge cavitation. This sheet cavity then is attached to the near tip sheet cavity (radius 0.9) and covers almost all of the suction side of the blade. The type of bubble cavitation in the experiments indicates a blade pressure close to, or even below, vapour pressure. The modelling used here can not accommodate the growth of individual nuclei to this type of bubble cavitation, instead leading to this formation of a sheet over the leading half of the blade. The pressure side of the blade experiences root cavitation at blade positions of zero and 270 degrees during the experiment. The numerical simulation under predicts root cavitation at zero degree position, and 270 degree blade position.

In Figure 6.14, the pressure coefficient of the wetted flow and also the vapour iso-surface 60% are presented for Case2.1. The pressure coefficient values, Figure 6.14a, are adjusted to show the values below -2 which represent regions with pressure lower than the saturation pressure. At these regions it is probable that cavitation incepts. As it is discussed before, the main discrepancy between cavitation numerical prediction and the experimental observations is related to the prediction of leading edge sheet cavity, e.g. at the blade position 72 and 144 degrees. In the leading edge regions where the numerical prediction show pressure lower than the saturation pressure, the computational model will start to produce vapour. In the experiments, the formation of a sheet cavity depends as well on the nuclei content and nuclei residence time in the low pressure region. This is a modelling discrepancy between the numerical and experimental procedures. Bubble cavitation is observed in the experiment to incept from the leading edge at these positions which suggests a blade pressure close to, or possibly even below, vapour pressure while the numerically predicted pressure at the leading edge is far lower than the saturation pressure in a considerable region. Without further experimental data clarifying the actual blade pressure, its difficult to assess whether the difference in prediction is related to an error in the flow modelling, or if there are, e.g., geometrical differences between the tested and modelled propeller causing this deviation. However, it is also known that a laminar boundary layer can suppress the cavitation inception even though pressure is far below the saturation pressure.

In Figure 6.15, the cavitation prediction for different settings and mesh resolutions are presented for Case2.1 where the vapour iso-surface is 60%. For SMP-Mesh-III, the picture is modified in a way that each blade position is replaced with the corresponding results of the blade having the refined mesh. Therefore, the picture somehow represents the results for an imaginary full refined propeller.

Comparison between Figure 6.15a and Figure 6.15b cannot explain the significant difference in the torque coefficient prediction between Euler and backward time schemes.

Comparison between Figure 6.15a and Figure 6.15c shows that the effects of the inlet distance from the propeller are negligible on the cavitation prediction for this

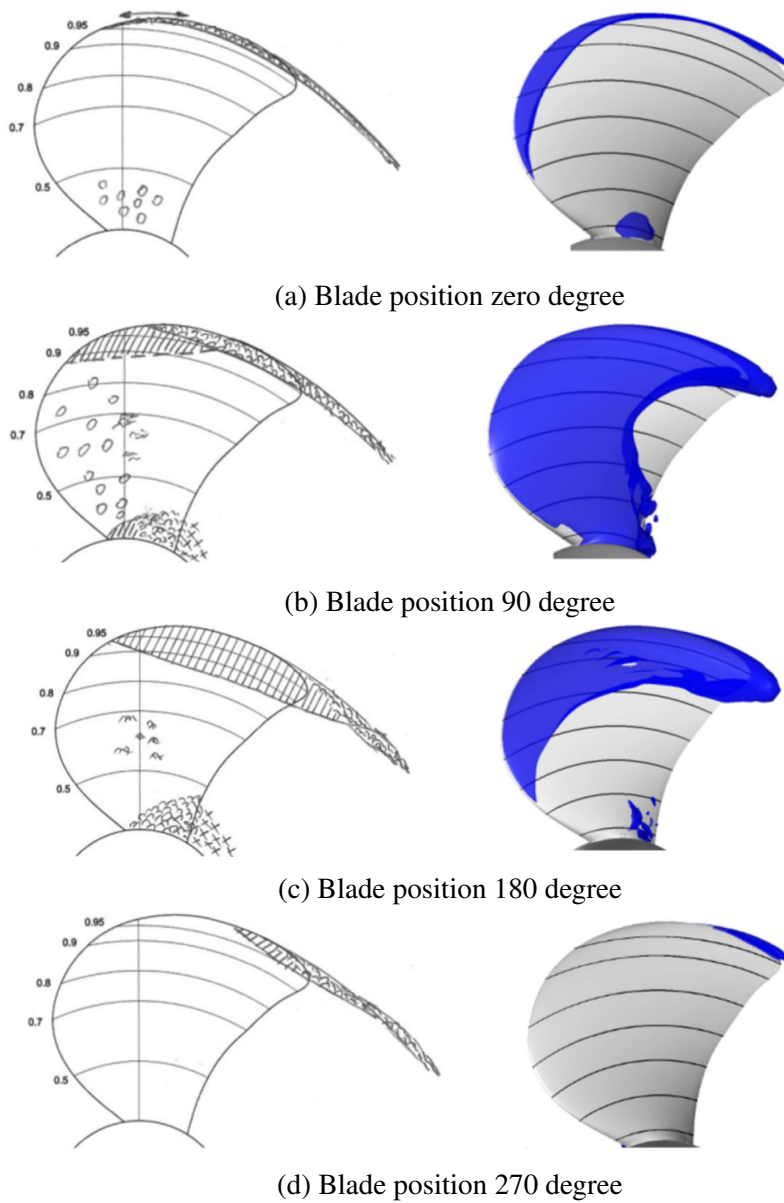


Figure 6.12: Comparison between numerical results and experimental sketches for cavitation in Case2.1, view along x-axis, suction side, numerical results: SMP-Mesh-III, vapour iso-surface: 0.6

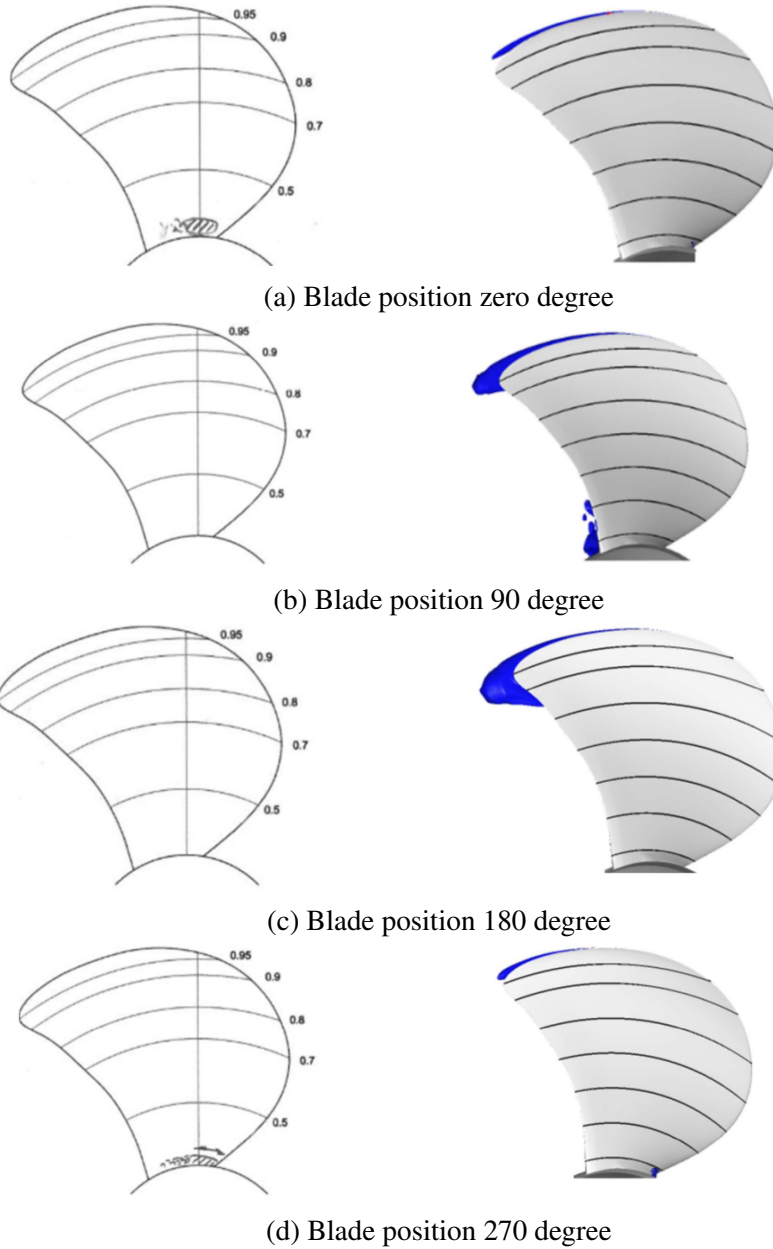


Figure 6.13: Comparison between numerical results and experimental sketches for cavitation in Case2.1, view along x-axis, pressure side, numerical results: SMP-Mesh-III, vapour iso-surface: 0.6

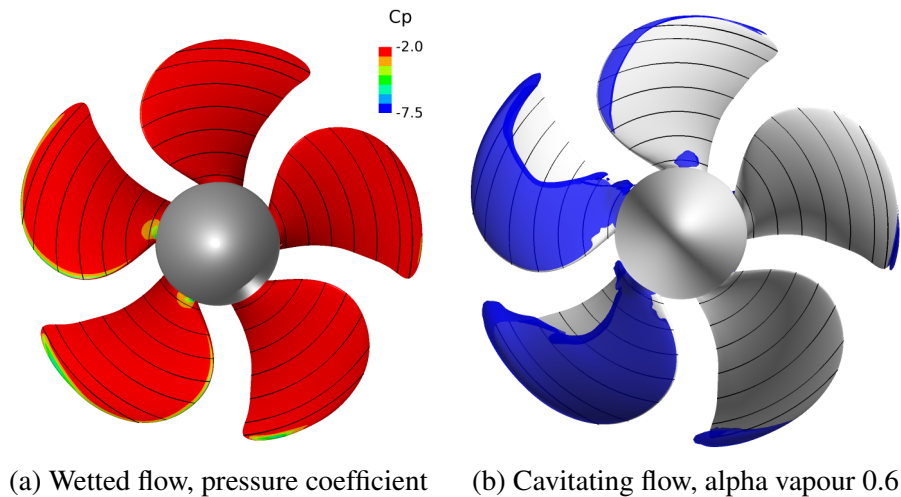


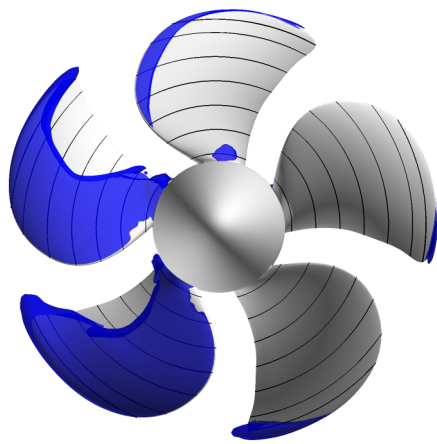
Figure 6.14: Case2.1, view along x-axis, suction side, SMP-Mesh-I

investigated operating condition. The only difference can be seen on the leading edge sheet cavity at the radius ratio between 0.4 and 0.5 where SMP-Mesh-II results show lower amount of cavitation.

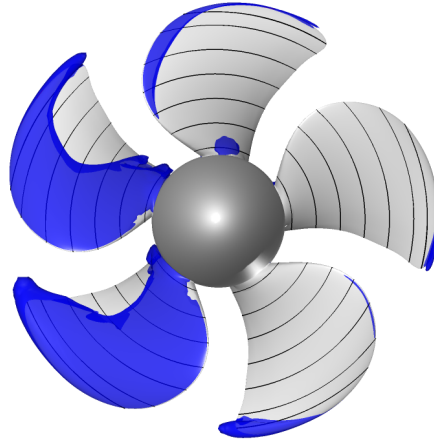
Comparison between results of Figure 6.15c and Figure 6.15d will reveal the effects of refining mesh resolution on the cavitation prediction. From the results it can be deduced that the finer mesh is more capable of capturing and preserving the vortex rolled up into the blade tip region; note that only the region around the blade is refined and not when the vortex has left the blade. From the blade position zero degree, it can be seen that finer mesh resolution is able to preserve the tip vortex cavitation longer, till the end of blade tip while in the coarser mesh the tip vortex cavitation is ended before reaching the blade tip. From the blade position 72 degree, it can be seen that in the finer mesh the vortex is rolled up earlier into blade tip region, and also from the blade position 216 degree, it can be seen that the preserved cavity is bigger than the one in the coarser mesh. We remark that the mesh refinement does not affect the over predicted mid radii sheet cavity.

6.2.6 Case2.2

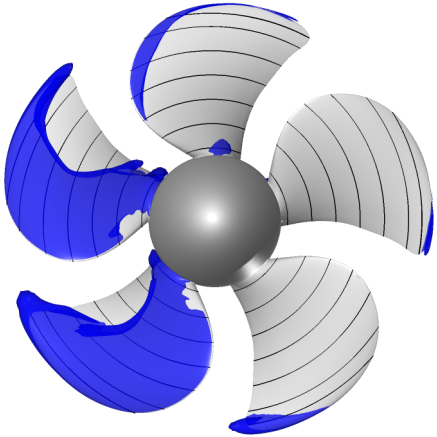
Cavitation prediction of Case2.2, presented in Figure 6.16, shows cavitation appearances on both pressure side and suction side of the blade. It should be noted that the mesh is constructed in a way that it has finer resolution on the suction side of the blades. As a result the cavitation is less resolved on the leading edge of the pressure side comparing to the suction side. The most pronounced feature is the leading edge cavitation which seems to start from the mid-chord of the blade on the suction side and then the cavity extends till the trailing edge.



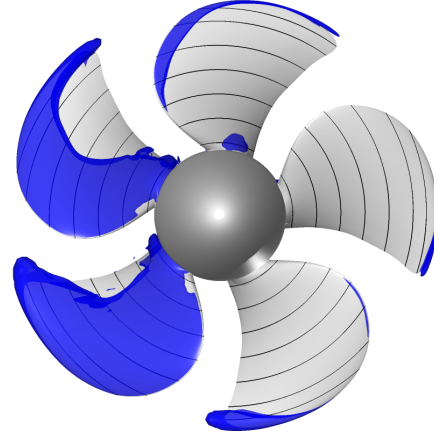
(a) SMP-Mesh-I, backward scheme



(b) SMP-Mesh-I, Euler scheme

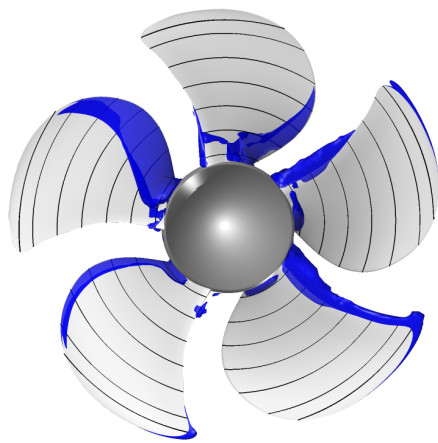


(c) SMP-Mesh-II, backward scheme

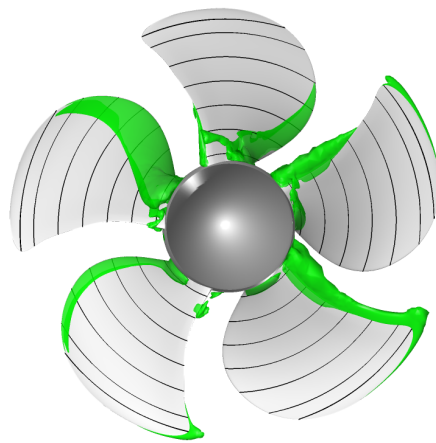


(d) SMP-Mesh-III, backward scheme

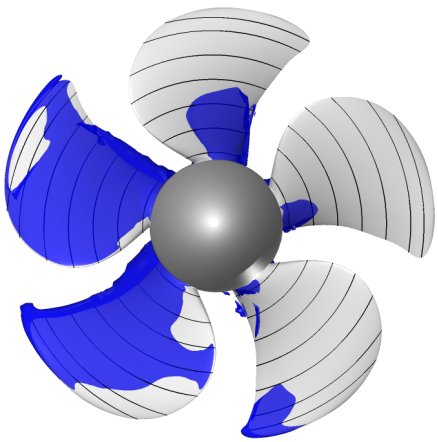
Figure 6.15: Case2.1, view along x-axis, Suction side, vapour iso-surface 0.6



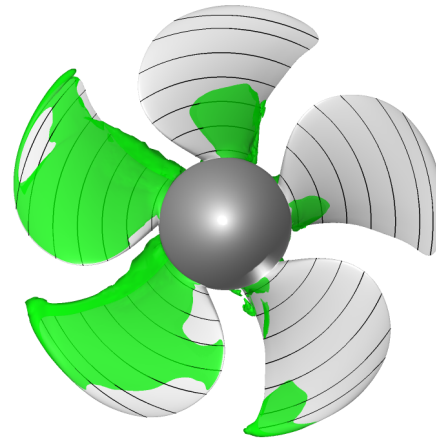
(a) Pressure side, vapour volume fraction 0.6



(b) Pressure side, vapour volume fraction 0.4



(c) Suction side, vapour volume fraction 0.6



(d) Suction side, vapour volume fraction 0.4

Figure 6.16: Vapor Iso-surfaces for Case2.2, SMP-Mesh-I, view along x-axis

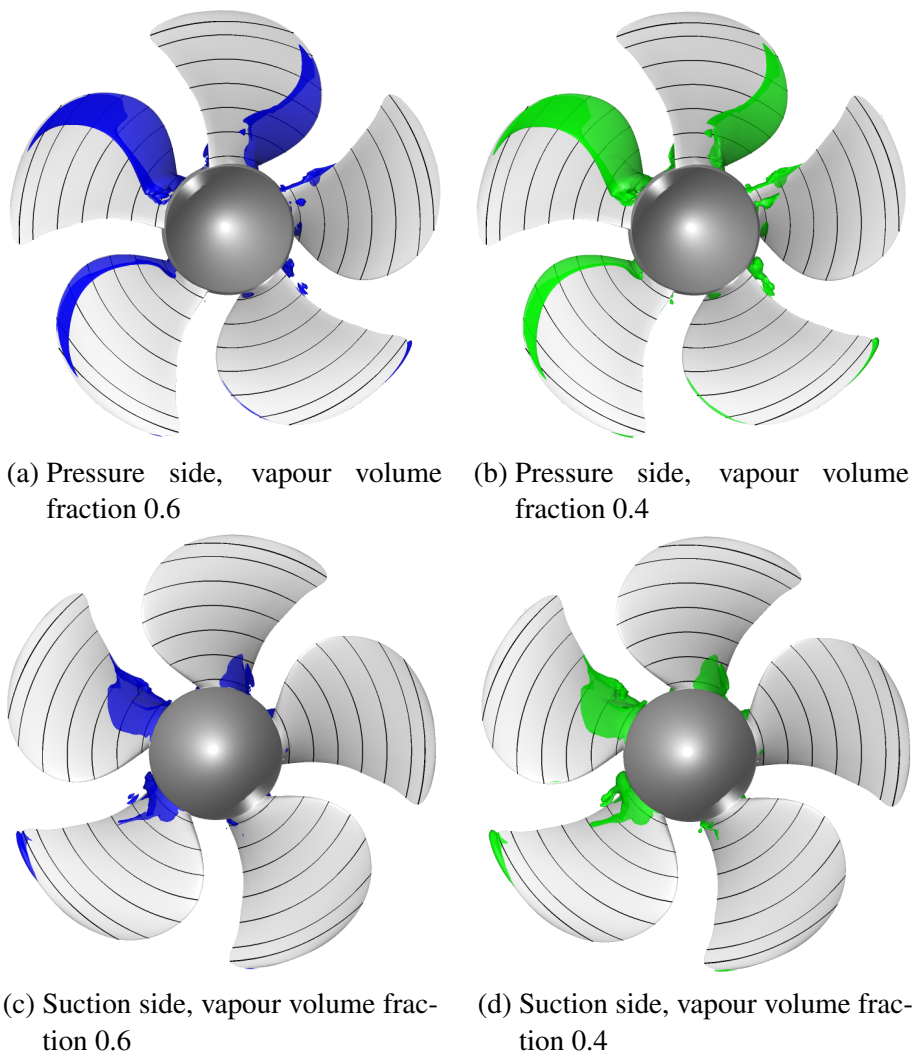


Figure 6.17: Vapor Iso-surfaces for Case2.3, SMP-Mesh-I, view along x-axis

6.2.7 Case2.3

In Figure 6.17, cavitation prediction of Case2.3 is presented. The root cavitation is predicted for both suction and pressure sides of the blade at different positions. The leading edge cavitation is predicted for just the pressure side of the blade. At position 135 degree, tip cavitation is predicted for both sides of the blade.

6.3 Rolls-Royce high skew propellers

In the previous sections, the numerical settings and also the solution algorithm have been verified by comparing the numerical results and experimental data for open access model scale propellers. Here, the simulation has been extended to the industrial propellers in order to provide more detailed information for possible design improvement. Results included here are the wetted flow and cavitating flow simulations of two high skew propellers.

The basic design of the propellers is from a highly skewed propellers research series which has effective tip load and are typical for yachts and Ro-Pax vessels, where it is very important to suppress and limit propeller-induced vibration and noise. In this type of the propeller, the main source of noise and vibration is the vortex cavitation in the tip region. The tip vortex cavitation, and therefore, the noise and vibration is sensitive to modification of the blade's geometry in the tip region. In order to investigate the influence of tip shape and loading on the cavitation behaviour, different designs have been suggested and tested at the RRHRC cavitation tunnel, the Hydrodynamics Research Centre of Rolls-Royce AB, Kristinehamn, Sweden. The focus of the current work is on the analysis of the latest propeller design (called propeller RR-B) and its wetted and cavitating flows performance. However, in order to evaluate the impacts of the design changes; numerical simulation of the previous propeller design (called propeller RR-A) is also conducted.

RR-A propeller has been studied previously in the Department of Shipping and Marine Technology, Chalmers University of Technology, see [38, 63, 74]. In these references, RR-A propeller is named as propeller B. In Figure 6.18, the general sketch of the propeller is presented.

The RR-A and RR-B propellers are simulated with the same settings and strategy as used in this work for the E779A and PPTC propellers. The flow structure, pressure distribution, cavitation pattern and also thrust and torque coefficients are computed for wetted flow and cavitating flow, and are compared with the experimental data. The discrepancy between the numerical results and the experimental data is investigated, and few suggestions are proposed for future experimental tests and also numerical simulations.

6.3.1 Experimental setup

In Figure 6.19, the experimental setup and cavitation tunnel used to test the RR propellers are plotted. In this setup, the water flows from the left side to the right side with a constant velocity. The propeller shaft is inclined towards the water flow direction 10 degrees, Figure 6.20.

After mounting the propeller, the operating condition is set by adjusting the water velocity, revolution rate of the propeller and the pressure of the tunnel. A pilot tube mounted on the lower part of the side wall of the tunnel measures the inflow

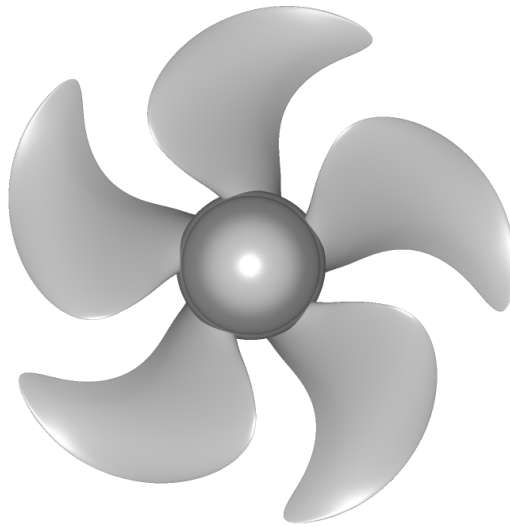


Figure 6.18: The general sketch of the RR propellers geometries

velocity. It is installed far enough from the wall to be sure that it stands outside the boundary layer developed on the bottom wall of the test tunnel. There are also few pressure sensors to measure the pressure at different locations of the tunnel. The thrust and torque are also measured in the rotational axis direction. It should be noted that the forces measured for propeller RR-A and RR-B include blade, hub and cap forces.

The cavitation observed in the experiments is sensitive to the nuclei content of the water and since the cavitation tunnel is a free-surface tunnel the water becomes de-gased after some time running at low cavitation number. The gas content was, therefore, closely monitored and measures were taken to keep the nuclei content on an acceptable level during the measurements.

For both of the propellers, the cavitation behaviour observed in the experiment was relatively intermittent and varied from blade to blade. The latter one can be considered to be related to high sensitivity of the cavitation on these propellers to the pitch adjustment of blade mounting; a deviation of 0.01 degree together with possible manufacturing discrepancy between the blades can result in substantial differences in the amount of cavitation occurring on each blade. Scale effect and also water quality can be other typical reasons for intermittency of the cavitation in this type of cavitation pattern. Considering the limited amount of detailed data measurable in the experiment, the quantitative comparison between numerical simulation and experiments becomes relatively uncertain. Therefore, in order to provide appropriate conditions for comparison, the focus here is put on the investigation and analysis of large and medium-small scales of the flow mechanisms. These scales are related to the mechanisms mainly responsible for creation and development of the cavitation, and also the collapse energy, see [38, 75] for further details.



Figure 6.19: Experimental setting of the propeller cavitation tests



Figure 6.20: Inclined propeller towards the incoming flow in experiment setup

6.3.2 Computational domain and mesh specifications

In Figure 6.21, the computational domain used in simulation of the RR propellers is presented. The computational domain consists of two regions, rotating region close to the propeller, and the outer region which is stationary. The data interpolation between the regions are handled via the AMI boundaries which are colored light blue in the figure.

In order to avoid the possible inflow disturbance effects on the results, the inflow is located $2.5D$ upstream of the propeller, and the outflow is located $5D$ downstream of the propeller where here D is the diameter of the propeller. The outer domain has $2D$ distance from the propeller. Therefore, the contribution of the outer domain boundaries on the flow around the propeller can be neglected, and as a result, coarser grid distribution along with the slip boundary condition are employed for the outer domain boundaries.

Similar to the experimental setup, the water flows from the left side to the right side. The constant inflow velocity (4.2 m/s) is set as inlet velocity boundary condition, and constant pressure (19944 Pa) is employed as outlet pressure boundary condition to set the flow Reynolds and cavitation numbers. The propeller rota-

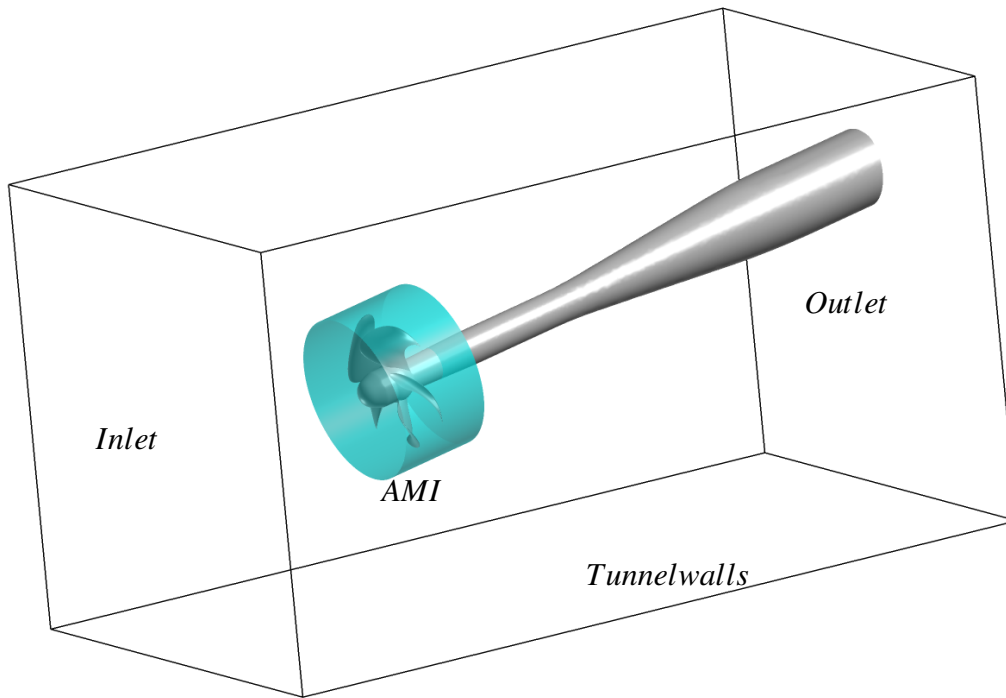


Figure 6.21: Isometric view of the computational domain, RR propellers

Table 6.8: Boundary conditions for cavitation simulation, RR propellers

boundary	velocity	pressure	nuSgs	alpha
Inlet	fixed value	zeroGradient	zeroGradient	fixed value (one)
outlet	zeroGradient	fixed value	zeroGradient	zeroGradient
Blades	no slip	zeroGradient	WallFunction	zeroGradient
Hub and cap	no slip	zeroGradient	WallFunction	zeroGradient
Tunnel walls	slip	zeroGradient	zeroGradient	zeroGradient
Sahft	slip	zeroGradient	zeroGradient	zeroGradient

tional speed is set equal to 17.7 rev/s . In Table 6.8, further information regarding the boundary conditions is presented.

In order to have the same spatial mesh resolution with the previous study, the same computational grids near the blades are employed for proepeller RR-A where the grid type is named CoarseII in [63]. The near wall resolution of the blade is around $y^+ = 30$ and therefore a wall model, `nutUSpaldingWallFunction`, is used to correct the viscosity of the flow near the wall. The computational domain of RR-A propeller consists of 8.7 million cells which are composed of tetrahedrals with prism layers of hexahedrals around the blades, hub and shaft, Figure 6.22. The mesh is named Mesh-RR-A-1 in this study.

For propeller RR-B, two different mesh structures are considered. The first mesh,

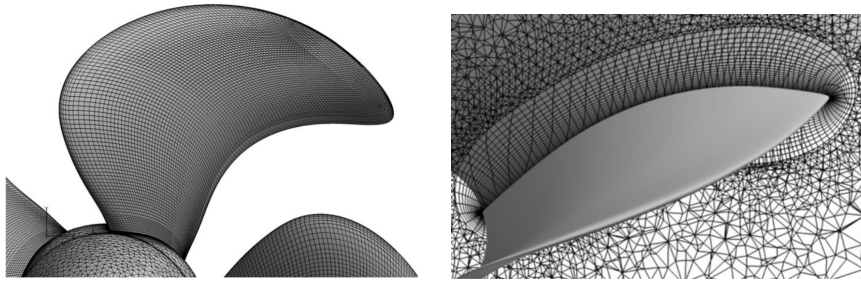


Figure 6.22: Surface mesh and closed-up views of volume mesh around the blades of the the propeller RR-A

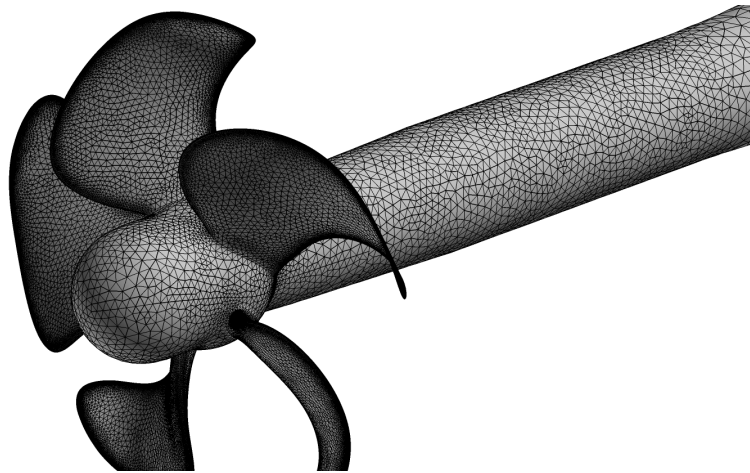


Figure 6.23: Triangular surface mesh of the propeller RR-B, Mesh-RR-B-2

Mesh-RR-B-1, is created by using the same mesh topology as used in the RR-A propeller, employing the quad surfaces on the blades surfaces, and then extrusion of this surface mesh to create prismatic layers around the blades and at the last step, using tetrahedral cells to fill the rest of the domain where the total mesh size is around 7.5 M cells. For this mesh, the near wall resolution of the mesh (y^+) is around 20. The second mesh topology, Mesh-RR-B-2, is composed of triangular prisms near the blades and tetrahedral cells in the rest of the computational domain, totally 13.7 M cells. The surface mesh distribution of this mesh is presented in Figure 6.23. For both of the meshes, the mesh is finer near the leading edge, trailing edge and also tip of the blades in order to capture more physics of the flow at these regions.

6.3.3 Wetted flow numerical results

In Table 6.9, thrust and torque coefficients are presented for wetted flows of the propellers RR-A and RR-B. These results have been obtained by using the same settings which are used to simulate E779A and PPTC propellers. However, while

the error level in prediction of the thrust coefficients of E779A, PPTC and RR-A propellers is around 2%, the thrust coefficient prediction error level of the RR-B propeller is around 7%.

Table 6.9: Wetted flow open water performance of the RR propellers

Propeller		Mesh	K_T	$10K_Q$
RR-A	Experiment		0.289	0.631
	ILES	Mesh-RR-A-1	0.282	0.636
RR-B	Experiment		0.291	0.644
	ILES	Mesh-RR-B-1	0.272	0.593
	ILES	Mesh-RR-B-2	0.269	0.590

6.3.4 Cavitation prediction of the RR-A propeller

In Table 6.10, the numerical prediction of open water performance of the propeller RR-A (thrust and torque coefficients) in the cavitating conditions are presented and compared with the experimental data where the error level of prediction of the forces (i.e. thrust coefficient) is -3.5%.

Comparing the thrust coefficients of the wetted flow conditions, Table 6.9, and the results for cavitating flows reveals that the thrust coefficient has dropped around 1%. Noting that the amount of the thrust coefficient reduction measured in the experiment between the wetted flow and cavitating flow is also around 1% suggests that numerical simulation can predict the flow trend.

Table 6.10: Cavitating open water performance of the propeller RR-A

Operating conditions	K_T	$10K_Q$
Experimental data	0.289	0.620
Numerical results	0.279	0.630
Error (%)	-3.5	1.6

In Figure 6.24, the numerical prediction of cavitation (vapour iso-surface 50%) has been compared with the experiment. In the experiment tests it is observed that the sheet cavity starts from the vortex core and grows toward the blade tip. The current numerical simulation is able to predict the sheet cavity near the tip region. Moreover, in the numerical results, the root cavitation is predicted as sheet cavitation. The root cavitation observed in the experiment is partly composed of large travelling single bubbles and partly of a glassy sheet cavitation. The vapour iso-surface and pressure coefficient distribution for cavitating flows of RR-A pro-

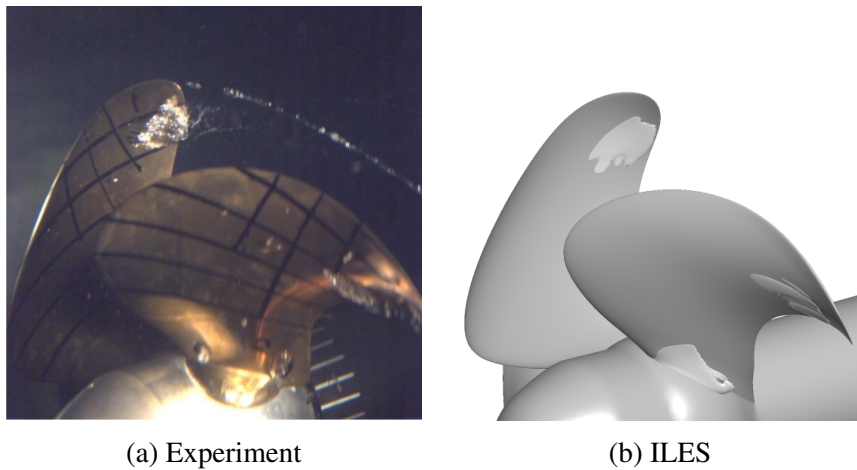


Figure 6.24: Side view of numerical predictions vapour Iso-surfaces (50 %) and experimental snapshot, RR-A propeller

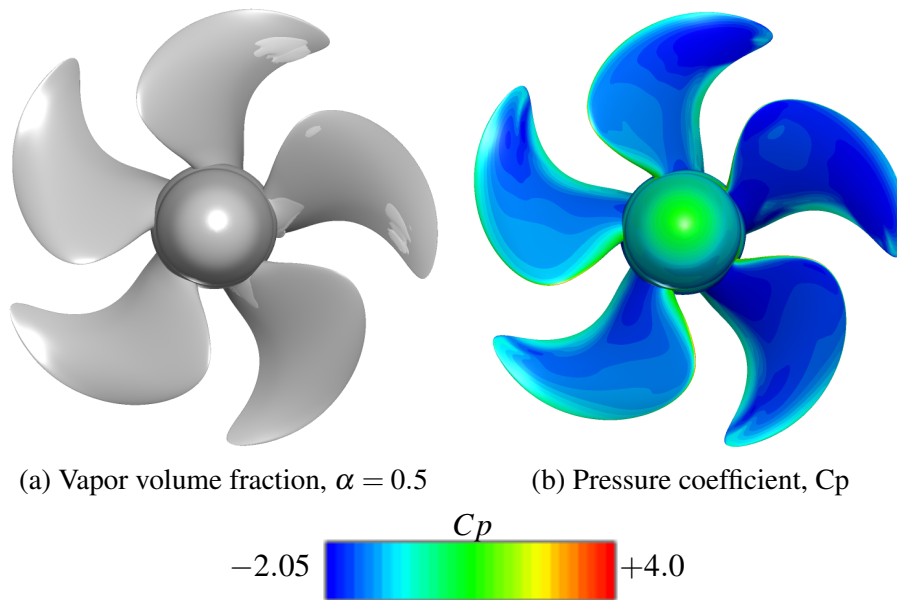


Figure 6.25: Front view of numerical predictions vapour Iso-surfaces (50 %) and pressure coefficients of RR-A propeller

propeller are presented in Figure 6.25.

6.3.5 Cavitation prediction of the RR-B propeller

The open water performance of RR-B propeller in the cavitating conditions is presented in Table 6.11. The error level of the thrust coefficient prediction with Mesh-RR-B-1 is 5.1% and with Mesh-RR-B-2 is 6.5%. One possible reason for having better prediction in Mesh-RR-B-1 is having finer mesh resolution near the

tip and also leading edge of the blades which helps to capture the high gradient nature of the flow at these regions more accurately.

Table 6.11: Cavitating open water performance of the propeller RR-B

Operating conditions	Mesh	K_T	$10K_Q$
Experimental data	—	0.292	0.641
Numerical results	Mesh-RR-B-1	0.277	0.616
	Mesh-RR-B-2	0.273	0.609

In Figure 6.26, the pressure coefficient distribution and vapour iso-surfaces (50 %) of cavitating flow simulations for RR-B propeller are presented for two different meshes. In Figure 6.28, the vapour iso-surfaces are compared with the experimental observation.

The first impression from the comparison is that the total extent of the predicted cavitation is larger than found in the experimental observations. The numerical simulations predict cavitation near the leading edge (e.g. blade position 270 degree) while leading edge sheet cavitation is not found in the experiments. During the experiment, it is observed that the leading edge area may show bubble cavitation, Figure 6.28c. Similar to the cavitation analysis of PPTC propeller, this indicates that the pressure at this region is close to, or even lower than, the saturation pressure.

The simulation results also show root cavitation formation in the blade positions 270 degree till zero degree. In the experiments some cavitation found at the root section but the amount predicted in the numerical simulation is larger.

Comparing the cavitation at the blade position 30 degree for Mesh-RR-B-1, Figure 6.26a, and Mesh-RR-B-2, Figure 6.26b, shows that results related to Mesh-RR-B-2 better predict the vortex separation from the tip blade region, and the shape of the cavity closure at this region is more similar to the experimental observations. One reason can be over prediction of cavitation in blade position 320 degree of Mesh-RR-B-1 which lead to over prediction of cavitation in the blade position 30 degree. In Figure 6.27, the zoomed in view of the tip region for two different blade positions are provided. It can be seen that the cavity reaches the trailing edge in results related to Mesh-RR-B-1 which affects the pressure distribution and vortex structure on the tip region.

In Figure 6.29, the vapour iso-surfaces 10% are plotted. From this figure, it can be seen that the results related to Mesh-RR-B-2 are more dependent on the mesh distribution. Moreover, the difference between cavity shape which can be seen in Figure 6.26a and Figure 6.26b at blade position 270 degree, is less obvious in the vapour iso-surfaces 10% pictures. It can be seen from this figure that at the blade position 180 degree, Mesh-RR-B-2 predicts cavitation appearance at the leading edge which is not observed in the experiment.

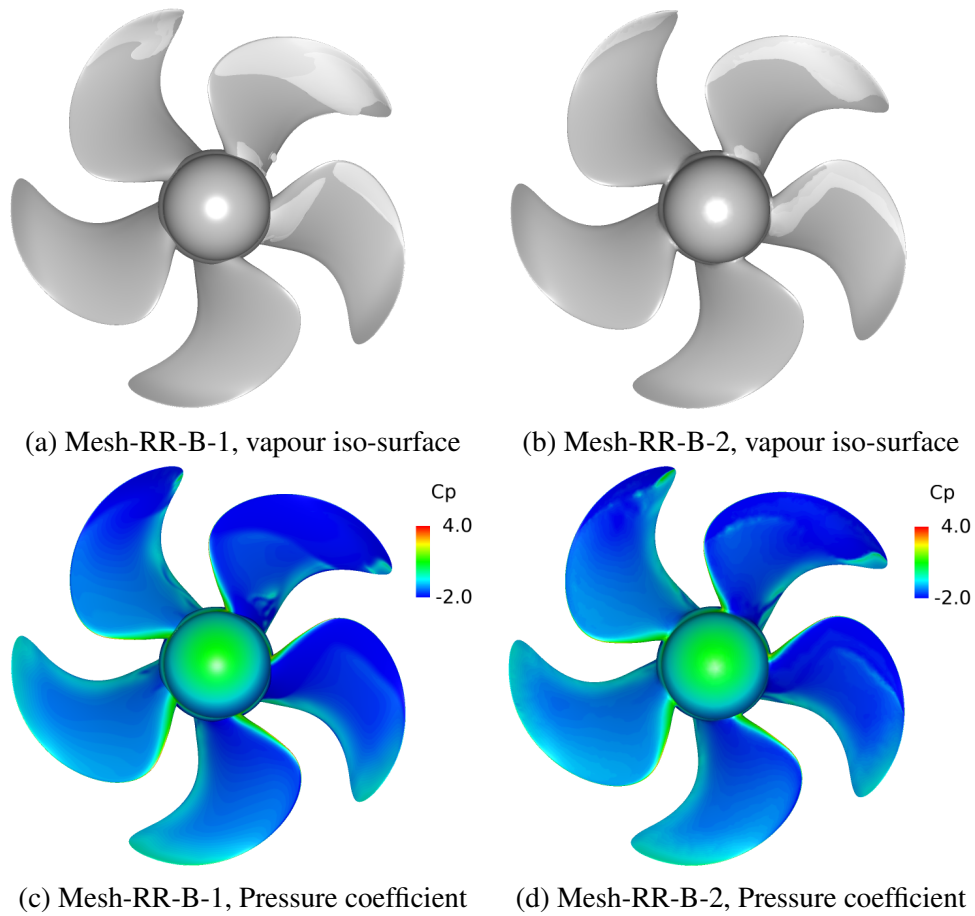


Figure 6.26: Pressure coefficient distribution and vapour iso-surfaces (50 %) of cavitating flow simulations for RR-B propeller

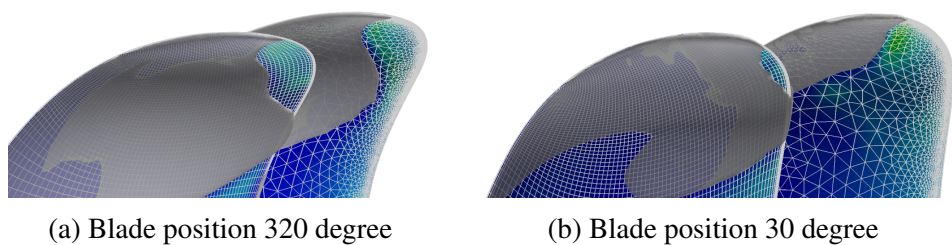


Figure 6.27: Zoomed in view of vapour iso-surfaces (50 %) and pressure coefficient distribution of numerical results for RR-B propeller

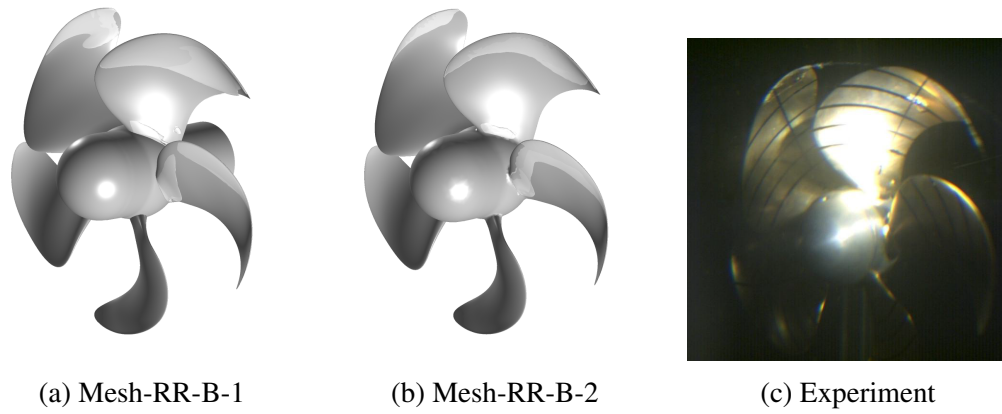


Figure 6.28: Comparison between vapour iso-surfaces (50 %) of numerical results and experimental observations for RR-B propeller

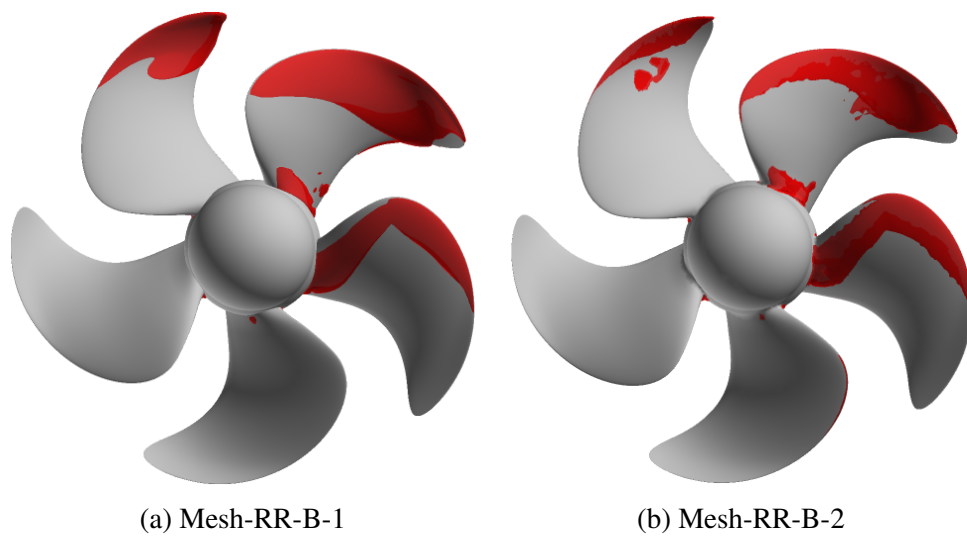


Figure 6.29: Vapor iso-surfaces (10 %) of numerical results for RR-B propeller

7

Summary and suggestions for future work

In the following, the current work is concluded and few suggestions for future work are presented.

- One of the main focuses of the current work is the spatial mesh resolution effects on the cavitating flow predictions. However, the solution resolution is dependent on both the computational grid resolution and the order of the discretization schemes. Therefore, it would be also interesting to investigate the effects of the different numerical schemes on the solution accuracy and on the stability of the solution and investigate its interactions with the spatial mesh resolution. Preliminary results (not reported here) of RR-A propeller indicate that the flow structure, e.g. vortex strength, is directly dependent of the numerical schemes. Using diffusive schemes will smear out the vortex and predicts more uniform pressure distribution. Moreover, from the cavitation results it is deduced that the two-phase vortex strength is dependent on both the schemes used in Navier-Stokes and vapour volume fraction transport equation.
- The current numerical results indicate the dependency of the cavity closure region and also cavity collapse to the spatial mesh resolution. Since the collapse is dependent on the resolution, the collapse induced pressure pulses are also dependent on the resolution. The collapse occurs in a very small fraction of time, and therefore this pressure oscillation does not affect the force prediction but the erosion and noise prediction will be affected. One suggestion is using very fine resolution in the closure regions which could be very costly. Another suggestion is using automatic mesh refinement approach to refine the computational cells in the regions that collapse occurs.
- To calibrate the mass transfer rate, the velocity strain time scale are suggested and tested. It was shown that using this time scale will improve the accuracy of the pressure distribution and also cavitation pattern predictions.

Moreover, it is highlighted in E779A propeller simulation that different calibrated mass transfer models lead to similar results and cavitation prediction.

- The shear stress effects on the rupturing of the liquid pocket is modelled by considering the velocity strain rate as an appropriate approximation for the magnitude of shear stress tensor.
- The open-water performance predictions for Rolls Royce high skew propellers have lower accuracy comparing to E779A and PPTC performance predictions. In the later two propellers, effects of the hub is deduced from the total forces and the forces are measured just over the blades. Therefore, it is suggested for future experimental tests on Rolls Royce propellers to measure the effects of dummy hub, and reduce it from the total forces.
- The numerical simulations on PPTC propeller and also RR-B propeller show sheet cavitation on the leading edge of the propeller while bubble cavitation is observed in the experiment to incept from the leading edge. It might be deduced that this is a modelling discrepancy between the numerical and experimental procedures. Appearance of bubble cavitation in the experiment on the leading edge suggests that pressure at the leading edge is close to, or possibly even below, the saturation pressure while the numerically predicted pressure at the leading edge is far lower than the saturation pressure in a considerable region. Without further experimental data clarifying the actual blade pressure, its difficult to assess whether the difference in prediction is related to an error in the flow modelling, or if there are, e.g., geometrical differences between the tested and modelled propeller causing this deviation. However, it is also known that a laminar boundary layer can suppress the cavitation inception even though pressure is far below the saturation pressure. Therefore, it is suggested to measure the pressure over the blade, e.g. by using Pressure-Sensitive Paint.
- Numerical simulation around the tested RR propellers show that the flow around the blade is mostly dominated by the vortex structure near the tip region and also tip vortex cavitation.
- In the current work, the first order UPWIND scheme is used as the discretization scheme to calculate the vapor volume fraction on the computational cells' faces. The volume fraction transport equation of the vapour is a pure convection equation with a source term representing the mass transfer between vapour and liquid. Therefore, the truncational error of the discretization scheme would interact with the mass transfer model, and phases transport characteristics. In the case that a first order scheme (either in time or space) is used for the discretization, the truncational error level will be second order, and therefore the error would act similar to a dispersion term knowing as artificial viscosity. This will lead to smearing the vapour volume fraction, and damping out the sharp interface. Depending on the pressure

distribution, this can increase the area covered with vapour. Subsequently, this will affect the pressure field and the forces, and finally the results would be affected by this smearing and truncation error. The truncation error level of a second order scheme is third order and would cause dispersion of the phases. Dispersion would create unrealistic scattering of phases distributions and therefore oscillation in the flow fields and instability in the solution convergence.

REFERENCES

- [1] Jean-Pierre Franc and Jean-Marie Michel. *Fundamentals of cavitation*, volume 76. Springer, 2006.
- [2] Eric Goncalvs and Boris Charrire. Modelling for isothermal cavitation with a four-equation model. *International Journal of Multiphase Flow*, 59(0):54 – 72, 2014.
- [3] JS Carlton. 9 - cavitation. In JS Carlton, editor, *Marine Propellers and Propulsion (Second Edition)*, pages 205 – 246. Butterworth-Heinemann, Oxford, second edition edition, 2007.
- [4] Youcef Aït Bouziad. *Physical modelling of leading edge cavitation: Computational methodologies and application to hydraulic machinery*. PhD thesis, Citeseer, 2006.
- [5] A. Philipp and W. Lauterborn. Cavitation erosion by single laser-produced bubbles. *Journal of Fluid Mechanics*, 361:75–116, 4 1998.
- [6] Propeller erosion brighthubengineering. <http://www.brighthubengineering.com>. Accessed: 2015-4-14.
- [7] J.P. Franc and J.M. Michel. Attached cavitation and the boundary layer: experimental investigation and numerical treatment. *Journal of Fluid Mechanics*, 154:6390, 1985.
- [8] L. Tassin and S. L Ceccio. Examination of the flow ear the leading edge of attached cavitation. part 1; detachment of two-dimensional and axisymmetric cavities. *Journal of Fluid Mechanics*, 376:61–90, 1998.
- [9] Vijay H Arakeri. Viscous effects on the position of cavitation separation from smooth bodies. *Journal of Fluid Mechanics*, 68(04):779–799, 1975.
- [10] G.H. Schnerr, I.H. Sezal, and S.J. Schmidt. Numerical investigation of three dimensional cloud cavitation with special emphasis on collapse induced shock dynamics. *Physics of Fluids*, 20, 2008.

REFERENCES

- [11] A.H. Koop. *Numerical simulation of unsteady three-dimensional sheet cavitation*. PhD thesis, University of Twente, 2008.
- [12] R.T. Knapp, J.W. Daily, and F.G. Hammitt. *Cavitation*. In *McGraw-Hill*, 1970.
- [13] An introduction to propeller cavitation international institute of marine surveying. <http://iims.org.uk>. Accessed: 2015-02-24.
- [14] Aurlia Vallier. *Eulerian and Lagrangian cavitation related simulations using Open-FOAM*. PhD thesis, Licentiate thesis, Lund University, Lund, Sweden, 2010.
- [15] Aurlia Vallier. *Simulations of cavitation from the large vapour structures to the small bubble dynamics*. PhD thesis, PhD thesis, Lund University, Lund, Sweden, 2013.
- [16] Dott. Mitja Morgut. *Prediction of non-cavitating and cavitating flow on hydrofoils and marine propellers by CFD and advanced model calibration*. PhD thesis, Universit Degli Studi Di Udine, 2012.
- [17] Mitja Morgut, Enrico Nobile, and Ignacijo Bilu. Comparison of mass transfer models for the numerical prediction of sheet cavitation around a hydrofoil. *International Journal of Multiphase Flow*, 37(6):620 – 626, 2011.
- [18] Youcef Ait Bouziad. *Physical modelling of leading edge cavitation: computational methodologies and application to hydraulic machinery*. PhD thesis, cole Polytechnique Federale De Lausanne, 2005.
- [19] A. Prosperetti and G. Tryggvason. *Computational methods for multiphase flow*. Cambridge University Press, 2007.
- [20] M. Ishii and T. Hibiki. *Thermo-fluid dynamics of two-phase flow*. Springer Verlag, Berlin, 2006.
- [21] Y. Ventikos and G. Tzabiras. A numerical method for the simulation of steady and unsteady cavitating flows. *Computers and Fluids*, 29(1):63–88, 2000.
- [22] S.J. Thalhamer M. Schmidt and G.H. Schnerr. Inertia controlled instability and small scale structures of sheet and cloud cavitation. In *7th International Symposium on Cavitation, CAV2009, Ann Arbor, Michigan, USA, 2009*.
- [23] S.J. Schmidt, I.S. Sezal, and G.H. Schnerr. Compressible simulation of high-speed hydrodynamics with phase change. In *European Conference on Computational Fluid Dynamics, ECCOMAS CFD, Egmond aan Zee, The Netherlands, 2006*.
- [24] J.L. Reboud and Y. Delannoy. Two-phase flow modelling of unsteady cavitation. In *2nd International Symposium on Cavitation, Tokyo, Japan, 1994*.
- [25] R. Fortes-Patella O. Coutier-Delgosha and J.L. Reboud. Evaluation of the turbulence model influence on the numerical simulations of unsteady cavitation. *Journal of Fluids Engineering*, 125(1):28–45, 2003.

-
- [26] J.-A. Astolfi O. Coutier-Delgosha, F. Deniset and J.B. Leroux. Numerical prediction of cavitating flow on a two-dimensional symmetrical hydrofoil and comparison to experiments. *Journal of Fluids Engineering*, 129(3):279–292, 2007.
- [27] S. Gopalan and J. Katz. Flow structure and modeling issues in the closure region of attached cavitation. *Physics of Fluids*, 12(4):895–911, 2000.
- [28] J. Sauer. *Instation ar kavitierende Strmungen - Ein neues Modell, basierend auf Front Capturing (VoF) und Blasendynamik*. PhD thesis, PhD thesis, Karlsruhe University, 2000.
- [29] J. Sauer and G.H. Schnerr. Unsteady cavitating flow - a new cavitation model based on a modified front capturing method and bubble dynamics. In *In Fluids Engineering Summer Conference, Proceedings of FEDSM*, 2000.
- [30] H. Li A.K. Singhal, M.M. Athavale and Y. Jiang. Mathematical basis and validation of the full cavitation model. *Journal of Fluids Engineering*, 124(3):617–624, 2002.
- [31] A.G. Gerber P.J. Zwart and T. Belamri. A two-phase model for predicting cavitation dynamics. In *ICMF 2004 International Conference on Multiphase Flow, Yokohama, Japan*, 2004.
- [32] Robert F Kunz, David A Boger, David R Stinebring, Thomas S Chyczewski, Jules W Lindau, Howard J Gibeling, Sankaran Venkateswaran, and TR Govindan. A preconditioned navier–stokes method for two-phase flows with application to cavitation prediction. *Computers & Fluids*, 29(8):849–875, 2000.
- [33] J. C.L. Merkle, Z. Feng and P.E.O. Buelow. Computational modeling of the dynamics of sheet cavitation. In *3rd International Symposium on Cavitation, Grenoble, France*, 1998.
- [34] I. Senocak. *Computational Methodology for the Simulation of Turbulent Cavitating Flows*. PhD thesis, PhD thesis, University of Florida, Florida, 2002.
- [35] I. Senocak and W. Shyy. Interfacial dynamics-based modelling of turbulent cavitating flows, part-1: Model development and steady-state computations. *International Journal for Numerical Methods in Fluids*, 44:975–995, 2004.
- [36] I. Senocak and W. Shyy. Interfacial dynamics-based modelling of turbulent cavitating flows, part-1: Time-dependent computations. *International Journal for Numerical Methods in Fluids*, 44:997–1016, 2004.
- [37] Tobias Huuva. *Large eddy simulation of cavitating and non-cavitating flow*. Chalmers University of Technology, 2008.
- [38] Nai Xian Lu. *Modeling cavitation mechanisms using large eddy simulation*. Chalmers University of Technology, 2013.
- [39] Nai-xian Lu, Rickard E. Bensow, and Göran Bark. LES of unsteady cavitation on the delft twisted foil. *Journal of Hydrodynamics, Ser. B*, 22(5):784–791, 2010.
-

- [40] Rickard E. Bensow and Göran Bark. Implicit LES predictions of the cavitating flow on a propeller. *Journal of Fluids Engineering*, 132(4):041302, 2010.
- [41] Rickard E. Bensow. Capturing secondary cavitation—a step towards numerical assessment of cavitation nuisance. *Ship Technology Research*, 2011.
- [42] Rickard E. Bensow and Christer Fureby. On the justification and extension of mixed models in LES. *Journal of Turbulence*, (8), 2007.
- [43] H. Jasak H.G. Weller, G. Tabor and C. Fureby. A tensorial approach to CFD using object oriented techniques. *Computational physics*, 12, 1997.
- [44] Hrvoje Jasak. *Error Analysis and Estimation for the Finite Volume Method with Applications to Fluid Flows*. PhD thesis, Department of Mechanical Engineering, Imperial College of Science, Technology and Medicine, 1996.
- [45] Rusche Henrik. *Computational Fluid Dynamics of Dispersed Two-Phase Flows at High Phase Fractions*. PhD thesis, Department of Mechanical Engineering, University of London, Technology and Medicine, 2002.
- [46] Abolfazl Asnaghi. *InterPhasChangeFoam Tutorial [Online]*. Chalmers University of Technology, 2013. Available http://www.tfd.chalmers.se/hani/kurs-er/OS_CFD_2013/AbolfazlAsnagi/interPhasChangeFoam_and.PANSTurbulenceModel.pdf.
- [47] F. Darwish and M. Moukalled. A unified formulation of the segregated class of algorithms for fluid flow at all speeds. *Numerical Heat Transfer, Part B: Fundamentals*, 37(1):103–139, 2000.
- [48] JP Franc and JM Michel. Attached cavitation and the boundary layer: experimental investigation and numerical treatment. *Journal of Fluid Mechanics*, 154:63–90, 1985.
- [49] Mohamed Farhat and Francois Avellan. On the detachment of a leading edge cavitation. In *4th International Symposium on Cavitation, CAV2001, California Institute of Technology, Pasadena, CA, USA*, 2001.
- [50] A Tassin Leger and SL Ceccio. Examination of the flow near the leading edge of attached cavitation. part 1. detachment of two-dimensional and axisymmetric cavities. *Journal of Fluid Mechanics*, 376:61–90, 1998.
- [51] Stephen B Pope. *Turbulent flows*. Cambridge university press, 2000.
- [52] N Wikstrom, G Bark, and C Fureby. Large eddy simulation of cavitation submerged objects. In *Eighth international conference on numerical ship hydrodynamics, Busan, Korea*, 2003.
- [53] Daniel D Joseph. Cavitation and the state of stress in a flowing liquid. *Journal of Fluid Mechanics*, 366:367–378, 1998.
- [54] Daniel D Joseph. Cavitation in a flowing liquid. *Physical Review E*, 51(3):R1649, 1995.

-
- [55] Sergey Martynov. *Numerical simulation of the cavitation process in diesel fuel injectors*. PhD thesis, The University of Brighton, 2005.
- [56] S Som, SK Aggarwal, EM El-Hannouny, and DE Longman. Investigation of nozzle flow and cavitation characteristics in a diesel injector. *Journal of Engineering for Gas Turbines and Power*, 132(4):042802, 2010.
- [57] Sung-Eun Kim and Susan Brewton. A multiphase approach to turbulent cavitating flows. In *27th Symposium on Naval Hydrodynamics, Seoul, Korea, 5-10 October 2008*.
- [58] P. Etude Dupont. *Etude de la Dynamique d'une Poche de Cavitation Partielle en Vue de la Prediction de l'Erosion dans LES Turbomachines Hydrauliques*. Ecole Polytechnique Federale de Lausanne, 1991.
- [59] Shin Hyung Rhee, Takafumi Kawamura, and Huiying Li. Propeller cavitation study using an unstructured grid based navier-stokes solver. *Transactions of the ASME*, 127, 2005.
- [60] Y. T. Shen and P. Dimotakis. The influence of surface cavitation on hydrodynamic forces. In *22nd American Towing Tank Conference, St. John's, Newfoundland, Canada, 1989*.
- [61] Evert-Jan Foeth. *The structure of three-dimensional sheet cavitation*. PhD thesis, Delft University of Technology, 2008.
- [62] EJ Foeth and T Terwisga. The structure of unsteady cavitation, part i: Observation of an attached cavity on a three-dimensional hydrofoil. In *Proceedings of 6th International Symposium on Cavitation, Wageningen, The Netherlands, 2006*.
- [63] Nai-Xian Lu, Rickard E. Bensow, and Goran Bark. Large eddy simulation of cavitation development on highly skewed propellers. *Journal of Marine Science and Technology*, 19, 2013.
- [64] Streckwall and Salvatore F. Results of the wageningen 2007 workshop on propeller open water calculations including cavitation. In *RINA Marine CFD, Southampton, England, 2008*.
- [65] Roberto Muscari Giulio Dubbioso and Andrea Di Mascio. CFD analysis of propeller performance in oblique flow. In *Third International Symposium on Marine Propulsors, smp13, Launceston, Tasmania, Australia, 2013*.
- [66] Rickard E. Bensow and Gran Bark. Implicit LES predictions of the cavitating flow on a propeller. *Journal of Fluids Engineering-Transactions of the Asme*, 132, 2010.
- [67] A. Stella, G. Guj, and Di Felice F. Implicit LES predictions of the cavitating flow on a propeller. *Experiments in Fluids*, 28, 2000.
- [68] D. Di Florio, F. Di Felice, G. P. Romano, and M. Elefante. Propeller wake structure at different advance coefficients by means of piv. In *Proceedings of PSFVIP-3, Maui, HI, 2001*.
-

REFERENCES

- [69] F. Di Felice, M. Felli, G. Giordano, and M. Soave. Pressure and velocity correlation in the wake of a propeller. In *Proceedings of Propeller Shafting, Virginia Beach, Norfolk, VA*, 2001.
- [70] F. Pereira, F. Salvatore, and F. Di Felice. Measurement and modeling of propeller cavitation in uniform inflow. *Journal of Fluids Engineering*, 126, 2004.
- [71] F. Salvatore, H. Streckwall, and T. van Terwisga. Propeller cavitation modelling by CFD-results from the virtue 2008 rome workshop. In *In The First International Symposium on Cavitation, smp09, Trondheim, Norway*, 2009.
- [72] 2nd international workshop on cavitating propeller performance. http://www.cae.utexas.edu/smp15/smp_workshop_2015.html. Accessed: 2015-04-11.
- [73] Potsdam Propeller Test Case svatech gmbh potsdam. http://www.sva-potsdam.de/pptc_data.html. Accessed: 2015-4-14.
- [74] Rickard E. Bensow, Gran Bark, Nai Xian Lu, Claes Eskilsson, and Florian Vesting. Computational tools for propeller cavitation analysis. In *15th Numerical Towing Tank Symposium, Cortona, Italy, October*, 2012.
- [75] Bark G and Bensow Rickard E. Hydrodynamic mechanisms controlling cavitation erosion. In *29th symposium on naval hydrodynamics, Gothenburg, Sweden*, 2012.